Long Term Behaviour of UHPC Shear Key Connections in Adjacent Box Girder Bridges Under Thermal Loading

By

Timothy Neirinck

A Thesis Submitted to the Faculty of Graduate Studies of

The University of Manitoba

In partial fulfillment of the requirements of the degree of

MASTER OF SCIENCE

Department of Civil Engineering

University of Manitoba

Winnipeg, Manitoba

Abstract

This thesis studies the cold weather performance of Ultra High-Performance Concrete (UHPC) shear keys within an adjacent prestressed concrete box girder bridge reinforced with steel dowels across the interface. Field data from the Little Morris River Bridge is reviewed to establish general trends in structure behaviour and a finite element model is created in Abaqus CAE to examine the cold weather behaviour of the shear key and bridge girders.

The finite element model included a developed traction separation model to represent the UHPC to girder concrete bond behaviour. The bond behaviour is established using the results of direct tension test in accordance with ASTM C1404/C1404M-98, slant shear test in accordance with ASTM C882, and Bi-shear test results to represent the response to different modes of loading across the shear key to girder bond. From these tests appropriate values for damage initiation and evolution were defined.

Finite element modelling revealed that damage and subsequent debonding initiates at the top of the shear key and progressively de-bonds further down the shear key under colder increments of temperature. It demonstrated that the primary mechanism of shear key damage is debonding in direct tension under increased increments of cold weather.

From parametric testing, decreasing the coldest on record temperature profile by a progressive 5 ^{o}C, it was found that debonding initiated at the top of the shear key by -37^{o}C and reached the level of dowels by -42 ^{o}C. Further, it was found that the evolution of shear key damage initiation and ultimate debonding is more pronounced at mid span

compared to at the support. As the damage to the shear key to beam bond progresses it is demonstrated by the finite element model that the dowels begin to transfer increasing tensile strain and resultant stress within the connection between the girders.

Acknowledgments

I would like to express my gratitude to my adviser, Dr. Dagmar Svecova for constant guidance over the many years it has taken to complete this project. This project would not have been possible without her constant support and patience. I would also like to thank Dr. Ali Semendary for valuable discussion, review of many finite element models, and wealth of knowledge he provided in completing this research program. I would also like to acknowledge Dr Emile Shehata and Dr Amir Gatefar for being in the advisory committee for this work. Finally, thank you to the many people in my life that have supported me over the many years it has taken to complete this work, it's been quite a journey.

Table of Contents

List of Figures

List of Tables

1.0 Introduction

1.1 Overview

Modern structural design seamlessly molds traditional and innovative materials to produce structures of unique form and function. One of the major tools available to structural engineers in the design of highway bridge structures is the use of adjacent concrete girders. Adjacent concrete girders, typically prestressed, may depend on a combination of a shear key and lateral post tensioning to ensure long term monolithic behavior between the girder units (CSA 2019). This behavior allows for effective load sharing between the adjacent units.

1.2 Adjacent Girder Bridges

Adjacent girder bridges may take many forms, however, in Manitoba the two most common girder types are precast prestressed concrete channel (PPCC) girders or precast prestressed concrete box (PPCB) girders without a cast in place deck. In both cases, a shear key and lateral post tensioning is utilized to modify the behavior of the girders to act monolithically, distributing load between each of the girder units.

Prestressed concrete, and by extension post tensioned concrete, was introduced in North America in the 1950's as an innovative approach to reinforced concrete construction (CPCI 2017). In its simplest form, prestressed concrete is a type of reinforced concrete in which internal reinforcement has been tensioned against the concrete. This tensioning results in a sustained pre-compression force being introduced into the concrete. Since concrete is strong in compression, but weak in tension, the pre-

compression force allows for improved response to externally applied loading. Pre-compression of the concrete allows the girder to remain in an un-cracked condition which promotes significant serviceability and durability benefits (Collins and Mitchell 1997).

The future durability and in-service performance of the shear key is a major consideration in the design of these structures. Premature degradation of the shear key or the lateral post tensioning can severely limit the structure's ability to support design loads through elimination of effective load transfer through monolithic behavior. It has been reported that distress in adjacent girder bridges is primarily due to cracking along shear keys and de-bonding of the interface between the shear key and girder (Newtson, et al. 2019). This cracking and debonding can lead to reflective cracking in the wearing surface and provide pathways for deleterious substances to ingress into the shear key, accelerating damage.

1.3 Current Practice in Shear key Implementation in Adjacent Girder Bridges

Historically the design of adjacent girder bridges has considered prestressing laterally across girder units, introducing precompression to the units as the primary method of reducing cracking at the shear key to girder interface to reduce instances of distress in the shear key connection (Lopez de Murphy, et al. 2010). The aim of the lateral post tensioning is to introduce enough precompression into the adjacent girders to limit the differential deflection of adjacent girder units under applied load. Figure *1* demonstrates deterioration of a laterally prestressed shear key.

Lateral post tensioning in bridges, especially those over waterbodies prone to flooding, are at risk of deterioration. Even in prestressed concrete structures, the conditions will be present at some point for the concrete to crack. Cracking to girders and shear keys can occur due to many factors which might include shrinkage of the concrete, unintended restraint, water seepage into concrete and expansion upon freezing, and overloads of the structure.

Figure 1: Corroded and Deteriorated Prestressing Strands Adjacent to Grouted Keyway *(Gulyas 1995)*

Once a crack does form, water can seep in, and upon freezing, cause expansion and further opening of the crack. This is further complicated depending on environmental exposure conditions. In harsh environments, such as the conditions experienced in northern climates, steel reinforced concrete is especially prone to deterioration. One of the major contributors to the deterioration is moisture ingress into concrete and the subsequent initiation of electrochemical corrosion of reinforcing steel (ACI Committee 201 2016). Corrosion of reinforcing steel within concrete is a complex process that is difficult to arrest once initiated. Significant attention is paid to design that attempts to

prevent corrosion of reinforcing steel within concrete. Design codes such as the Canadian Highway Bridge Design Code S6 (CSA 2019) places strict crack limits on concrete elements to promote long term durability and minimize the risk of corrosion. Corrosion results in significant expenditure each year to maintain and rehabilitate structures of all types.

Deterioration of the lateral post tensioning can subsequently lead to a loss of prestressing, in turn leading to reduced precompression on the shear key, and corresponding premature cracking and failure of the joint. Degradation of the lateral post tensioning and longitudinal prestressing can be seen in Figure 2. This picture depicts deterioration of the adjacent channel girder diaphragms at lateral post tensioning duct locations on a highway bridge just outside of Melita Manitoba, on PTH 3.

Figure 2: Wide Cracking at Post Tension Ducts in PPCC Bridge (Author's Photo, Melita Manitoba)

1.4 Project Background

Recently, Manitoba Transportation and Infrastructure (MTI), the transportation agency in Manitoba, has begun investigating alternatives to lateral post tensioning in adjacent girder bridges. Namely the use of Ultra High Performance Concrete (UHPC) shear keys reinforced with steel dowels as a viable alternative.

The consulting firm WSP Canada Limited was awarded the design of an adjacent girder bridge over the Little Morris River in the R.M of Morris, Manitoba. The shear key between the adjacent box girders were designed to have UHPC as the shear key material reinforced with dowels between the box girder and shear key. The structure is simply supported with joints over each pier unit and does not have a structural bridge deck over the adjacent girder units. The structure was tendered for construction in December of 2018 with construction completed in 2019. MTI has requested University of Manitoba to conduct comprehensive material testing on the joint and a monitoring program of joint performance through instrumentation of the bridge. The work presented in this thesis is part of the outcomes of the project.

1.5 Research Objectives and Scope

This research program is undertaken to analyze the in-situ performance of UHPC shear keys reinforced with dowels between adjacent girders with no lateral prestressing on a simply supported bridge span. The bridge over the Little Morris River has been instrumented to receive real-time data from the structure for a two year period. These sensors were placed to measure temperature gradient over the depth of the adjacent

box girders and to measure the corresponding strains within the shear key, girder, and dowels. This research project has three primary objectives:

- The first objective of this research is to conduct a literature review to develop a comprehensive understanding of past applications of UHPC as a shear key joint material in adjacent prestress concrete box girder bridges.
- The second objective is to utilize the instrumentation data from the Little Morris River bridge, combined with the results of the comprehensive material testing program, to create and calibrate a finite element model in Abaqus CAE software of adjacent box girders capable of replicating the measured response to temperature variation in the field across the shear key connection.
- The third and final objective is to provide an indication of the performance of the shear key in extreme cold weather.

1.6 Thesis Organization

This thesis is organized into five chapters as follows:

- Chapter 1: Introduces the research project, project background, and the research scope and objectives;
- Chapter 2: Details a literature review of key aspects related to the research program providing key findings and analysis results from related studies;
- Chapter 3: Provides an overview of the research program, research project background information, the developed material interaction model, and finite element model creation;

- Chapter 4: Provides the results of finite element model calibration and results of the parametric study under increasing increments of cold weather; and
- Chapter 5: Summarizes the conclusions of this research program and recommends areas of future work.

2.0 Literature Review

2.1 Introduction

The following chapter provides a summary literature review of Ultra High-Performance Concrete (UHPC) connections in adjacent girder bridges and past efforts to model their behaviour. This literature review covers the following topics:

- An overview of shear key connection design provisions in Canadian and American design codes in adjacent girder bridges;
- UHPC material interaction modeling;
- UHPC shear key studies under loading;
- Finite element modeling efforts related to the use of UHPC shear keys in bridges.

It is useful to reiterate that UHPC is a composite cementitious material with compressive strength ranging between 120 – 200MPa and tensile strength of up to 15MPa (CPCI 2017). The high compressive and tensile strengths are achieved through the addition of high quantity of steel fibres to the mix and use of supplementary cementitious materials (SCM). UHPC is characterized by a very low porosity and a discontinuous pore structure.

2.2 Shear Keys Connections in Adjacent Girder Bridges

Shear keys in adjacent girder bridges can come in multiple forms ranging from full depth joints to partial depth joints. The size and shape of the shear key design is dependent on the intended function, however, there is no standardized shear key shape within the major north American bridge design codes. In adjacent girder bridges shear keys are

typically designed to transfer moment and shear across the joint, however, there is scenarios where shear transfer only is desirable (CSA 2019).

The AASHTO LRFD design code 9th edition (AASHTO 2020) provides some general guidance on shear key proportioning and design. Clause 5.12.2.3.1 indicates that precast concrete units placed adjacent to each other in the longitudinal direction may be joined together transversely to form a deck system for both permanent and transient loadings. Clause 5.12.2.3.2, related to shear transfer across the joint, indicates that the shear key be not less than 7 in (177.8 mm) deep and the shear transfer at the joint can be modeled using a hinged connection between precast segments. Clause 5.12.2.3.3 covers the case where the joint is considered to provide full continuity between longitudinal beams forming monolithic behaviour. Under this provision the continuity can be achieved by any combination of transverse post tensioning, cast in place closure joints, or structural overlay.

CSA S6-19, The Canadian Bridge Design Code (CSA 2019), clause 8.21 indicates that multi beam decks consisting of prestressed units side by side shall have a means of transferring live load between the units. This can be achieved by any of the following methods:

- A 150 mm thick reinforced concrete structural slab;
- Grouted shear keys in combination with lateral post-tensioning providing a prestress of not less then 1.7 MPa, after all losses, over a compressed depth of joint not less than 175 mm; or

- An owner-approved means capable of live load shear transfer between the units.

From the review of bridge design codes it is clear that there is minimal information related to standardized shear key shape, design guidance, or methods other than structural overlay or lateral post tension to achieve monolithic behaviour. Overall the shear key must be designed to withstand three main typical mechanisms of failure which include shear failure occurring within the UHPC, compressive failure of the UHPC or substrate concrete and resultant slip, and bond failure. The following Figure *3* demonstrates the three main failure mechanisms.

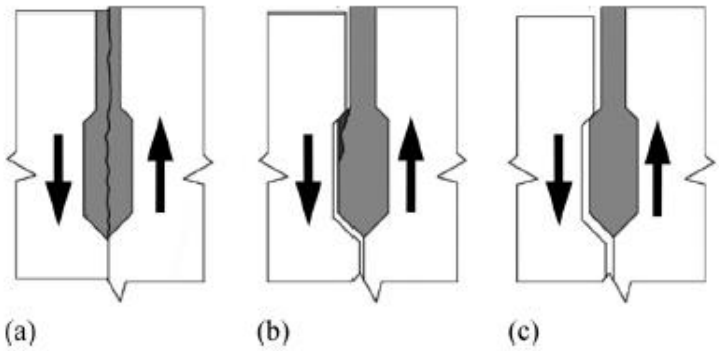

Figure 3: Typical Shear Key Failure mechanisms (a) Shear Failure; (b) Compressive Failure; (c) Bond Failure (From Sargand et al., 2017)

The exact provisions which are followed are dependent on the code being considered in the design of the shear key, however the shear resistance at the interface with the substrate concrete is designed to resist applied loading. Clause 5.7.4.3 of the AASHTO LRFD bridge design code covers the design of interface shear regions and covers three mechanisms which are considered to resist shearing force. These mechanisms include shear reinforcement, shear friction between concrete parts known as the clamping

force, and cohesion/adhesion between particles at the interface leading to shear resistance. The shear resistance is calculated using the following equations 1 through 4:

Equation 1: $$V_{ri} = \emptyset(cA_{cv} + \mu(A_{vf}f_y + p_c))$$

Equation 2: $$V_{ni} \leq K_1 f'_c A_{cv}$$

Equation 3: $$V_{ni} \leq K_2 A_{cv}$$

Equation 4: $$A_{cv} = b_{vi} L_{vi}$$

In these expressions $\emptyset$ is the limit state resistance factor, c is the cohesion factor dependent on the concrete application and surface roughness, A_{cv} is the interface shear area, μ is the friction factor also dependent on the surface condition of the interface, $A_{vf}$is the area of the interface shear reinforcement within the interface area, f_y is the yield strength of the interface steel, p_c is the permanent net compressive force normal to the shear plane which cannot be tensile, K_1 is the fraction of concrete strength available to resist interface shear, K_2 is a limiting interface shear resistance, b_{vi} is the interface width considered engaged in shear transfer, and finally L_{vi} is the interface length considered to be engaged in shear transfer.

The expression implemented within the AASHTO bridge code is designed to consider the contributions from cohesion and aggregate interlock in addition to the net normal clamping force through friction across the joint. The component cA_{cv} is meant to capture the effects of cohesion and aggregate interlock at the joint while the remaining component $\mu(A_{vf}f_y + p_c)$ captures the effect of shear reinforcement and net clamping

force resulting from compression across the joint. The limiting values of V_{ni} are introduced to prevent crushing and/or shearing of the aggregates along the joint shear plane bonded to the girders. Table 1 provides the interface parameters for various shear key concrete and surface roughness conditions in accordance with AASHTO LRFD clause 5.7.4.4.

Table 1: AASHTO LRFD 2019 Cohesion and Friction Factors for Interface Shear Transfer *(AASHTO 2020)*

Condition	Interface Parameter			
	Cohesion Factor, c (ksi)	Friction Factor, μ	K_1	K_2 (ksi)
Cast-in-place concrete slab on clean concrete girder surfaces, free of laitance with surface roughened to an amplitude of 0.25 in.	0.28	1.0	0.3	• 1.8 for normal density concrete • 1.3 for lightweight concrete
Normal weight concrete placed monolithically	0.4	1.4	0.25	1.5
Lightweight concrete placed monolithically, or placed against a clean concrete surface, free of laitance with surface intentionally roughened to an amplitude of 0.25 in.	0.24	1.0	0.25	1.0
Normal weight concrete placed against a clean concrete surface, free of laitance, with surface intentionally roughened to an amplitude of 0.25 in.	0.24	1.0	0.24	1.5
Concrete placed against a clean concrete surface, free of laitance, but not intentionally roughened	0.075	0.6	0.2	0.8
Concrete anchored to as-rolled structural steel by headed studs or by reinforcing bars where all steel in contact with concrete is clean and free of paint	0.025	0.7	0.2	0.8

CSA S6-19, The Canadian Bridge Design Code, clause 8.9.5 covers the design of interface shear transfer and is very similar to the provisions of AASHTO. The code

assumes that a crack forms along the shear plane, and the relative displacement is resisted by cohesion and friction maintained by the shear reinforcement crossing the crack. The code provides the following formulas shown in equation 5 to 8 to facilitate capacity calculations.

Equation 5: $$V_r = \lambda_1 \emptyset_C (C + \mu\sigma) + \emptyset_S p_V f_y cos\alpha_f$$

Equation 6: $$\lambda_1 \emptyset_C (C + \mu\sigma) \leq 0.25 \emptyset_C f'_c \text{ or } 6.5\,MPa$$

Equation 7: $$\sigma = p_V f_y sin\alpha_f + \frac{N}{A_{cv}}$$

Equation 8: $$p_V = \frac{A_{vf}}{A_{cv}}$$

Where λ_1 is a parameter dependent on the density of concrete, $\emptyset_C$ is the concrete material resistance factor, C is the cohesion value for interface shear transfer, μ is the friction coefficient, σ is the compressive stress across the shear-friction plane, $\emptyset_s$ is the resistance factor of the reinforcing bars across the shear plane, p_V is the ratio of vertical shear reinforcement to the gross concrete area of the horizontal section, f_y is the reinforcing steel yield strength, α_f is the angle between the shear reinforcement and the shear plane, N is the unfactored permanent load normal to the shear interface area, A_{cv} is the area of concrete resisting shear transfer, and A_{vf} is the area of shear friction reinforcement. Different values of C and μ are provided for different surface conditions ranging between a clean surface free of laitance, to a clean roughened surface free of laitance, to concrete placed monolithically.

Table *2* provides the interface parameters for various shear key concrete and surface roughness conditions in accordance with CSA S6-19 clause 8.9.5.2.

Table 2: CSA S6-19 Cohesion and Friction Factors for Interface Shear Transfer *(CSA 2019)*

Condition	Interface Parameter	
	Cohesion Factor, c (MPa)	Friction Factor, μ
Concrete placed against hardened concrete, with the surface clean and free of laitance but not intentionally roughened	0.25	0.6
Concrete placed against hardened concrete, with the surface clean and free of laitance and intentionally roughened to a full amplitude of about 5 mm and a spacing of about 15 mm	0.5	1
Concrete placed monolithically	1	1.4

Overall, the Canadian bridge code provisions are fundamentally similar to the AASHTO LRFD code provisions. Differing values of cohesion and friction are provided between the two codes as well as differing cutoff limits to account for the potential for the crushing of concrete and shearing of aggregates at the joint.

2.3 UHPC Material Interaction Model

When finite element modeling the UHPC to high strength concrete (HSC) interface a surface based cohesive model combined with compressive and friction behaviour is typically implemented (Semendary, Steinberg, et al. 2019). This model represents the interface as two types of behaviour. Surface based cohesion is represented by a traction separation model, which allows for the debonding failure mode to be represented within the finite element model. Buildup of strains and resultant stresses at the interface is represented by compressive and friction models.

The traction separation model is a methodology of modeling the interaction between two materials, in this case the UHPC and HSC materials under stress and allows for the representation of a debonding failure mode between two materials (Sudziak, Jackiewicz-Rek and Kozyra 2021). This model first considers the interaction between materials using linear elastic behaviour up to a point of damage initiation, typically defined as the quadratic interaction function Equation 10, which is then followed by the evolution of damage and corresponding change in behaviour at the interface. A schematic representation of the model can be seen in Figure *4*. Following the onset of damage initiation, denoted by the peak traction force, damage evolution is then considered by the model.

The model considers the initial normal (t_n^0) and shear stresses t_s^0 and t_t^0 in the two corresponding available directions of shear (vertical and longitudinal) shown in Figure *5*. The behaviour of the connection is assumed to occur in a linear elastic manner prior to the onset of damage initiation. Deformations in each direction of loading are calculated within the finite element model and then compared to the initial material thickness. This allows for directional strains (ε_n, ε_s, and ε_t) to be calculated which are then multiplied by the corresponding directional material stiffness response to calculate the stresses at the state of loading being considered.

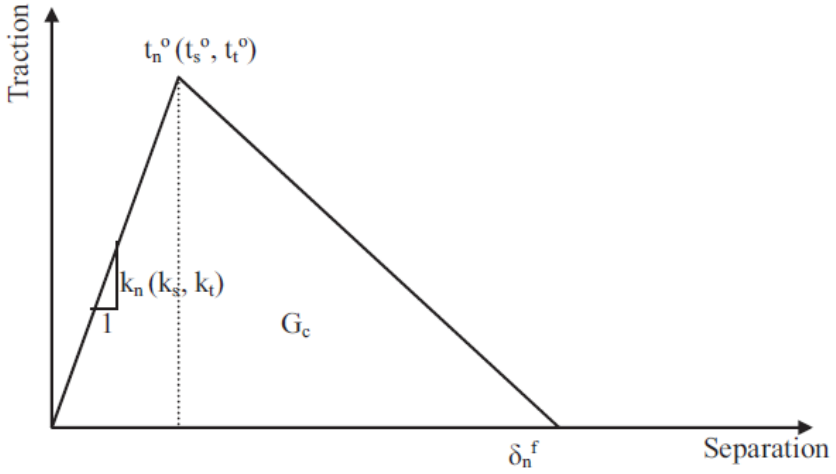

Figure 4: Traction Separation Model With Exponential Damage Evolution (From Hussein et al, 2017)

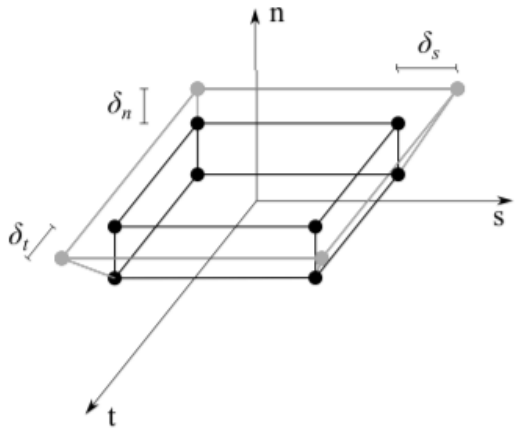

Figure 5: Local Element Directions of Contact Stresses and Deformations *(*Sudziak et al, 2021*)*

Material response stiffness values K_{nn}, K_{ss}, and K_{tt} for the normal and shear directions of deformation are defined within the model. In turn, contact stresses at time of loading are calculated utilizing the following relationship shown in Equation 9.

Equation 9:
$$T = \begin{bmatrix} t_n \\ t_s \\ t_t \end{bmatrix} = \begin{bmatrix} K_{nn} & 0 & 0 \\ 0 & K_{ss} & 0 \\ 0 & 0 & K_{tt} \end{bmatrix} \times \begin{bmatrix} \varepsilon_n \\ \varepsilon_s \\ \varepsilon_t \end{bmatrix} = K\varepsilon_n$$

The damage relationship of the cohesive connection begins when the damage initiation criterion is exceeded. One of the commonly implemented relationships for damage initiation in finite element modeling of the UHPC to HSC connection is the quadratic nominal stress model. When the sum of the squares of the contact stress at damage initiation for the considered loading mechanism divided by considered contact stresses meet a ratio of unity, debonding initiates. The following equation 10 shows the damage onset criteria.

Equation 10: $$\left(\frac{\langle t_n \rangle}{{t_n}^o}\right)^2 + \left(\frac{t_s}{{t_s}^o}\right)^2 + \left(\frac{t_t}{{t_t}^o}\right)^2 = 1$$

Within Equation 10 the parameters t_n, t_s, and t_t define the contact stresses within the normal and shear directions of loading across the bond. The parameters ${t_n}^o$, ${t_s}^o$, and ${t_t}^o$ all define the corresponding contact stress when damage starts to initiate within the UHPC to HSC bond, as shown in Figure *4*.

Multiple approximation models exist to define the descending branch of the traction separation model to consider the evolution of damage with increased loading and resulting bond slip relationship following the initiation of damage such as the traction separation law utilizing exponential damage evolution (Sudziak et al, 2021). These methods attempt to approximate the critical fracture energy up to failure, which is represented by G_c, the area under the curve of the traction separation model shown in Figure *4*. Laboratory testing can be completed to find the critical fracture energy of the connection instead of using an approximation model.

The critical fracture energy is different dependent on the direction of loading and resultant mechanism of bond failure. The critical fracture energy can be obtained from experimental results using bond specimens. For example, tensile bond testing will provide tensile capacity of the interface. Similarly, slant shear test on bond specimens will provide the combined response to compression and shear at the interface, while direct tension shear strength at the interface may be obtained from bi-shear test on bond specimens.

2.4 UHPC Shear Key Behaviour

Many researchers have investigated the use of UHPC shear keys in adjacent concrete girder bridges as well as other applications such as prestressed bridge deck slabs. The following experimental programs outline some key findings of shear key behaviour.

Ozyildrim and Moruza (Ozyildrim and Moruza 2016) performed a comparative evaluation of bridge structures containing three different shear key grouting materials in an adjacent box girder bridge. The materials utilized were a non-shrink grout with no fibres, an engineered cementitious composite (ECC) with polyvinyl alcohol fibres, and UHPC with steel fibres. The main objective of this comparative study was to find the grouting material with the highest potential to prevent cracking and leakage at the shear key. The researchers monitored the bridges for a 1-year period for crack formation and leakage at the joints between the adjacent girders (Ozyildrim and Moruza 2016).

It was ultimately found that the ECC grout performed the best exhibiting deflection hardening, a behavior of fibre reinforced composites whereby additional material

capacity is gained upon cracking, where fibres in the composite restrict cracks from widening. This behaviour is characterized by an increase in stress in the concrete with further deflections following first crack of the concrete. The UHPC material in this study did not exhibit similar deflection hardening material behaviour to the ECC grout and ultimately formed some cracks. This was attributed by the researchers to settlement of the steel fibres during placement of the UHPC. It was also found that the UHPC had a delayed setting time which made it difficult to prevent settlement of the steel fibres to the bottom of the shear key. The researchers ultimately concluded that ECC performed the best, preventing leakage at the joint. The superior performance of the ECC was attributed to both deflection hardening behaviour and a faster set time (Ozyildrim and Moruza 2016).

This study demonstrates certain limitations of UHPC that need to be overcome through proper detailing and placement procedure of the shear key. Missing from this study is information pertaining to the surface roughness of the substrate concrete at the shear key locations, a key consideration in bonding of the shear key, and ultimate potential for crack formation in the long term.

In a study examining full scale testing of shear key details for Precast Concrete Box girder bridges Yuan and Graybeal (Yuan and Graybeal 2016) examined connection details between adjacent girder bridges including current good practices in high strength non-shrink grout in combinations with transverse post-tensioning as well as connection details using ultra high performance concrete. Many factors which effect shear key

performance including traffic loading, thermal loads, level of transverse post tensioning, and different connection designs were examined as part of the study.

Of key interest was their examination of partial depth and full depth UHPC shear keys. The details of these shear keys can be schematically viewed below in Figure 6. The girders were subjected to both experimental thermal and structural loading cycles. Following loading no crack were observed in the connection. It was found that the UHPC connection performed very similar to an intact conventional grout connection in terms of moment distribution and differential deflection between girders. It was further found that the bonding properties between the girder and UHPC shear key was stronger than the underlying girder.

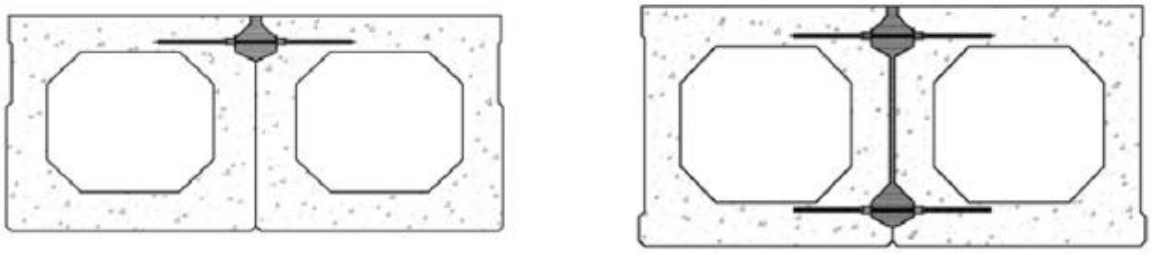

Figure 6: Investigated Partial and Full Depth Shear Key Orientations (Yuan and Graybeal, 2016)

The study concluded that the behaviour of the UHPC shear key can be expected to be comparable with well-constructed monolithic concrete decks. The researchers observed that the capacity of the UHPC connection enhanced the connection capacity beyond the tensile resistance of the precast box girders. They further concluded that transverse reinforcement within the connection act to enhance the local shear and tensile strengths directly resulting in reduced crack widths.

Halbe *et al.* (Halbe, et al. 2017) performed a research program with the aim of developing improved connection details for adjacent prestressed girder bridges. One main goal of this research program was to eliminate the need for lateral post tensioning across the shear keys. The study performed full scale testing on 6 box girder sub-assemblages, each with a different shear key connection detail. The tested connections consisted of assemblies with typical grout, grout reinforced with a kevlar strip over the joint, UHPC with lapped steel dowels with and without composite deck, and Very High-Performance Concrete (VHPC) with lapped steel dowels with and without composite deck. The aim of testing VHPC was to investigate a nonproprietary high-performance concrete behavior that attempted to behave in a similar manner to the proprietary UHPC material.

This study found that both the UHPC and VHPC performed well providing a high level of durability. Under cyclic testing, performed to represent repeated simulated loadings of the AASHTO design truck, both shear key materials lasted over 1 million cycles of loading without any full depth cracks developing. This is a benefit of the UHPC shear key, as water ingress is a key mechanism of deterioration within adjacent girder bridges.

Overall the UHPC and VHPC materials were considered better filler materials then typical grout by the researchers as they exhibit less shrinkage then typical joint grout. The research program further demonstrated that lapped splice bars within the shear key connection allow for abatement of cracking and successful shear and moment transfer across the joint.

In an examination of the early age behaviour of UHPC shear key in adjacent prestressed box girder bridges containing UHPC shear keys with transverse dowels Semendary et al. (Semendary, Walsh and Steinberg 2017) studied the early age strains in the UHPC shear key, girders, and transverse dowels at the joint. The study validated that the dowels play a role in carrying transverse stresses across the joint at the early age of the structure before the UHPC gains sufficient strength. The study found many key observations including:

- No cracking was visually observed in the shear key interface in its early age;
- The shear key responded to temperature gradients experienced by the beams. As the top of the beam experienced a temperature increase, compressive strains were generated. As the beam cooled the opposite occurred. The bottom of the beams experienced reduced influence to temperature;
- The same behaviour was experienced in the transverse and longitudinal directions, however, there was a delay between temperature peaks and strain peaks in the transverse direction; and
- The longitudinal and transverse strains within the shear key behave similar to that of the longitudinal strains within the girder, and further the strains within the dowel bars did respond to changing temperature, indicating load transfer.

Overall, this study of shear key performance reviewed the behaviour of the girders and shear key strains when subjected to thermal gradient loading. It demonstrates general expected behaviour of the shear key regarding tension and compression and further demonstrates that dowels are playing a role in behaviour.

2.5 Past Modeling Efforts of UHPC Shear Keys in Adjacent Girder Bridges

Many past finite element modeling efforts have been undertaken to model the behaviour of UHPC shear keys in adjacent girder bridges. These modeling efforts are typically undertaken in Abaqus CAE software and require a firm understanding of in-situ material properties, bridge behaviour, and interaction properties between the HSC and UHPC.

Steinberg *et al.* (Steinberg, et al. 2014) performed a parametric analysis of adjacent prestressed concrete box beams with UHPC dowel reinforced shear keys. This study investigated the effects of varying the transverse dowel spacing in full depth and partial depth shear keys. The goal of the research was to better understand the performance of longitudinal UHPC shear key and the capability of the dowel bars to transfer loading between adjacent girders. An examination on the effects of gradient temperature with depth from the girder top was performed in this study. The authors examined set beam geometry in the Abaqus CAE finite element software. The models were compared to testing being completed on similar girders for verification and calibration. The study found that principal tensile stresses within the shear key increased with positive temperature gradients. The principal tensile stresses also increased in both the shear key and shear key dowels with increased dowel spacing. The UHPC allowed for transfer of differential loading across the joint, with credit being attributed to the UHPC adhesive properties. The study ultimately recommended that a transverse dowel spacing of 12 inches (304.8 mm) was the most economical configuration, balancing both cost with both strength and serviceability requirements of the adjacent box beams.

In a follow up study Steinberg *et al.* (Steinberg, Semendary and Walsh 2016) examined the field performance of dowel reinforced UHPC shear key on a bridge in Fayette County Ohio, which the researchers stated was the first such application of a UHPC shear key in an adjacent box girder bridge. The field data was compared to the results of a three-dimensional finite element model in the Abaqus CAE software. Multiple load tests were performed on the structure for the purpose of data recording and calibration of the finite element model. These tested load configurations included:

- A single 56.1 kip (249.54 kN) truck load placed in the left lane;
- A single 53.4 kip (237.53 kN) truck load placed in the right lane;
- Two trucks placed side-by-side with a 109.6 kip (487.52 kN) total load; and
- Two trucks placed back to back in the left lane for a 109.6 kip (487.52 kN) total load.

Through this study and finite element modeling, the researchers were able to recreate comparable modeled transverse tensile strain within the shear key and longitudinal compressive strain for each of the tested load cases. The researchers were also able to model the tensile strain to a comparable magnitude to that recorded within the dowel bars. Through this modelling effort it was demonstrated that the UHPC shear key behaves in a predictable way, that can be recreated within a finite element model.

In part one of a two-part study *Hussein et al.* (Hussein, Walsh, et al. 2017) looked at the calibration and validation of a three-dimensional finite element model to examine UHPC shear key connection in adjacent box girder bridges. The objective of the study was to develop a model that could accurately represent the interaction between the UHPC joint

and the HSC substrate material. The authors modeled the UHPC to HSC joint using a traction-separation model with damage initiation criteria (DIC) and damage evolution being present in the behavioral modeling. The traction separation model considers an initial linear elastic behaviour at the interface which is then followed by the start and progression of damage.

The adhesive friction properties of the bond as well as the non-linear behaviour of the material and interface were considered. Through a lengthy calibration process the researchers were able to accurately model the shear key and interface behaviour between the UHPC and HSC substrate. It was concluded that accurately representing the friction and adhesion at this interface is of upmost importance when modeling the adjacent girder performance.

The calibration process examined multiple roughness and interface values, shown in Table *3* below through finite element modeling of slant shear tests and comparison to laboratory test results. The mechanical properties of the interface used in the finite element model produced results, presented in Table *4*, that correlated well with the laboratory test results. The researchers then utilized the interface model within the adjacent girder finite element model where they were able to achieve good agreement between the experimental and modeled results.

Table 3: UHPC to HSC interaction Traction Separation Model Parameters (Hussein et al, 2017)

Property	Smooth	Midrough	Rough
K_{nn} (N/mm^3)	1,358	1,358	1,358
K_{ss} and K_{tt} (N/mm^3)	20,358	20,358	20,358
t_n^o, t_s^o, and t_t^o (MPa)	3.02	5.01	5.63
Total/plastic displacement (mm)	0.018	0.117	0.241
Stabilization	0.001	0.001	0.001

Table 4: Comparison of Traction Separation Finite Element Model and Laboratory Testing Results (Hussein et al, 2017)

Roughness degree	Experimental average P (kN)	Failure experiment	FE model P (kN)
Smooth	75.86	Bond	75.713
Midrough	252.2	Bond	227.31
Rough	620.4	Concrete	602.75

In part two of the study Sargand *et al.* (Sargand, et al. 2017) examined the mechanism of load transfer between adjacent box girders with a UHPC shear key. The goal of the research was to perform a finite element analysis of two adjacent box-beams to investigate the load transfer mechanism and ultimate load capacity of the shear key design. The researchers examined the role of the UHPC material, transverse dowel reinforcement, and surface roughness at the UHPC to HSC interface within the load transfer across the shear key between adjacent box girders. The study of load transfer mechanism demonstrated the following summarized points:

- A shear key with a smooth roughness parameter and no transverse dowels into the key was capable of transferring load between the adjacent girders. This

finding would allow for specification of minimal shear reinforcement saving time and cost;

- The UHPC joint connection failed by crushing of the top surface of the HSC beam regardless of the surface roughness at the beam to shear key interface however differences were noted for smooth versus mid-rough and rough interfaces.
- When smooth surface roughness was modeled the shear key de-bonded to the depth of dowel reinforcement prior to failure. When mid-rough and rough bonding surface parameters were utilized, the bond remained intact up to failure load with no debonding being noted.

Key modeling outcomes demonstrated the benefit of the transverse dowel reinforcement and influence of surface roughness on shear key behaviour. The results of these two studies demonstrate the importance of the surface condition of the UHPC to HSC surface on finite element modeling and ultimate in-situ performance of the UHPC shear key.

Hussein *et al.* (Hussein, Sargand and Khoury 2019) studied the load transfer mechanism of the UHPC shear key under static truck load testing of a full scale bridge and used those results to develop and validate a traction separation interface model between the UHPC shear key and substrate concrete within a finite element model of the bridge superstructure. The researchers developed a finite element model in Abaqus CAE which included the shear key, girders, internal shear reinforcement, prestressing

strand bars within the girder, and bearing pads under the girder ends. A traction separation model was utilized at the UHPC to HSC shear key interface.

Modeling was conducted in three stages to represent the construction staging and its influence on the structure behaviour. First prestressing was applied to the girders, second the gravity loads and boundary conditions (bearings) were applied, and then finally the truck load was investigated. Calibration to field results was facilitated by fixing the bottom of the bearing pads and modifying the frictional contact value between the bearing and girder interface. The researchers note the method worked well, with good agreement being achieved between the measured and modeled results.

The study ultimately demonstrated that the high bond strength, friction, and shear key interlock between the girders provides a high degree of load transfer between girders with minimal differential deflection being noted between girders in the field and with the modeled results. The results further indicated that minimal steel dowels are required to achieve the desire load transfer between girder units. Ultimately, the finite element modeling conformed well to the measured strains at the interface when modeled using a traction separation model.

In another study Semendary *et al*. (Semendary, Steinberg, et al. 2019) investigated the effects of temperature distribution on thermally induced behaviour of the UHPC shear key connection in adjacent box girder bridges. This study sought to validate a finite element model of adjacent box girders against field data for thermally induced stresses within UHPC shear key connections.

The finite element model was created in Abaqus CAE and contained all girders and shear keys within the bridge superstructure including prestressing strands within the girders, longitudinal reinforcement, dowels into the shear keys, and diaphragms. The interface between the UHPC shear key and HSC was modeled using a traction separation model. The temperature measured from the in-situ thermocouples with depth from the top of the girders was mapped to the model. The temperature was mapped consistently across all bridge girders along the bridge's length and width.

The resulting model was able to capture the behaviour of the structure and compared well to the field data. A key property of the shear key examined by the researchers as part of the modeling effort was the damage index (DI) of the interface bond. This index is a measure of the degradation and eventual failure of the bond between the HSC and UHPC. More directly the damage index is the numerical result of the quadratic damage initiation function, Equation 10, where a value of unity indicates debonding of the shear key at a particular location. It was noted that as transverse strain increases so too does the interface DI. A key conclusion of this modeling program was that the maximum transverse tensile strain in the shear key, and resultant damage index, is when the top flange and web are negative and bottom flange is positive.

Overall, this study validated that the traction separation model of interface behaviour is appropriate to further model the effects of thermally induced loading on the shear key and also found that temperature gradient effects are a potential source of deterioration of the UHPC to high strength concrete connection.

3.0 Research Program

The research program is undertaken to analyze the in-situ performance of UHPC shear keys reinforced with dowels between adjacent girders without lateral prestressing on a simply supported bridge span. The bridge over the Little Morris River has been instrumented to receive strain and temperature data from the structure.

This thesis focuses on the creation of a finite element model within the software Abaqus CAE of adjacent girders to replicate the field measured data from the Little Morris River bridge and performs a parametric study on the extreme cold performance. Field data collection and processing as well as material testing data that informs this study is presented that was completed by other members of the research team Dr Ali Semendary and Li Xin Tan.

This chapter summarizes the conducted research program including:

- Overview of Little Morris River Bridge and data collection (completed by others);
- Summary of bridge thermal behaviour under cold and warm weather;
- Summary of material testing program and results (completed by others);
- Formulation of the traction separation model used to represent shear key behaviour within the finite element model; and
- Overview of the adjacent box girder finite element model;

3.1 Little Morris River Bridge

Constructed in the summer of 2019, the Little Morris River bridge is a five-span structure consisting of four spans of simply supported Precast Prestressed Concrete

Channel Girders (PPCCG) and one simply supported span of Precast Prestressed Concrete Box Girders (PPCBG) centred with the river. The investigated box girder span elevation and cross section, taken from the tender drawings, is shown in the following Figure 7 and Figure 8.

The bridge superstructure cross section features a clear roadway width of 9.6 m composed of two 3.7 m travel lanes and two 1.1 m shoulders. The superstructure is overlain by an asphalt overlay and hot poured rubberized asphalt waterproofing membrane complete with 6 mm protection board between the waterproofing and asphalt. The driving surface features a 2% cross fall off centreline, made up entirely by thickening and thinning the asphalt. The girders have exterior mounted Test Level 2 bridge rails.

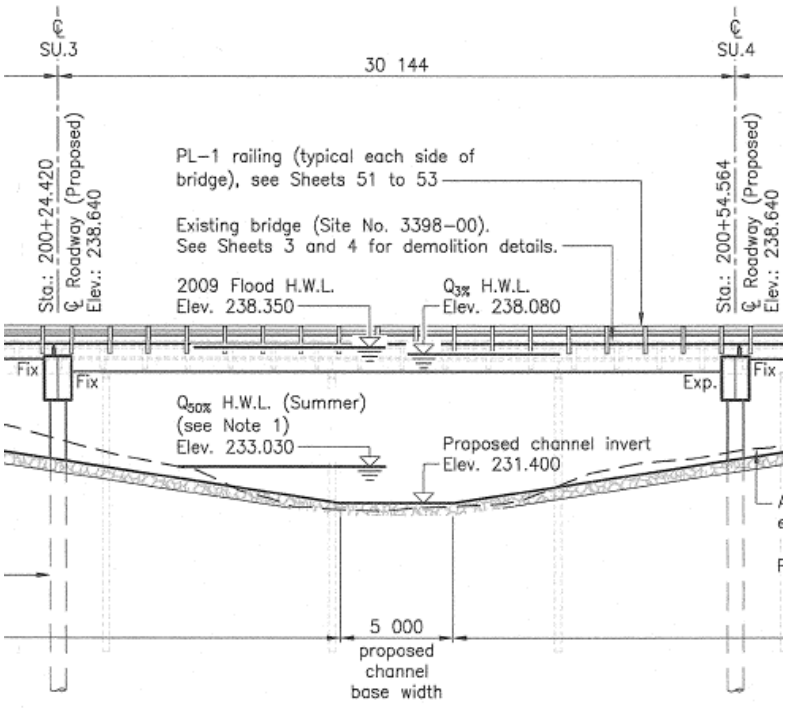

Figure 7: Little Morris River Bridge Centre Span General Elevation *(WSP 2018)*

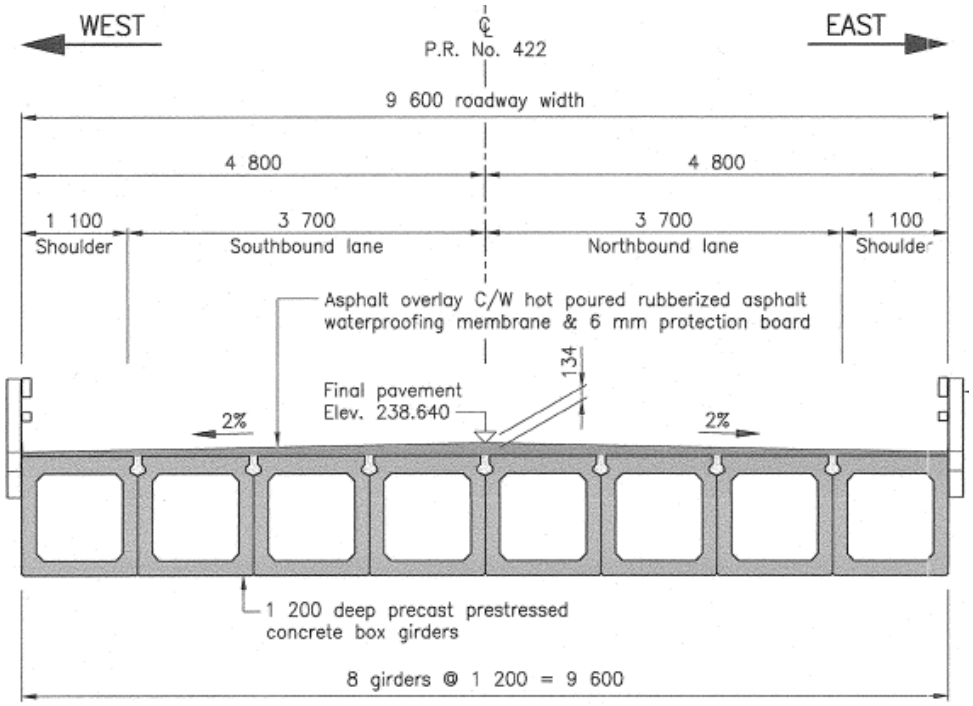

Figure 8: Cross Section of Prestressed Box Girder Span *(WSP 2018)*

The centre box girder span is 30.144 m from centre to centre of bearing with a girder out to out dimension of 30.4 m. The span is simply supported founded of steel reinforced elastomeric bearings with flexible expansion joint strip seals at either end of the span. Fixity of the girders at the fixed end of the span is supplied to select girders in the form of steel dowels grouted into girder ends and pier cap. From the west edge of the structure girder lines 2, 4, 5, and 7 have these fixity dowels installed on either side of the bearing pad. The fixity dowel detail can be seen below in Figure *9*

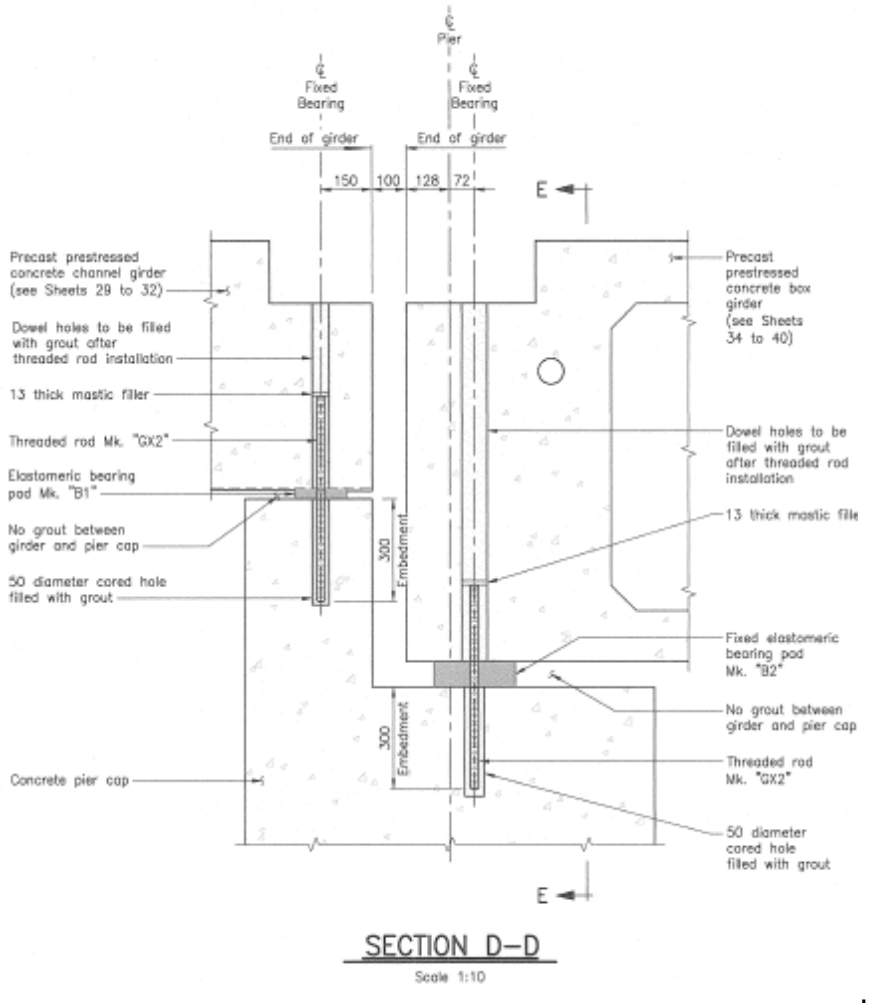

Figure 9: Fixed End of Girder Dowel Fixity Connection *(WSP 2018)*

On the expansion end of the girders, no longitudinal expansion fixity is provided, however, transverse movement is restrained by a transverse retaining angle. An elastomeric bearing bulk shear modulus G, of 1.1 MPa is listed on the drawings, and will provide some minor restraint to girder longitudinal movement.

The box girders are hollow and feature 150 mm thick concrete walls and floor. The roof of the box is minimum 150 thick (at centre of span) and maximum 174 mm (at end of span) thick due to reverse camber provided on the girder as it is prestressed, causing

the girder to deflect upward to the flat position because of the internal force couple induced from the prestressed tendons. The girders have internal diaphragms at a consistent 3.4 m spacing, each with lateral post tension ducts 0.7 m from the base of the girder. These ducts are present as a contingency plan to post tension girders laterally in the case the UHPC shear key were to not perform.

The girder prestressing features a two harp tendon profile with a total of 42 seven wire strands, 12 draped and 30 straight. Each seven wire strand is 12.7 mm diameter low relaxation uncoated steel strand. The design jacking force per strand P_j is 138 kN. The girders are reinforced with both longitudinal and transverse non prestressed steel reinforcement to provide crack control and shear reinforcement.

The center box girder superstructure segment is founded upon two reinforced concrete pier caps founded on steel pipe piles. These pier caps also have bearing keeper plates bolted to their surface to prevent the elastomeric bearings from moving forward off the pier cap. Overall the substructure does have some flexibility to it as a function of its design, however for this study the flexibility is considered negligible due to the nature of simple span, and presence of flexible bearings.

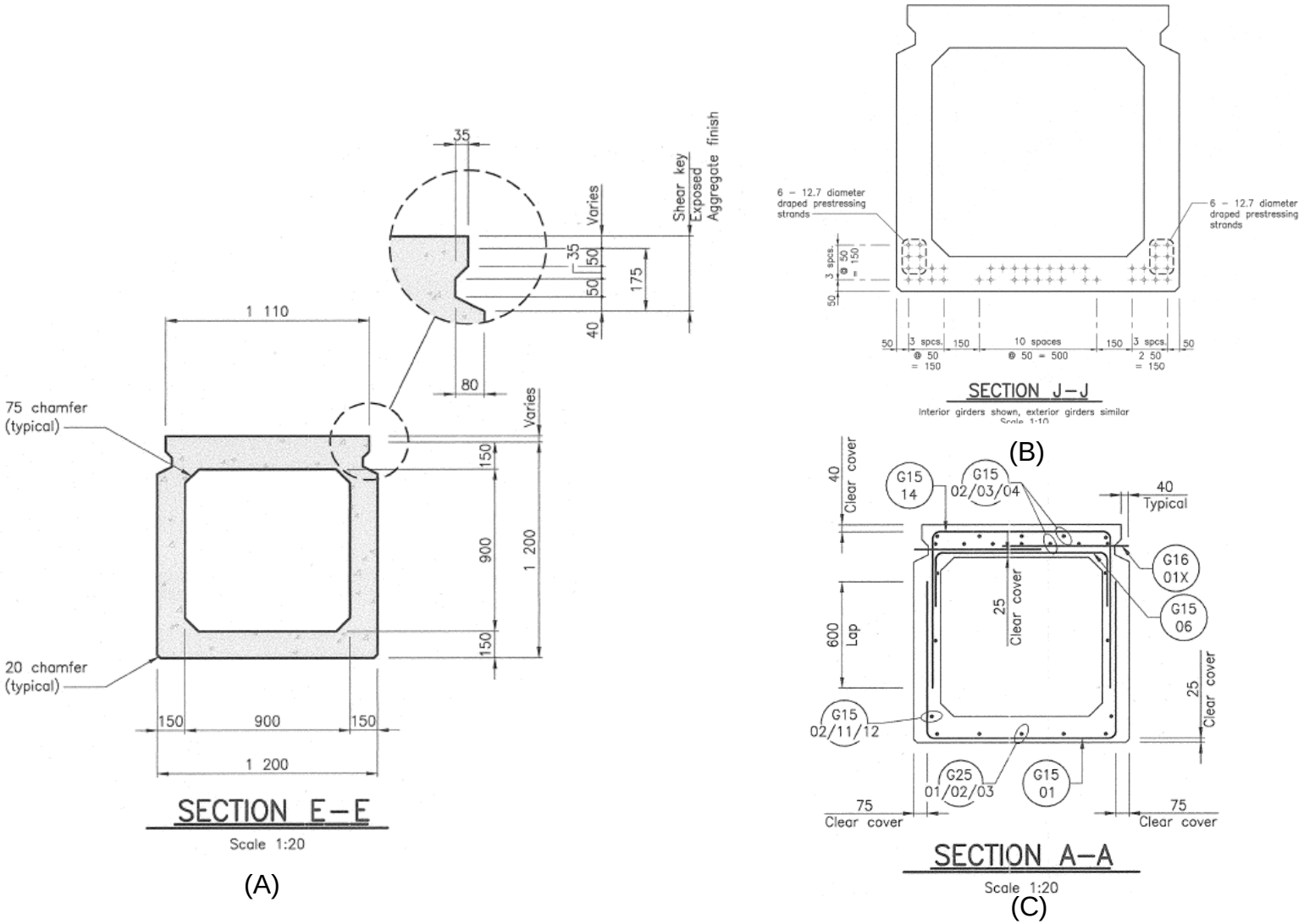

Figure 10: Girder Cross Section (a) Concrete Geometry; (b) Prestressing Steel; (c) Steel Reinforcing Bars *(WSP 2018)*

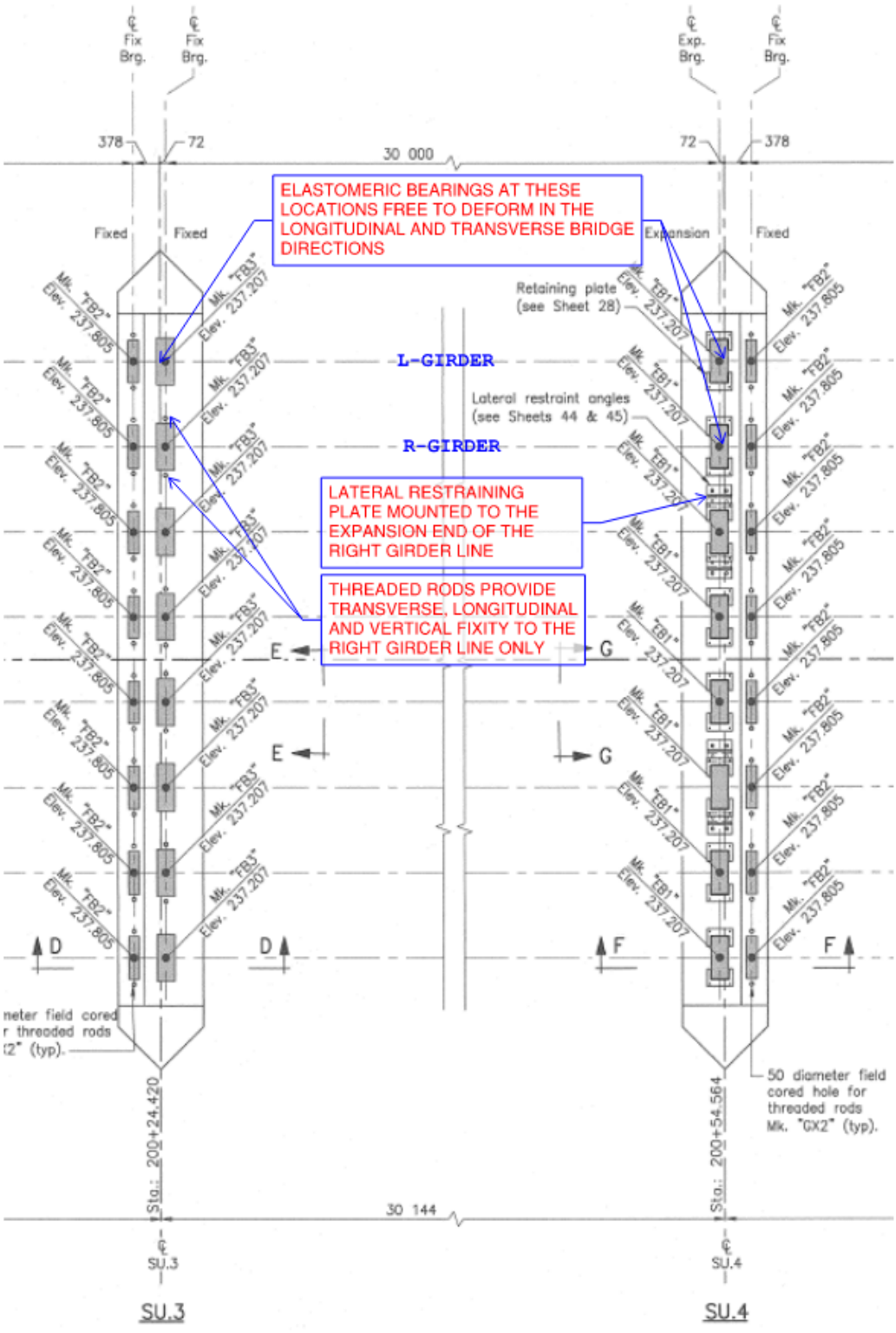

Figure 11: As-Constructed Girder Fixity Arrangement *(WSP 2018)*

3.2 UHPC Shear Key Geometry and Mix Properties

The dowel reinforced UHPC shear key is installed between adjacent box girder units. The shear key reinforcement dowels were designed to be placed along the longitudinal joint with 175 mm spacing and staggered at 87.5 mm spacing. The dowels had a design embedment of 80 mm into the shear key which was later extended to 125 mm during construction with a lapped bar. Figure 12 to Figure *14* contains the dowel layout, shear key geometry, and final dowel embedment modification.

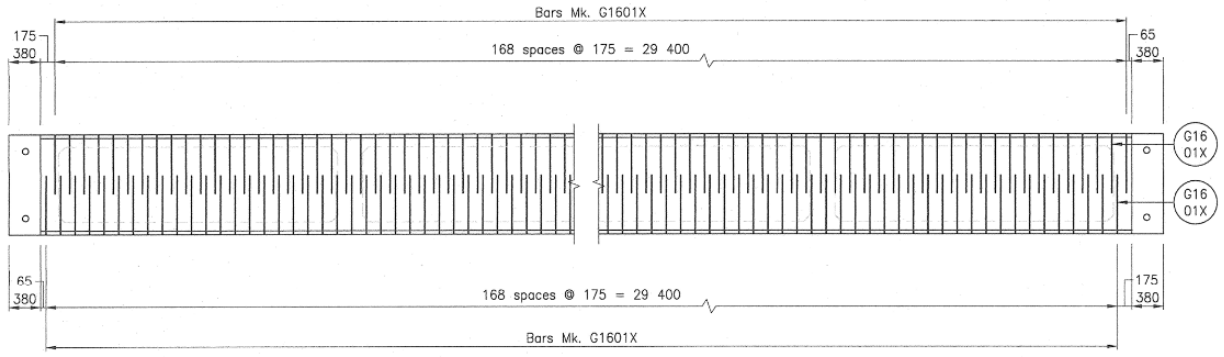

Figure 12: Bridge Design Drawings Dowel Layout Interior Prestressed Girder Plan View *(WSP 2018)*

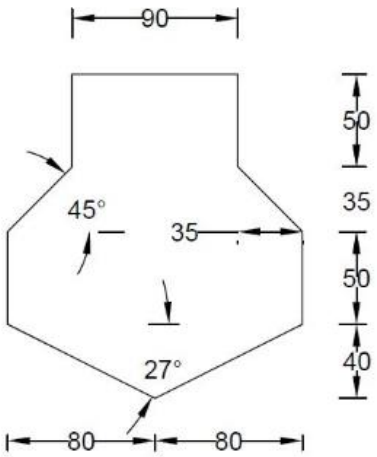

Figure 13: Shear Key Dimensions (From Tan, 2021)

Figure 14: Shear Key Rebar Modification to 125 mm Embedment (From Tan, 2021)

Shear key units were numbered from west to east, shown in Figure 15 with the west most shear key between beam 1 and 2 being shear key 1. The UHPC concrete was mixed by the Contractor onsite and contained the mix proportions shown in Table *5* below. Following mixing the UHPC was transported into place using wheelbarrows. The joints were placed on July 30, 2019 (Shear key 7) and on August 1, 2019 (Shear Keys 1-6).

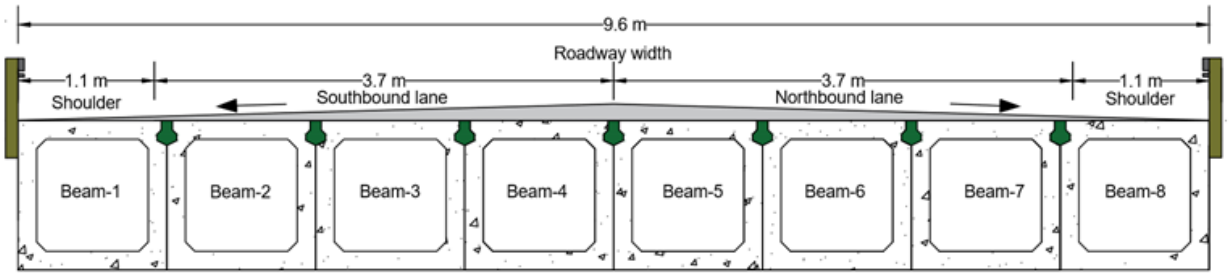

Figure 15: Shear Key Locations (green) and Beam Numbers (From Tan, 2021)

The shear key interface was pre wetted prior to joint placement. The mix temperature was between 26 and 36 ℃ while the ambient temperature was between 20 and 30 ℃ while the shear key was placed. During mixing and placement, static and dynamic flows of the UHPC were measured and found to be 215 mm and 225 mm respectively. Following casting the plywood was placed over the fresh UHPC concrete joint for 7 days.

Table 5: UHPC Mix Proportions

Material	Quantity (kg/m^3)
Premix	2195
Water	130
Premia 150	30
Steel Fibre (2%)	156

3.3 Field Data Collection

Strain and temperature data has been collected from instrumentation installed within selected girders within the Little Morris River Bridge. Sensors were originally installed within the bridge by others as part of the overall research project. The following is a summary of the sensor placement completed during bridge construction (Semendary, Tan and Svecova 2019)

The field data has been collected from the following instrumentation:

- Vibrating wire strain gauges installed within all eight of the adjacent box girders:
    - Gauges include transverse and longitudinal strain gauge installed in all top flanges at a depth of approximately 75 mm and one transverse strain gauge placed in the bottom flange of all girders;

  - One longitudinal strain gauge was placed in the bottom of beams 1 to 4 (beam 1 being the west most girder);
- Beams 1, 4, and 8 were instrumented with thermocouples distributed over the height of the beam at depths of 0 mm, 200 mm, 498 mm, 796 mm, 1100 mm, and 1200 mm measured from the bottom of the girder.
- A total of 28 shear key dowels (14 at mid span and 14 at the support) were instrumented, each with one strain gauge.

The layout of instrumentation within the bridge can be seen below in Figure 16 which is taken from the interim project report and shows the location of all sensors within the structure. Referencing the sensor layout, “G” prior to the gauge number denotes girder gauge, “K” denotes shear key gauge, “D” denotes a dowel gauge. In addition Figure *17* shows the sensor placement within the shear keys.

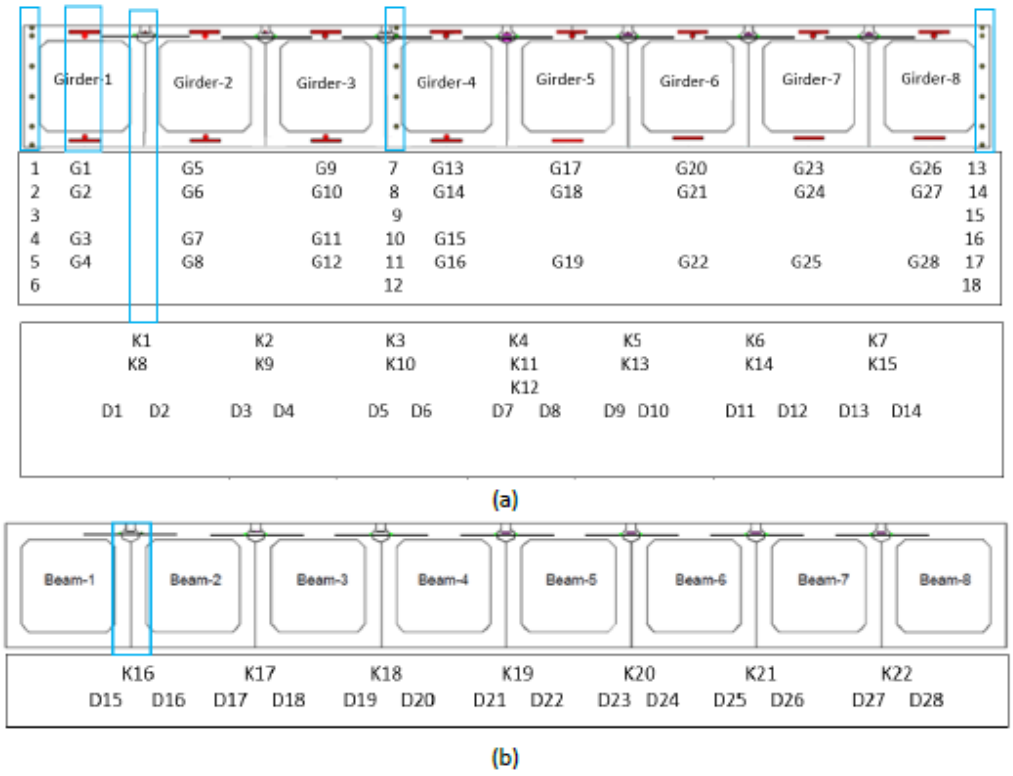

Figure 16: Location of Instrumentation (a) midspan; (b) At Support *(Semendary et.al. 2019)*

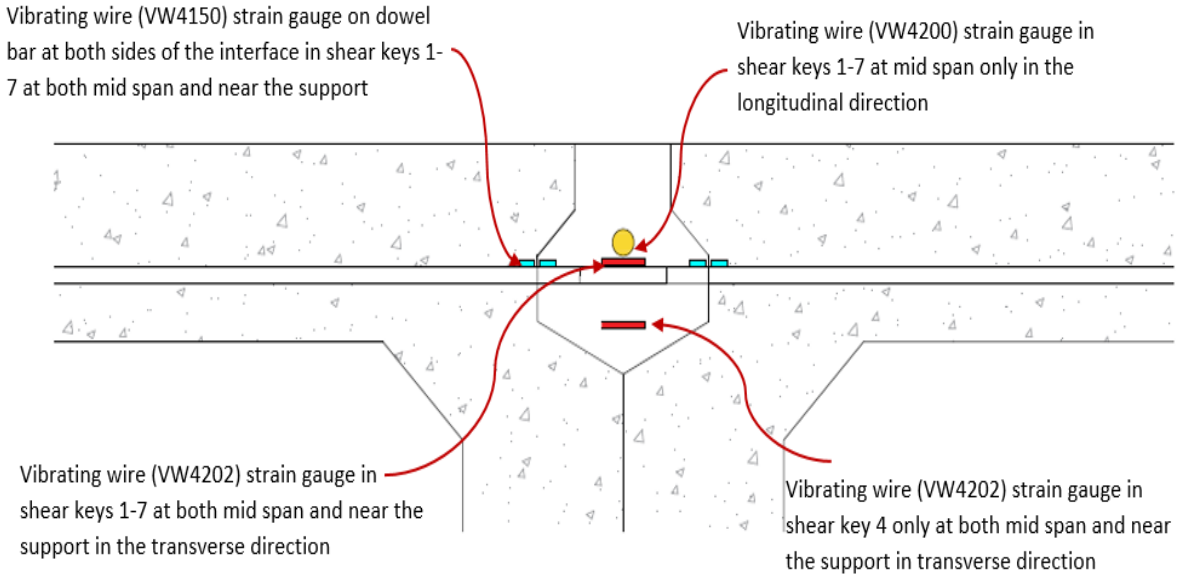

Figure 17: Strain Gauge Placement at Shear Keys *(Semendary et al. 2021)*

3.4 Strain and Temperature Readings

3.4.1 Structure Strain Response to Thermal Loading

The strain gauges and thermocouples recorded continuous temperature and strain data throughout the study period. In addition, temperature over the girder depth was also measured at mid span of the bridge on both exterior beams and between beam 3 and 4 as outlined in Section 3.3. The following Figure *18* through Figure *24* provide a snapshot of the strain and ambient temperature data, showing some general trends of behaviour within the girders and shear keys in cold and warm weather conditions between November 26th, 2019 and February 26, 2021. All strain graphs are processed by Dr. Ali Semendary as part of the research team work on the long-term strain behaviour of the structure (Semendary et al. 2021).

These strains have been offset to a baseline strain of 0με at 0℃ to demonstrate the total thermal effect with temperature fluctuation on structure strain. From the dataset the temperature profiles can be identified which represent the peak tensile and compressive strains within the transverse and longitudinal directions of both the shear keys and the girders induced by thermal loading.

First, examining Figure *18* and Figure *19* reveals some general trends as they relate to the longitudinal strain behaviour of the shear key under cold weather conditions. As the temperature transitions to below zero degrees Celsius longitudinal tension strain forms in the shear key. The strain and temperature readings are a consistent mirror image of each other. As the ambient temperature heats up, compression begins to form in the shear key. The strains experienced by each of the shear keys across the width of the

bridge, where measurements are taken, are stable as well, featuring similar magnitude of compression strain.

The peak tensile strain in the shear key longitudinal direction experienced by the structure was 103 με on February 14th, 2021. The peak longitudinal compressive strain of -132 με occurred in the girder top span on July 3rd, 2020.

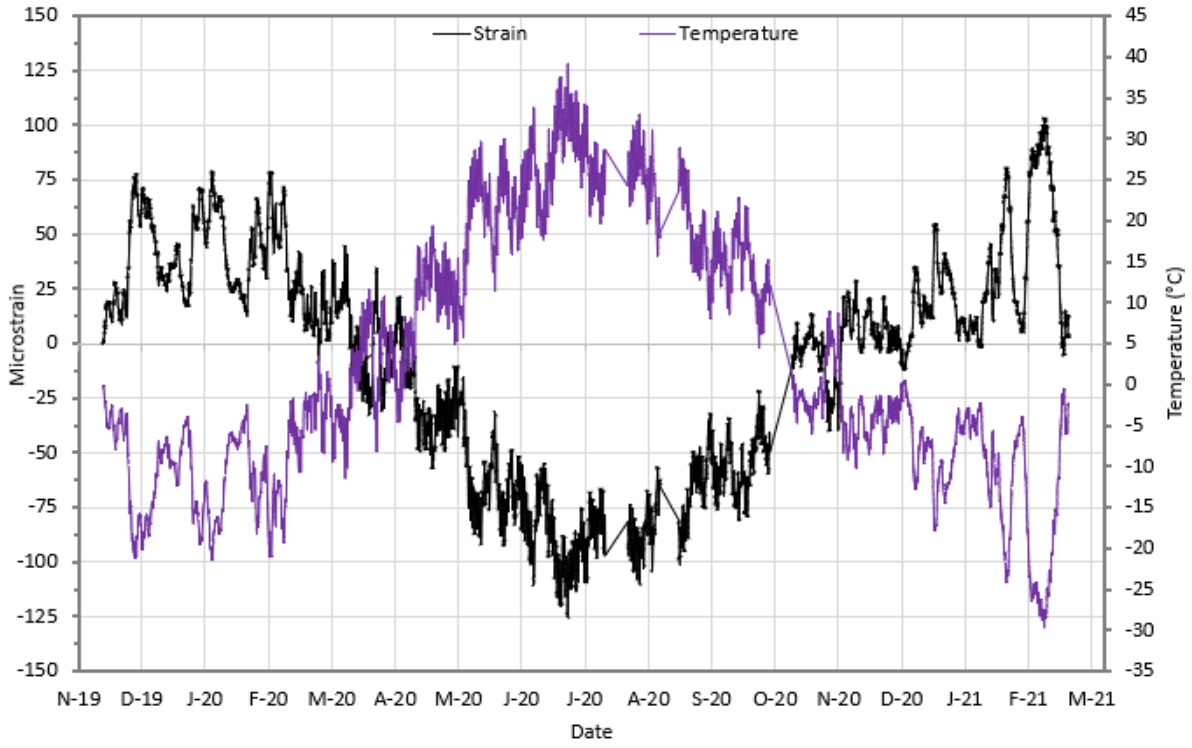

Figure 18: Shear Key 1 Longitudinal Strain @ Mid Span (Semendary et al. 2021)

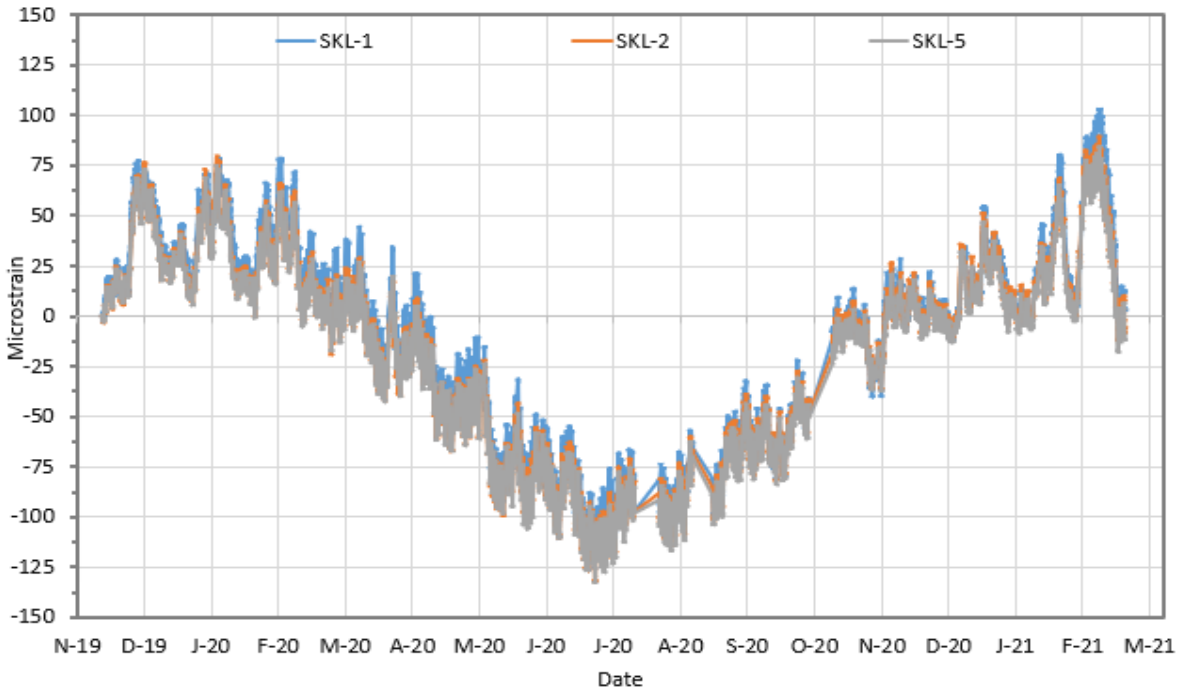

Figure 19: Shear Keys Longitudinal Strain @ Mid Span (Semendary et al. 2021)

When we examine the transverse strains across the shear keys, shown in Figure *20* and Figure *21* a similar pattern may be noted. As the temperature travels below zero the strain across the shear key generally forms tension and transitions to compression as the temperature gets warmer above zero degrees celcus. This data demonstrates that the peak time period for tension to form across the shear key is during cold weather events.

Similar to the longitudinal direction of loading, the peak mid span tensile strain in the transverse direction experienced by a shear key within the structure was 78 με on February 14th, 2021. The peak transverse compressive strain of -109 με occurred on July 3rd, 2020. The data further reveals that slightly higher peak strains were noted in the shear key over the support in the transverse shear key direction in both tension and compression at 85 με and -125 με respectively.

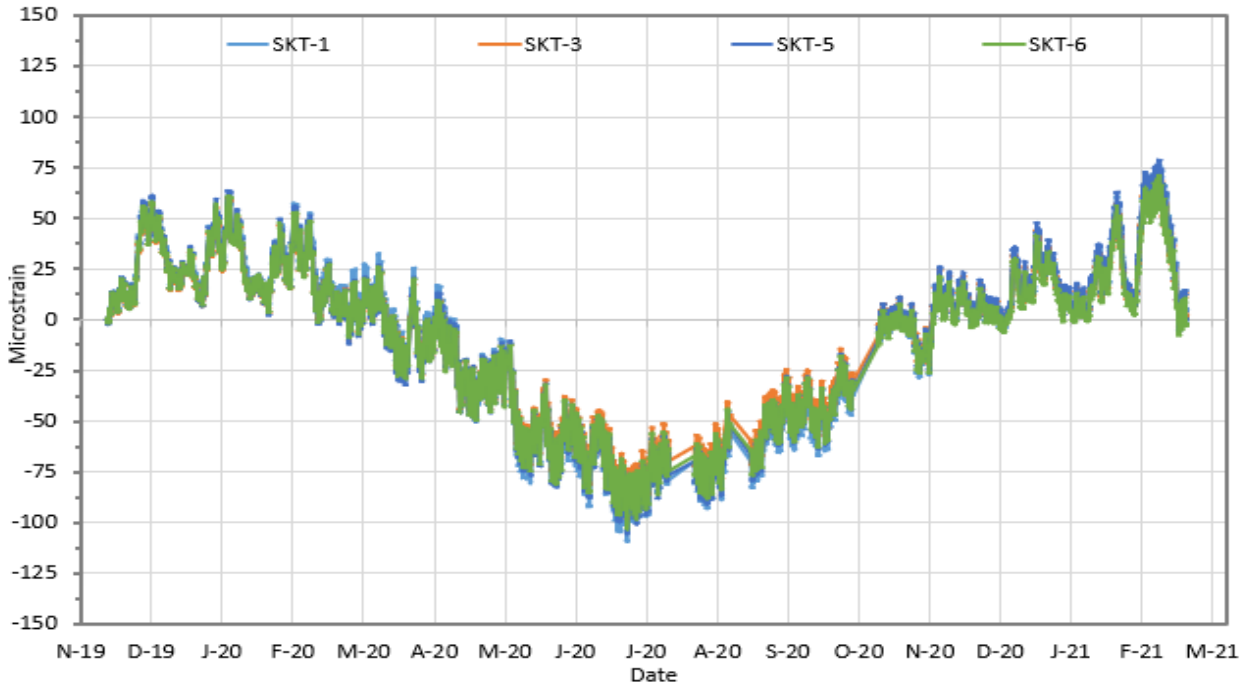

Figure 20: Shear Keys Transverse Strain @ Mid Span (Semendary et al. 2021)

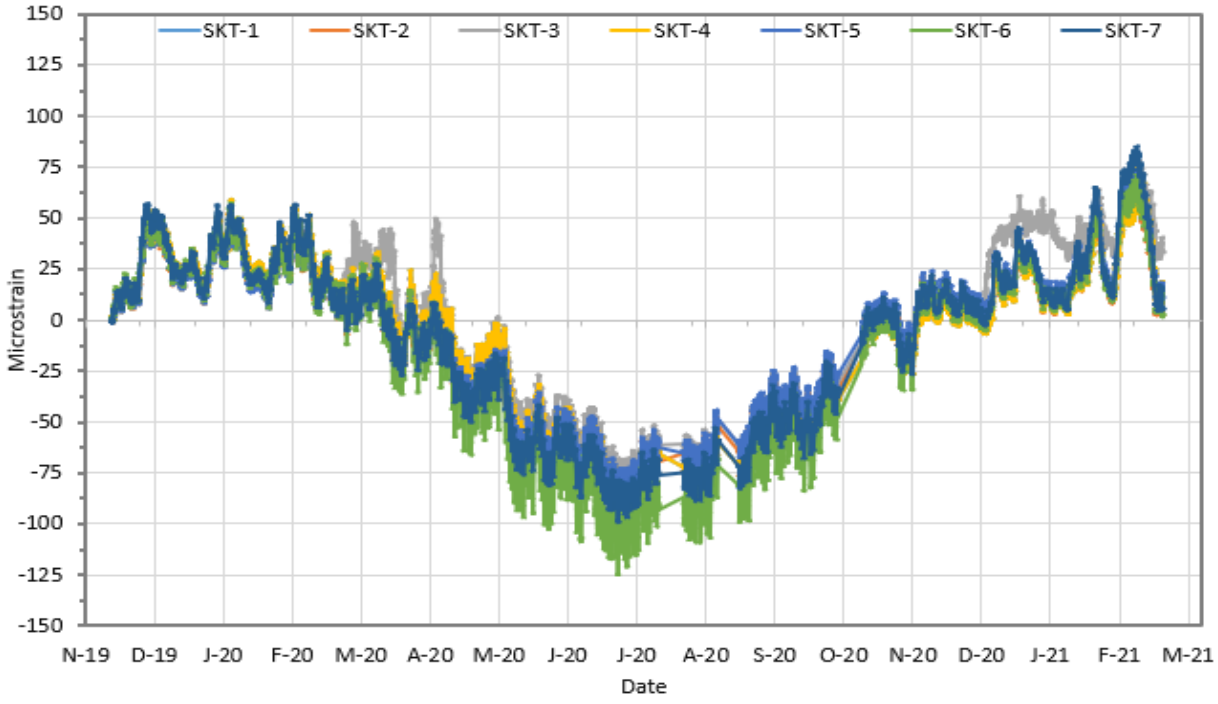

Figure 21: Shear Keys Transverse Strain @ support (Semendary et al. 2021)

Next, examining Figure *22* and Figure *23* some general trends can be noted as they relate to the longitudinal and transverse behaviour of the girder top flanges under cold weather conditions. These strains, similar to the shear key, demonstrate as the temperature transitions to below zero degrees Celsius longitudinal and transverse tension strain begins to form in the girder top flange. The strain and tension readings are a consistent mirror image of each other. As the ambient temperature heats up the behaviour transitions to compression in the top flange.

The peak tensile strain in the transverse direction experienced by the girder top flange was 328 με on February 14th, 2021 and in the longitudinal direction was 338 με on January 16th, 2021. The peak transverses compressive strain of -160 με and peak longitudinal compressive strain of -418 με in the girder top flange on July 3rd, 2020.

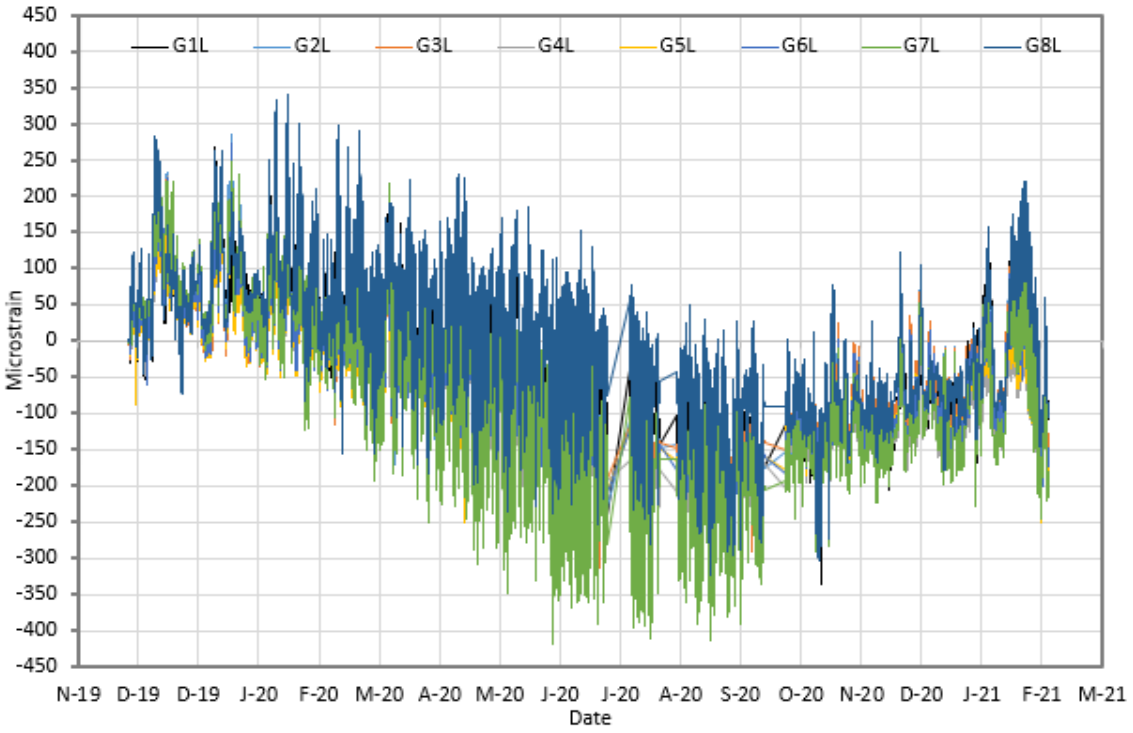

Figure 22: Girder Top Flange Longitudinal Strain @ Mid Span (Semendary et al. 2021)

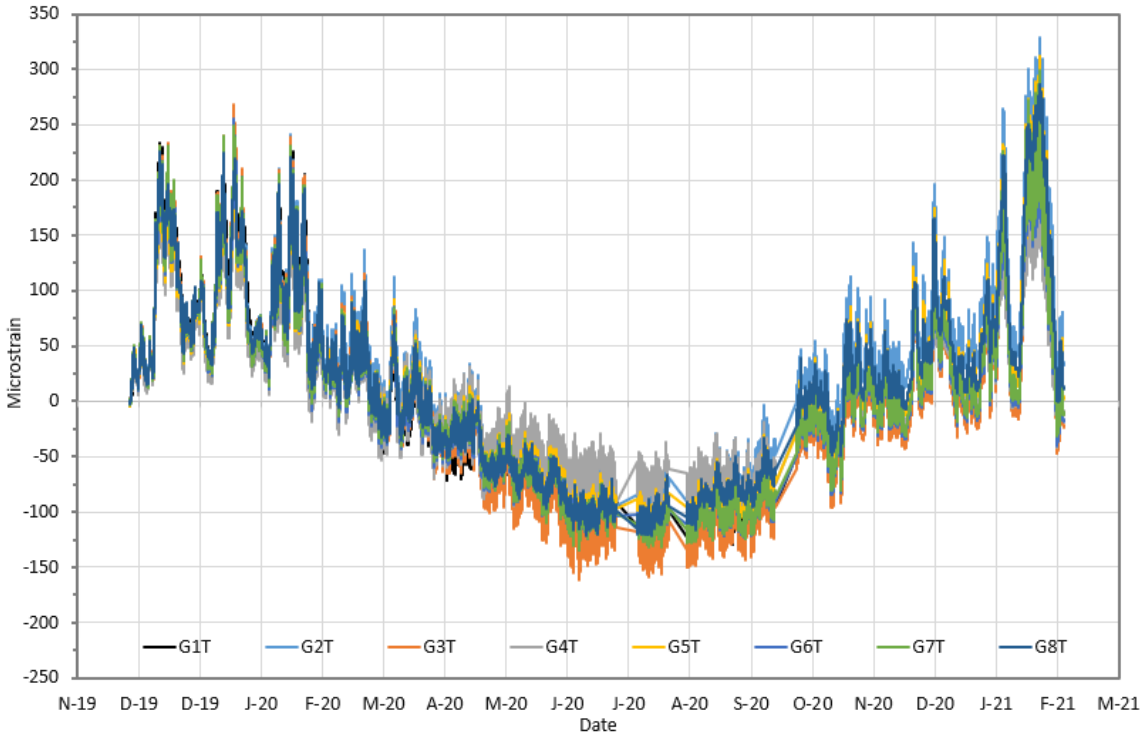

Figure 23: Girder Top Flange Transverse Strain @ Mid Span (Semendary et al. 2021)

Similar to the shear key and beam top flange strain behaviour, Figure *24* and Figure *25* shows the dowel strain, measured at mid span and over the span support. Looking at the naming convention “L” indicates a dowel off the left side of the beam flange and “R” refers to a dowel of the right side of the beam in question.

The data reveals that as the temperature transitions below zero degrees Celsius tension strain begins to form within the dowels. As the ambient temperature heats above zero degrees Celsius, the behaviour transitions to compression in the dowels. In addition, the magnitude of strain in the dowels at mid span and at the support do not feature any meaningful difference.

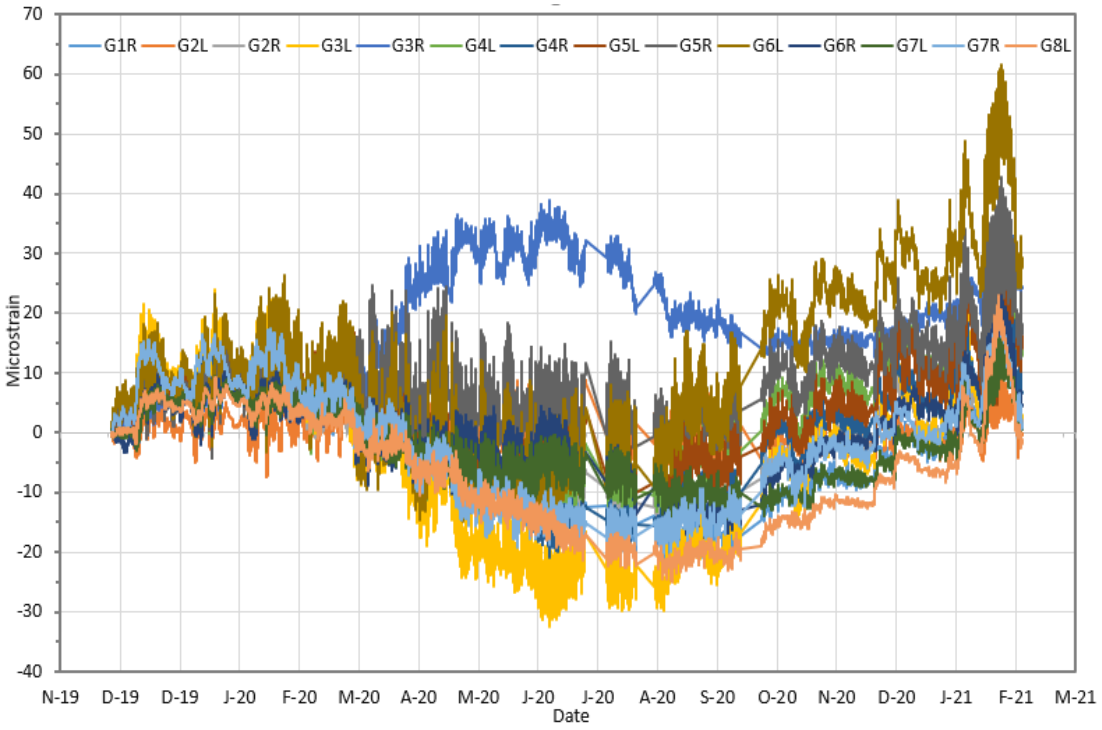

Figure 24: Dowel Bar Strain @ Mid Span (Semendary et al. 2021)

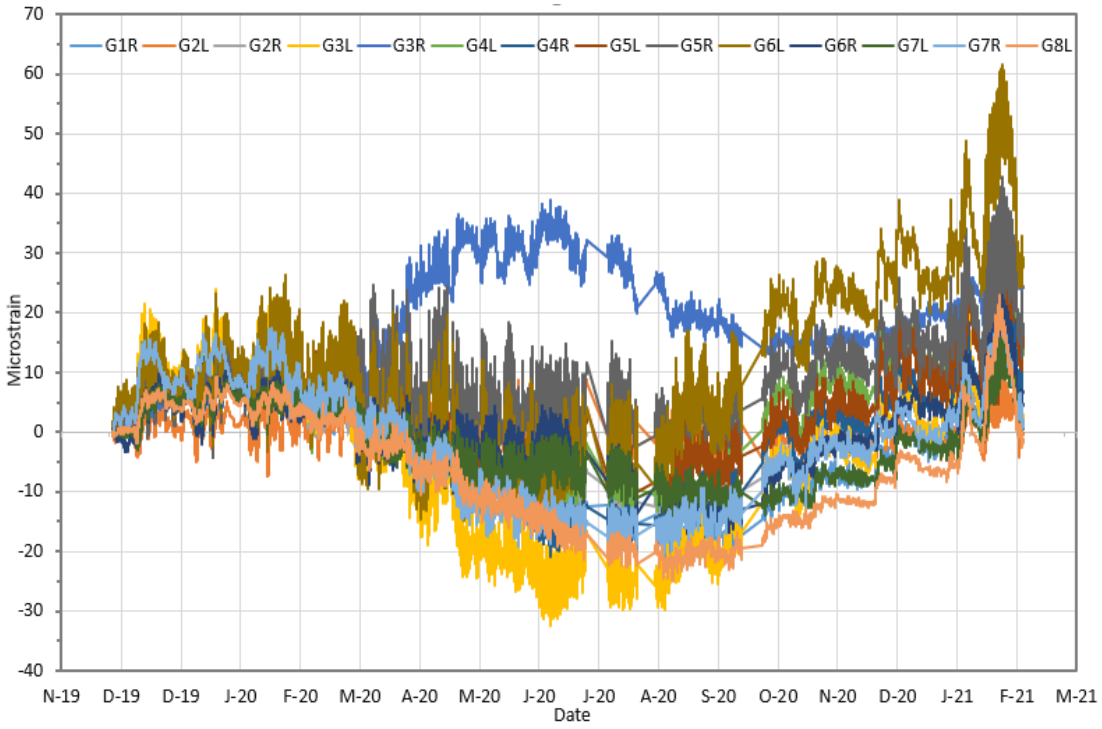

Figure 25: Dowel Bar Strain @ Support (Semendary et al. 2021)

3.4.2 Peak Structure strains

From the recorded data set a few dates can be chosen which contain the peak thermally induced strains experienced by the structure in both tension and in compression. These dates allow for the determination of critical temperature profiles on the bridge for further examination.

It was found that peak tension was experienced within the bridge on January 16th, 2020 and on February 14th, 2021. Peak compression was found on July 3rd, 2020. As a result of the recorded peaks and resultant temperature profile, these dates will form the basis of investigation within the finite element model calibration outlined in Section 4.1.

3.5 Temperature Profile Cases

Multiple temperature profile cases with respect to the depth of the box girder have been chosen based on the sensor data review in Section 3.4 to represent extreme strains within the structure from application of cold and hot temperature profiles. The corresponding delta strains between a neutral temperature case around zero across the cross-section depth and the extreme hot and cold cases are also provided. The delta strain results are critical to calibration of the proposed finite element model described in Section 3.8 and calibration process in Section 4.1.

3.5.1 Temperature Profile

The temperature profile with depth was measured within the bridge at mid span and locations show in Figure *16*, at locations 0 mm, 200 mm, 498 mm, 796 mm, 1100 mm, and 1200 mm measured from the bottom of the girder.

As outlined in Section 3.4.2 three representative temperature profile snapshots are chosen and provided in Table *6* and Table *7* below based on peak measured structure strains being experienced at these times. In reference to the naming convention in Figure *15*, the temperature profiles are measured on the exterior of beam 1 and between beam 3 and 4. Two of the profiles, on Jan 16, 2020 and Feb 14, 2021 are chosen to represent extreme tension strain from cold temperature profile, and July 3, 2021 is chosen to represent extreme compression strain from hot temperature profile. In addition, the measured delta strains between a consistent near zero temperature profile, on November 26, 2019 and the temperature profile in question is provided.

Table 6: Beam 1 Initial and Final Temperature Profiles

Depth (mm)	Temperature Profile (°C)			
	November 26th, 2019 @ 8:55 (initial)	January 16th, 2020 @ 11:00	July 3rd, 2020 @ 20:15	February 14th, 2021 @ 14:10
1200 (top)	1.048	-20.78	44.21	-27.55
1100	1.054	-22.92	46.6	-27.15
796	0.912	-24.19	45.91	-25.67
498	0.911	-24.56	45.01	-25.35
200	0.914	-24.63	43.01	-24.54
0	0.954	-23.42	38.83	-22.85

Table 7: Beam 4 Initial and Final Temperature Profiles

Depth (mm)	Temperature Profile (°C)			
	November 26th, 2019 @ 8:55 (initial)	January 16th, 2020 @ 11:00	July 3rd, 2020 @ 20:15	February 14th, 2021 @ 14:10
1200 (top)	1.435	-21.46	44.29	-25.08
1100	1.441	-20.77	43.03	-25.63
796	1.419	-18.505	38.12	-24.985
498	1.397	-16.24	33.21	-24.34
200	1.373	-18.58	32.3	-24.51
0	0.72	-21.08	32.45	-22.93

The temperature profile on Jan 16, 2020, shown in Figure *26*, features a colder west edge exterior beam 1, possibly due to the insulating effect of the surrounding girders and fluctuation of atmospheric temperature during the time frame. The temperature at the top of the girder, at -20.78℃, is about 3℃ warmer than the underside flange of the girder at -23.42 ℃. The core of the bridge mass reached a warm point of -16.24 ℃ (beam 4).

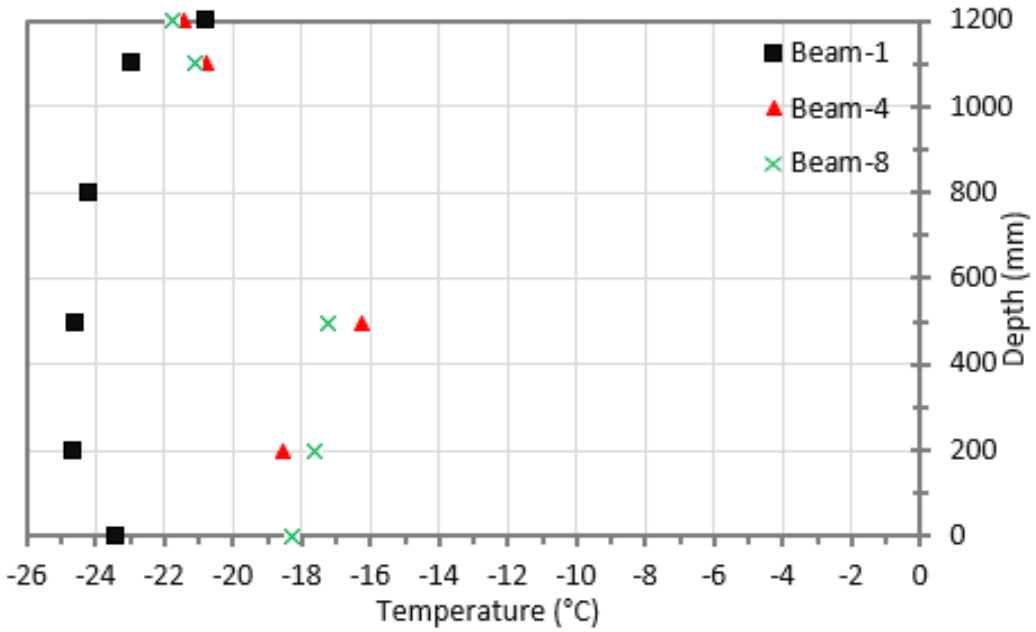

Figure 26: Mid Span Temperature Profile – January 16, 2020 (Semendary et al. 2021)

The temperature profile on Feb 14, 2021, shown in Figure *27*, features a similar temperature profile between the exterior beam 1 and the interior beam 4. This temperature consistency between the interior and exterior girders is consistent with the duration of extreme cold temperature during the time period. The temperature is also fairly linear between the top and bottom of the girder ranging between -27.55℃ at the top of the girder and –22.85℃ at the bottom of the girder

In both the January 16, 2020 and Feb 14, 2021 cases it can be noted that the temperature from beam 8, the east exterior edge of the bridge, is consistently warmer then the west edge. This effect may be partially explained by the duration of sunlight impacting the east versus west edges of the bridge as the sun rises in the east and sets in the west. In addition, the sun tends to set late afternoon to early evening in the winter months.

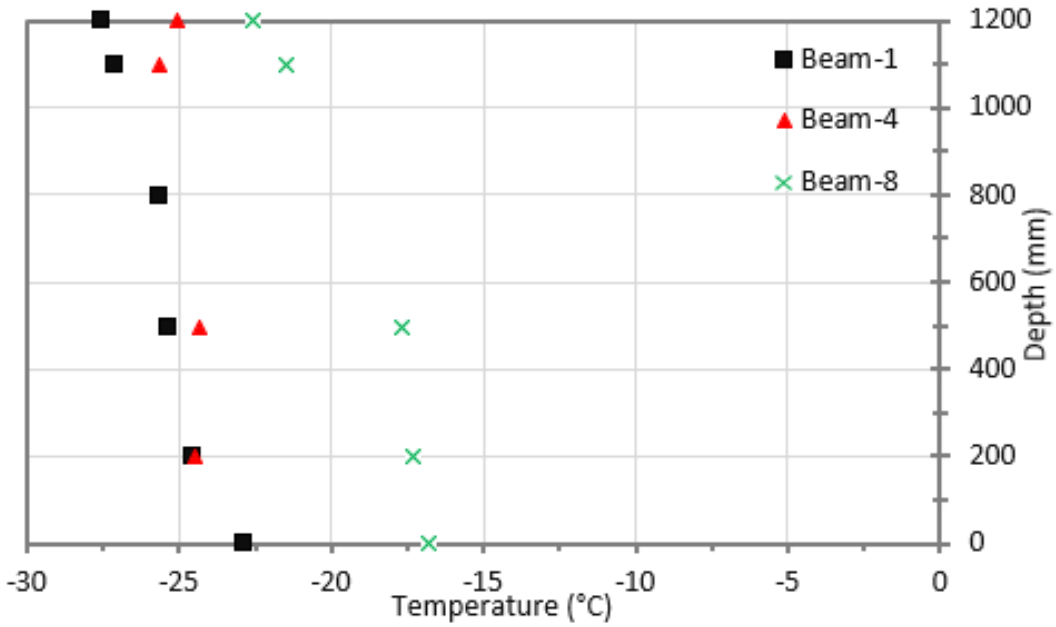

Figure 27: Mid Span Temperature Profile – February 14, 2021 (Semendary et al. 2021)

Finally for reference, a warm weather case is presented in Figure *28*. The exterior girder line reached higher temperatures, possibly due to the sun beating on the exterior girder, heating it up in the direct sun. The exterior girder top flange reached a temperature of 44.21 ℃ while the bottom flange reached 38.83 ℃ . Across the bridge towards the centreline, the girder reached 44.29 ℃ at the top flange and 32.4 ℃ at the bottom flange. The interior girder cooled with depth, indicating that the insulating effect of concrete provided a cooler bridge underside, as expected.

Beam 1, on the west side of the bridge, experiences a warmer temperature profile then beam 8, on the east side of the bridge. This may be rationalized by the fact that summer months have sunlight well into the evening in Manitoba, and the peak temperatures tend to occur towards the late afternoon when the sun would be beating directly on the west girder. This contrasts with the winter months where the sun sets very early and colder weather can be experienced in the evening, as demonstrated by the cold weather cases where beam 1 on the west side of the bridge was colder than beam 8 on the east side of the bridge.

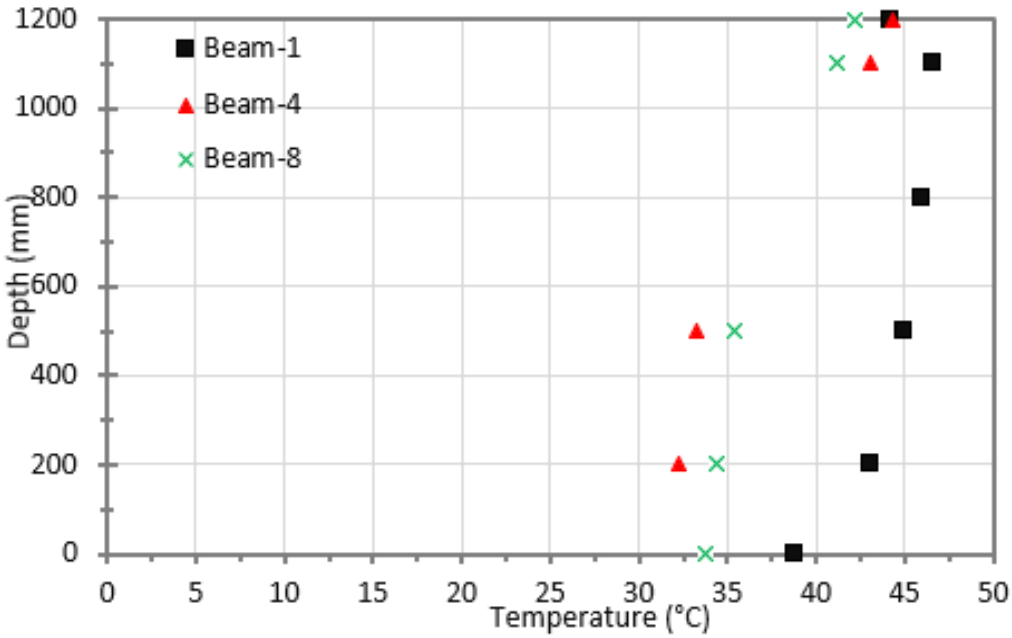

Figure 28: Mid Span Temperature Profile – July 3, 2020 (Semendary et al. 2021)

3.5.2 Temperature profile Strain Data

The following *Figure 29* to Figure *33* provide the strains for each direction of action within the shear key and girders for the three chosen temperature profile cases. These figures show the exact measured strains and are used for comparison within the finite element

modelling calibration. More detailed discussion of overall bridge strain response to thermal loading is provided within Section 3.4.

Figure *29* and Figure *30* show the girder transverse top and bottom flange strains within the bridge girders. Examining the cold weather temperature profiles, the highest transverse tension strain within the top flange is experienced in beam 2 on February 14th, 2021. Overall, the tension strain within these cold weather temperature profiles is relatively stable across the width of the bridge with no discernable pattern of strain fluctuation between girders within the top flanges.

Similarly, beam 2 also experiences the highest tension strain within the bottom flange. Overall, the bottom flange tension strain generally reduces as you travel to the east edge of the structure where beam 8 is located. These measured strains are in line with the temperature profiles which demonstrate the west edge of the bridge (beam 1) gets colder than the east side of the bridge (beam 8). As a result, higher transverse tension strain would be expected to occur within the west side of the bridge.

The highest transverse compression strain in both the top and bottom flanges is experienced within beam 3 at the July 3rd, 2020 temperature profile. Generally, more compression strain is experienced within the west side of the bridge (beam 1) then the east side of the bridge (beam 8). This is in line with more thermal expansion occurring on the west side when compared to the east side as shown within Figure *28*.

Within each of the figures the table across the bottom summarizes the values shown within the bar chart for each of the three temperatures profiles chosen from the overall dataset of field monitored strains.

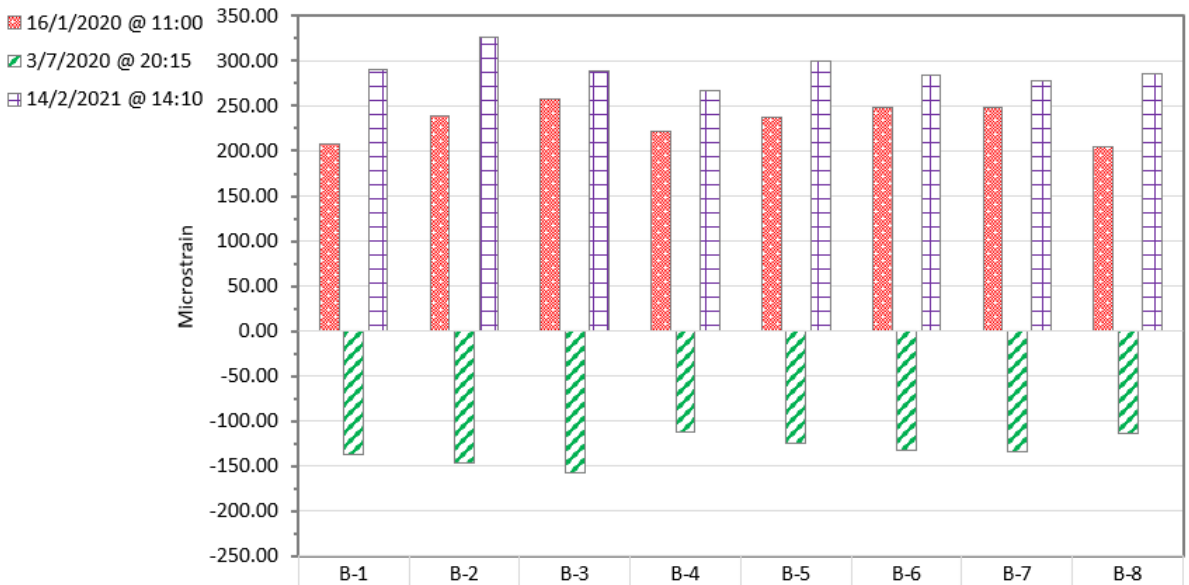

	B-1	B-2	B-3	B-4	B-5	B-6	B-7	B-8
16/1/2020 @ 11:00	207.22	238.72	258.15	221.66	238.00	247.87	247.96	204.88
3/7/2020 @ 20:15	-137.49	-145.87	-157.91	-112.73	-124.76	-132.12	-133.23	-114.02
14/2/2021 @ 14:10	291.10	325.62	288.85	267.30	299.86	284.20	277.99	286.34

Figure 29: Transverse Top Flange Strain in the Girders at Mid Span (Semendary et al. 2021)

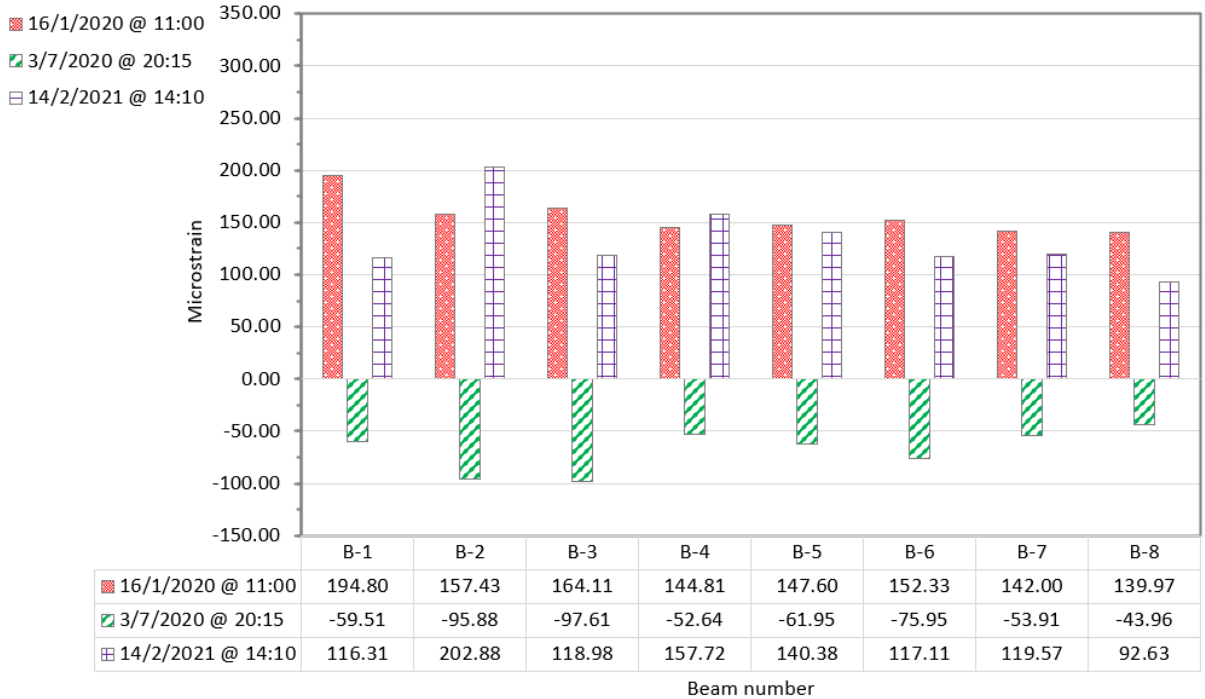

	B-1	B-2	B-3	B-4	B-5	B-6	B-7	B-8
16/1/2020 @ 11:00	194.80	157.43	164.11	144.81	147.60	152.33	142.00	139.97
3/7/2020 @ 20:15	-59.51	-95.88	-97.61	-52.64	-61.95	-75.95	-53.91	-43.96
14/2/2021 @ 14:10	116.31	202.88	118.98	157.72	140.38	117.11	119.57	92.63

Figure 30: Transverse Bottom Strain in the Beams at Mid Span (Semendary et al. 2021)

Figure *31* and Figure *32* show the longitudinal top and bottom flange strains within the girders. Examining the cold weather temperature profiles, the highest longitudinal tension strain within the top flange is experienced in beam 2 on January 16th, 2020. This is supported by the thermal gradient for the day featuring a colder temperature at the west side of the bridge (beam 1) compared to the east (beam 8).

In contrast the strains mimic the thermal gradients for the February 14th, 2021 case throughout the bridge mass. Under this case, the center of the bridge was generally warmer than the exterior faces. The strains show less tension at the interior girders and more at the exterior girders matching the temperature profile. The recorded bottom flange longitudinal strains generally match in behaviour to the top flange but at a lower magnitude of strain. In contrast, the warm weather profile reveals the highest top flange compression strain was found within girder beam 7 with most longitudinal strains within the girder of similar magnitude at the other girders.

The longitudinal bottom flange strains were generally stable, although they were only measured at beams 1 through 4. The exterior west edge (beam 1) featured higher magnitude of strain then the centre girders under all temperature profiles. The direction of strain action was the same as the top flange (tension / compression) however the magnitude of bottom flange strains was generally lower than the top flange, indicating that rotation through the cross section, and related bending moment is being induced.

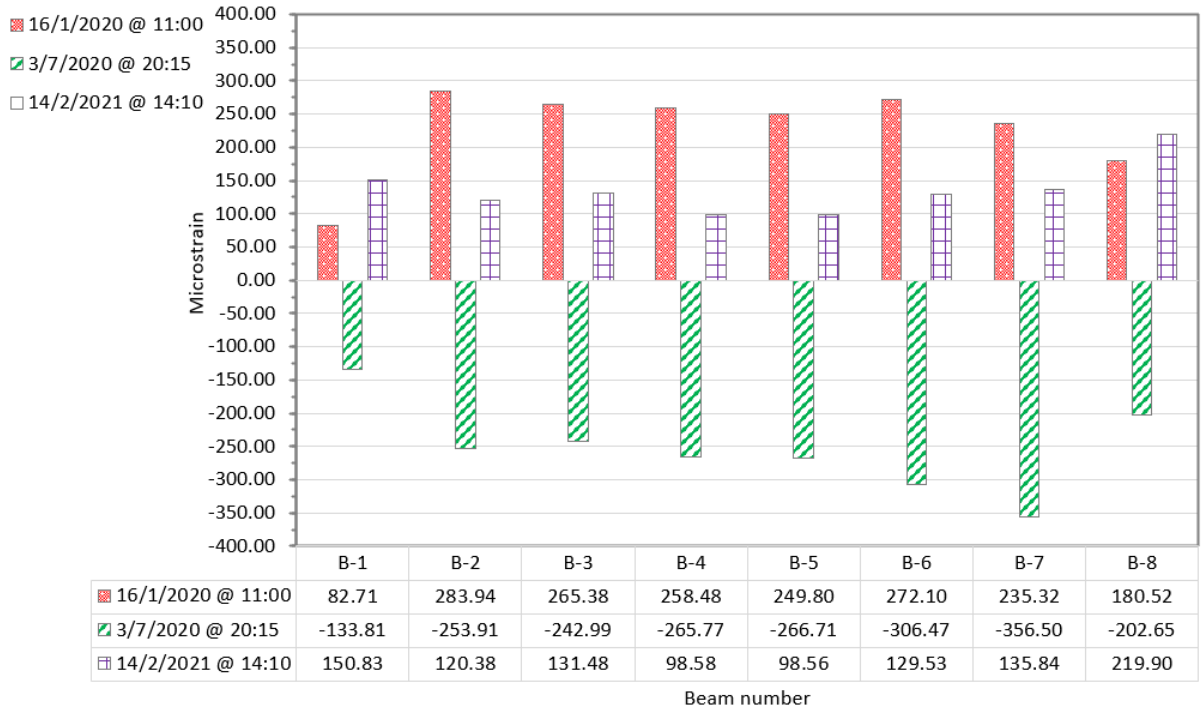

	B-1	B-2	B-3	B-4	B-5	B-6	B-7	B-8
16/1/2020 @ 11:00	82.71	283.94	265.38	258.48	249.80	272.10	235.32	180.52
3/7/2020 @ 20:15	-133.81	-253.91	-242.99	-265.77	-266.71	-306.47	-356.50	-202.65
14/2/2021 @ 14:10	150.83	120.38	131.48	98.58	98.56	129.53	135.84	219.90

Figure 31: Longitudinal Top Strain in the Beam at Mid Span (Semendary et al. 2021)

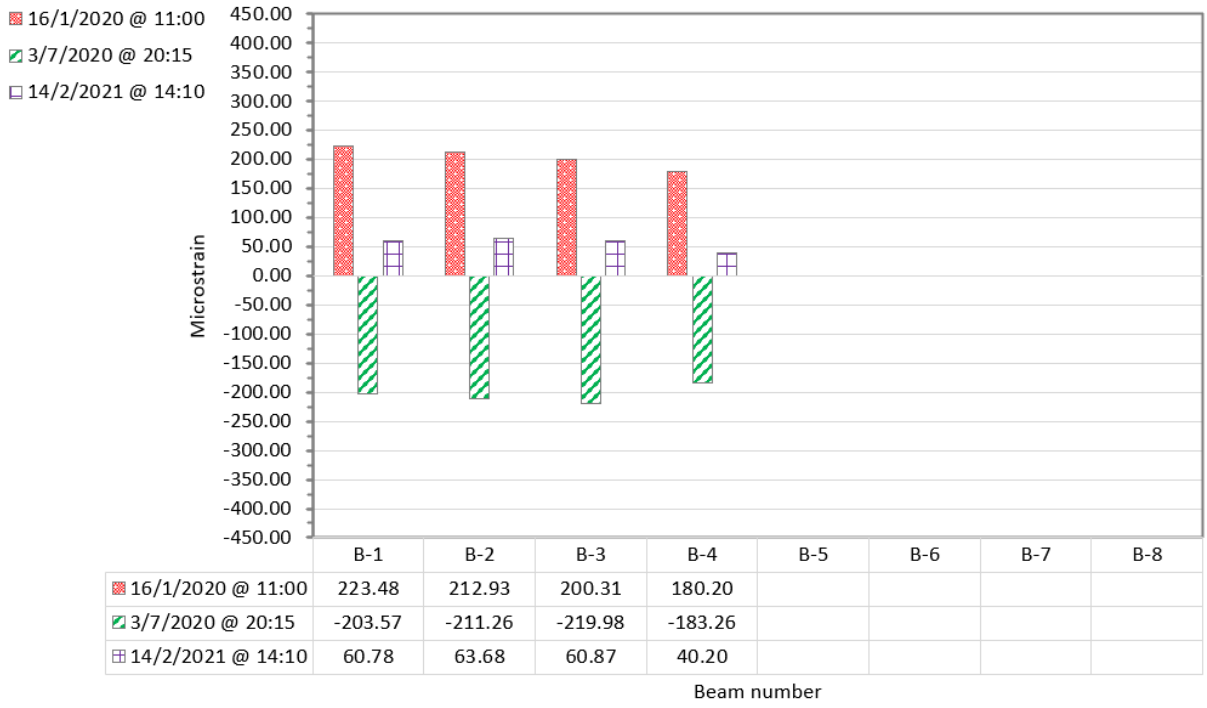

	B-1	B-2	B-3	B-4	B-5	B-6	B-7	B-8
16/1/2020 @ 11:00	223.48	212.93	200.31	180.20				
3/7/2020 @ 20:15	-203.57	-211.26	-219.98	-183.26				
14/2/2021 @ 14:10	60.78	63.68	60.87	40.20				

Figure 32: Longitudinal Bottom Strain in the Beams at Mid Span (Semendary et al. 2021)

Figure *33* shows the longitudinal shear key strains while Figure *34* to Figure *36* shows transverse strains across each of the shear keys and the strains within the dowels at mid span and at the bridge span support. The bottom axis indicates the shear key or girder beam number, the “L” or “R” denotes if it is the dowel off the left or right side of girder, and the vertical axis indicates the strain in question. These figures provide some insights into how the bridge shear keys are responding to temperature profile.

Examining the cold weather temperature profiles, the highest longitudinal tension strain within the shear key is experienced in Shear Key 1 and Shear Key 7 on February 14th, 2021. This coincides with the coldest on record temperature event within the data set, where the temperature was consistent throughout the bridge mass.

As a result the tension strain being similar within the east and west most shear keys makes sense. The warm weather temperature profile, on July 3, 2020 featured similar consistency of strain magnitude between the shear keys with the peak compression strain being higher at the interior shear keys compared to the exterior shear keys.

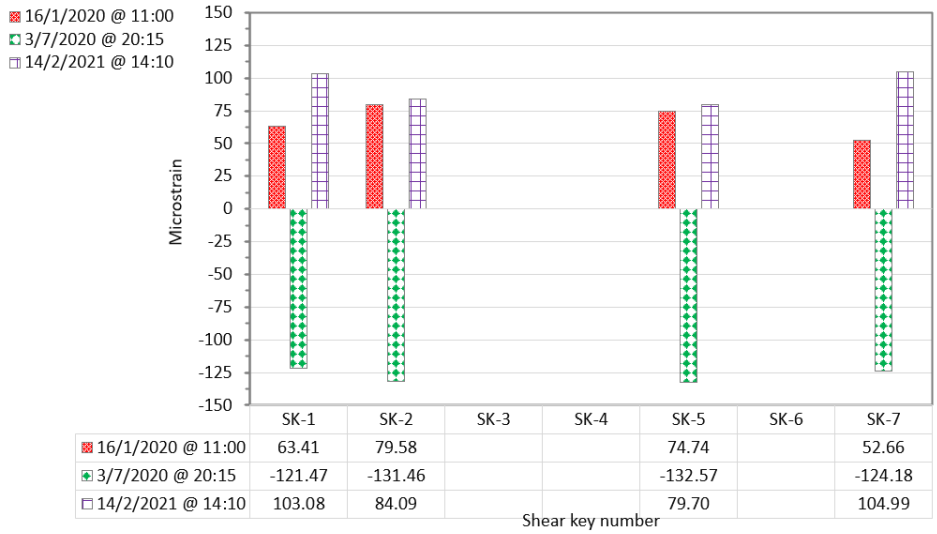

	SK-1	SK-2	SK-3	SK-4	SK-5	SK-6	SK-7
16/1/2020 @ 11:00	63.41	79.58			74.74		52.66
3/7/2020 @ 20:15	-121.47	-131.46			-132.57		-124.18
14/2/2021 @ 14:10	103.08	84.09			79.70		104.99

Figure 33: Longitudinal Shear Key Strain at Mid Span (Semendary et al. 2021)

From Figure *34* through Figure *36* it is clear that under each of the temperature profile cases each of the shear keys experience higher strain magnitude then that measured within the dowels. This indicates that bond is playing an important role in strain transfer across the shear key. All shear keys within the structure experience a similar level of strain magnitude with no real pattern of magnitude change.

As the bridge undergoes cold weather temperature profiles on January 16, 2020 and February 14, 2021, tension forms within all of the dowels and within all of the shear keys. The same cannot be said for the warm weather case where some tension and some compression was measured within the dowels, with all shear keys measuring compression.

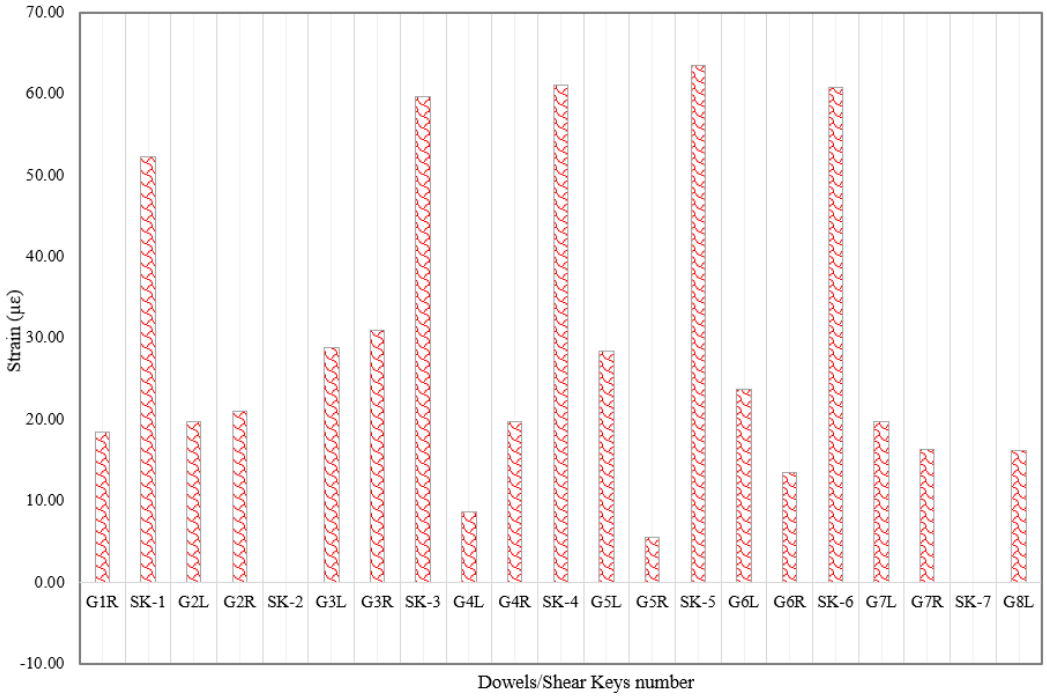

Figure 34: Dowel/shear key strain at mid span for data collected on January 16, 2020 at 11:00 (Semendary et al. 2021)

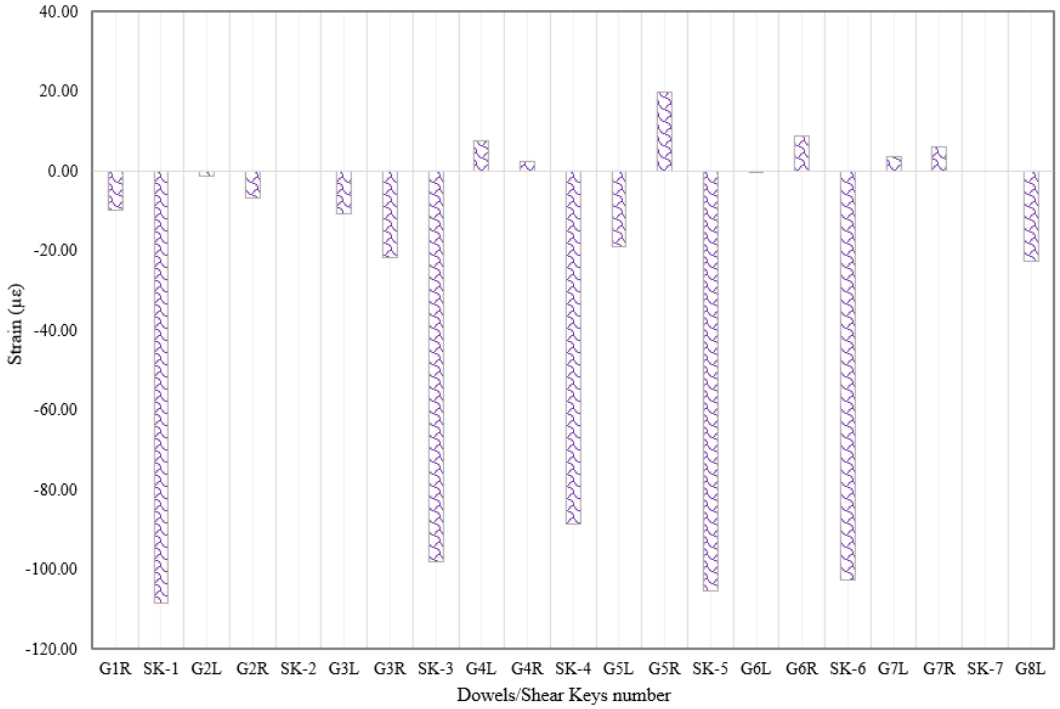

Figure 35: Dowel/shear key strain at mid span for data collected on July 3, 2020 at 20:15 (Semendary et al. 2021)

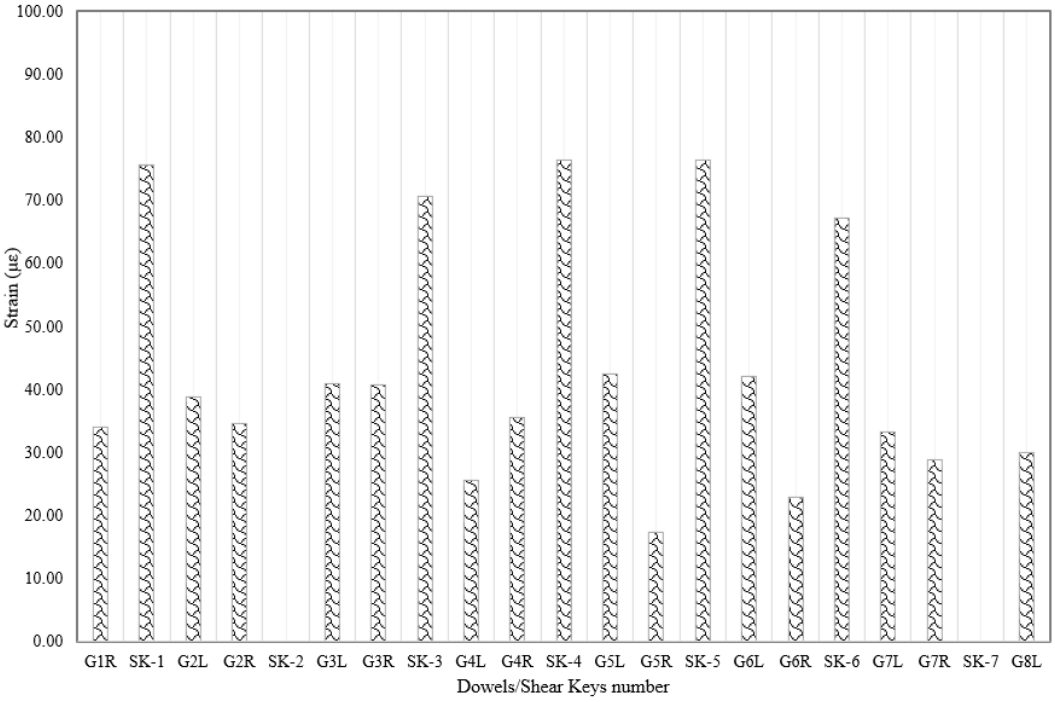

Figure 36: Dowel/shear key strain at mid span for data collected on February 14, 2021 at 14:10 (Semendary et al. 2021)

3.5.3 Structure Behaviour Trends Under Temperature Profiles

Overall, from all the graphs we can establish some trends of behavior within the structure subjected to temperature profile effects outlined in Section 3.5.1. Generally, the following can be found:

- As the temperature decreases below zero tensile strain forms in the longitudinal and transverse bridge span direction in both the top and bottom flanges of the girder and across the shear key.
- As the temperature increases above zero compressive strain forms in the transverse and longitudinal bridge span direction in both the top flange, bottom flange, and shear key.
- The dowels respond to temperature gradient by forming tension in their local axial direction under cold weather events and compression along their local axial direction under warm weather events.
- The magnitude of strain in the dowel is far lower than that of the shear key and girder top flange. This possibly indicates that most of the force due to temperature across the interface is taken by the bond between UHPC and HSC.

3.6 Material Properties

Laboratory material testing was conducted on both the UHPC and HPC girder material used within the Little Morris River Bridge construction as part of the overall research team project work. This material testing program, completed by Li Xin Tan, is summarized within the paper titled, “Estimation of bond strengths and design parameters for precast concrete-UHPC shear key interface in box beam bridge”, by Tan

et al. (Tan, Semendary and Svecova 2021). Additional information is found in Tan's thesis (Tan 2021) titled, "Early Age Durability Study of the Bond Strength on the Interface between UHPC-HSC."

Tan studied both the concrete girder and the shear key UHPC material in a comprehensive testing program including the following:

- Direct Tension testing in accordance with ASTM C1404/C1404M-98 (withdrawn standard);
- Pull off testing in accordance with ASTM C1583/C1583M;
- Slant Shear Testing in accordance with ASTM C882; and
- Direct shear testing utilizing the bi-shear test method.

The following sections summarizes the results of the program and material properties of the Little Morris River Bridge. The original paper and thesis should be referred to for a complete understanding of the work completed. These material test results form the basis of the girder and shear key material properties utilized in the finite element model. These properties are also fundamental to the developed traction separation model discussed further in Section 3.7 to represent the bond interaction between the shear key and girder within the finite element model. As this thesis focuses on a study of long-term behaviour, the presented test results are discussed in the context of long-term bridge behaviour as they relate to this study.

3.6.1 HSC Box Girder Mechanical Properties

The 28-day compressive strength, modulus of elasticity, poisson's ratio, and splitting tensile strength is listed below in Table 8 for each of the girders using the girder reference numbers in Figure 15. The Poisson Ratio and modulus of elasticity of the HSC were calculated in accordance with ASTM C469 (2014).

Table 8: Box Girder HSC Properties (From Tan, 2021)

Girder	Average Compressive Strength from U of M Lab (MPa)	Lafarge Day 28 Average Compressive Strength (Mpa)	Average Modulus of Elasticity (Mpa)	Poisson's Ratio	Splitting Tensile Strength (Mpa)
1	75.7	74.5	36,700	0.28	5.52
2	86.9	88.1	40,000	0.26	5.52
3	71.9	86.2	N/A	N/A	N/A
4	70.8	77.2	36,700	0.26	5.15
5	73.9	80.2	N/A	N/A	4.79
6	75.6	81.4	37,400	0.27	5.66
7	86.3	77.4	N/A	N/A	N/A
8	73.6	84.0	N/A	N/A	N/A

With respect to the above table, the measured Poisson's ratio at 28 days is above the Canadian bridge code CAN / CSA S6-19 recommendation of 0.2 Poisson's ratio and commentary indicating that typical poisons ratios range between 0.15 and 0.2 (CSA 2019). Looking at the literature, the higher values in Table *8* can be explained by the early age at which the ratio was measured. Dependent on the mix design, curing conditions, and level of loading, poison's ratios tend to decrease with time and settle around 0.15-0.2 in the long term (Persson 1999). Results as low as 0.1 have been reported in SCC mix designs (Mazzoti and Savoia 2012).

3.6.2 UHPC Mechanical Properties

The compressive strength and modulus of elasticity of the UHPC was tested at six different ages between day 1 and 91 days as shown in Table *9*. As this is a study of long-term behaviour of the shear key the increase in strength and elasticity with age is an important factor in the modeling of the structure. The 91-day age strength was found to be 164.2 MPa. The Modulus of Elasticity was found to be 58,721 MPa. The modulus of elasticity of the UHPC was calculated in accordance with the formula within ASTM C469(2014).

The UHPC poisons ratio was not measured as part of this study. However, the literature indicates that a poisons ratio ranging between 0.16 and 0.21 has been historically found to describe the behaviour of the UHPC (Graybeal and Russell 2013).

Table 9: UHPC Shear Key Properties (From Tan, 2021)

Date of Casting	UHPC Age (days)	Average Compressive Strength (MPa)	Average Modulus of Elasticity (MPa)
30-Jul, 2019	1	14.7	16400
30-Jul, 2019	3	106.3	42300
30-Jul, 2019	7	138.2	N/A
30-Jul, 2019	14	146.4	N/A
30-Jul, 2019	28	164.4	N/A
01-Aug, 2019	1	43.5	28300
01-Aug, 2019	5	125.1	43400
01-Aug, 2019	7	135.0	45600
01-Aug, 2019	14	167.9	51000
01-Aug, 2019	28	152.7	50400
01-Aug, 2019	91	164.2	58700

As this is a long-term study of the UHPC shear key behaviour, an indication of the modulus of elasticity between casting of the shear key and the thermal cases

considered in Section 3.5 between 6 months and 18 months following casting is required in order to calibrate a finite element model of the structure behaviour. Multiple projections have been made to determine a feasible range for the modulus of elasticity.

Figure *37* contains a regression curve to predict the modulus using all the test result. The curve achieves an r^2 value of 0.8325. It is clear from the curve that it overpredicts the results at 91 days and should be considered an upper bound. The curve predicts a 6-month elasticity of 68 068 MPa and 18-month elasticity of 76 703 MPa. Figure *38* contains a similar regression curve eliminating the day 1 test results. This curve achieved a r^2 value of 0.9516. Looking at the curve it underpredicts the day 91 elasticity and should be considered closer to a lower bound of actual long term elasticity. The curve predicts a 6-month elasticity of 61 364 MPa and 18-month elasticity of 66 602 MPa.

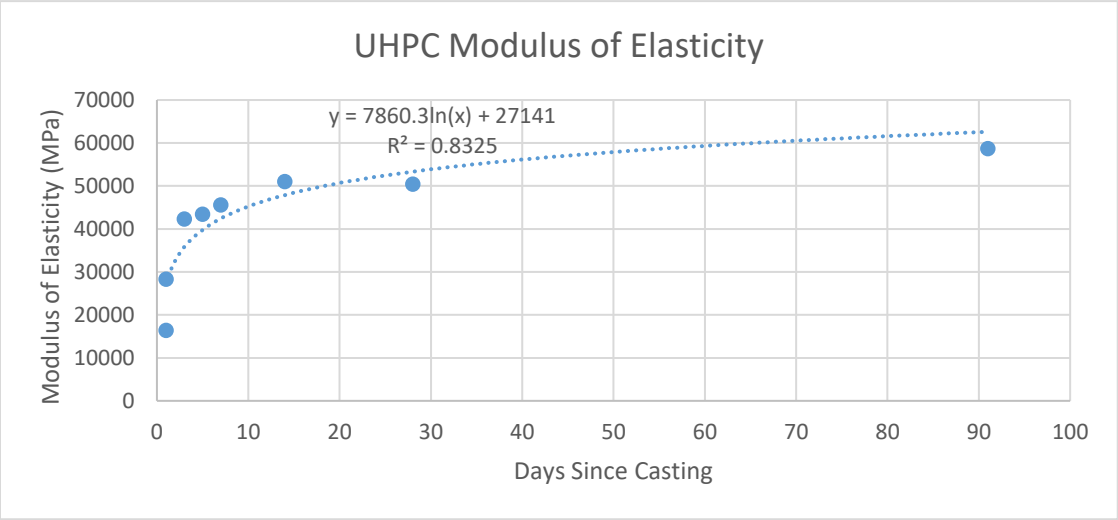

Figure 37: Modulus of Elasticity Regression – All Data

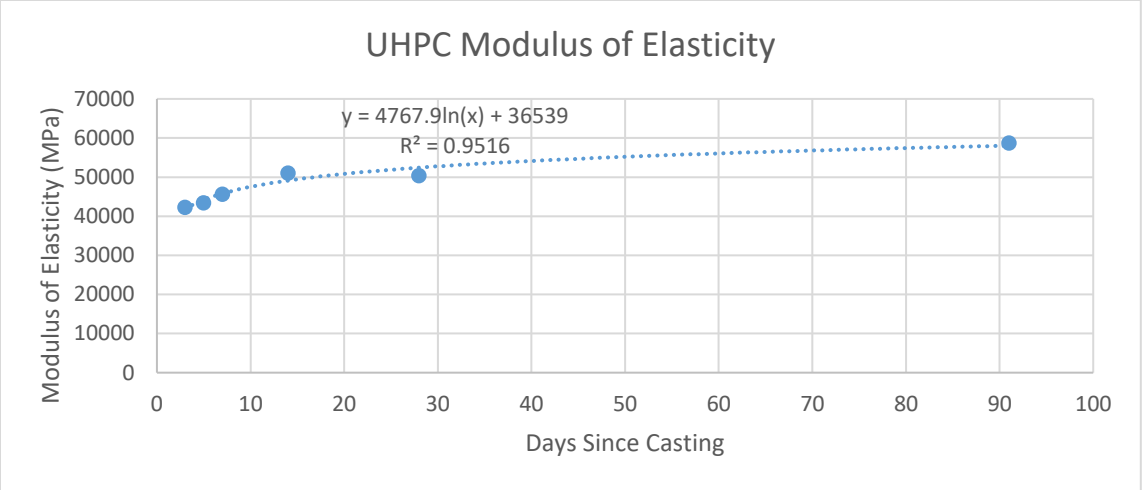

Figure 38: Modulus of Elasticity Regression – 3 Day to 91 Day Data

3.6.3 UHPC Tensile Mechanical Properties

Samples of the UHPC taken at time of shear key casting were tested in direct tension and in pull off tests at various ages. The results of direct tension are in Table 10 and pull off are shown in Table 11. The average tensile strength at 91 days was found to be 2.9 MPa when tested in direct tension and 3.8 MPa when tested under pull off. There was an unexplained decrease in tensile strength on days 28 and 91 in the direct tension test setup.

Table 10: Direct Tension Test Results (From Tan, 2021)

UHPC Age (days)	Number of Tested Specimens	Average Tensile Strength (MPa)	STD (MPa)	COV
5	5	3.6	0.7	19%
7	3	3.9	0.5	13%
14	6	3.9	0.7	18%
28	6	2.5	0.8	30%
91	6	2.9	0.6	20%
STD = Standard Deviation COV = Coefficient of Variation				

Table 11: Pull off Test Results (From Tan, 2021)

UHPC Age (days)	Number of Tested Specimens	Average Tensile Strength (MPa)	STD (MPa)	COV
5	1	3.87	-	-
7	6	5.20	0.30	6%
14	6	4.33	0.57	13%
28	5	3.88	0.48	12%
91	7	3.80	0.44	12%
STD = Standard Deviation COV = Coefficient of Variation				

3.6.4 Slant Shear Mechanical Properties

Slant shear testing was completed on specimens in accordance with ASTM C882 to evaluate the performance of the shear key connection under combined shear and compression loading. Slant shear tests were performed on 34 specimens at different ages. Four specimens were tested at 91 days with an average shear strength found of 23 MPa at 91 days. Table 12 shows the average shear stress and standard deviation at each age of UHPC.

Table 12: Slant Shear Test Results (From Tan, 2021)

UHPC Age (days)	Average Slant Shear Strength (MPa)	Average σ (MPa)	Average τ (MPa)	STD σ (MPa)	STD τ (MPa)	COV σ & τ
1	20	10.1	17.4	2.4	4.2	24%
5	24	12.2	21.1	2.2	3.8	18%
7	30.6	15.6	27.0	3.1	5.4	20%
14	27.4	13.8	23.9	2.1	3.6	15%
28	31.4	16.4	28.4	3.2	5.5	19%
91	25.9	13.3	23.0	2.0	3.5	15%
σ = Normal Stress STD = Standard Deviation τ = Shear Stress COV = Coefficient of Variation						

3.6.5 Bi-Shear Mechanical Properties

The Bi-shear tests were conducted on 42 specimens with 4 specimens tested at 91 days. The Bi-shear test provides an indication of the minimum bond strength of the UHPC to HSC interface due to direct shear. The average shear strength at 91 days was found to be 6.63 MPa, however, the completed tests had a quite wide standard deviation of 2.12 MPa. Table 13 summarizes the results of the completed bi-shear tests.

Table 13: Bi-Shear Test Results (From Tan, 2021)

UHPC Age (days)	Number of Specimens	Average Shear Strength	STD (MPa)	COV
1	6	3.45	1.53	44%
5	6	3.75	1.10	29%
7	6	4.42	1.22	28%
14	6	4.71	1.66	35%
28	6	5.53	3.02	55%
91	4	6.63	2.12	32%
STD = Standard Deviation COV = Coefficient of Variation				

3.7 Bond Behaviour and Traction Separation Interaction Model

From the results of the materials testing program completed by Tan, a model can be developed to represent the shear key behaviour under loading for the purposes of finite element modeling.

Surface based cohesion is represented by a traction separation model, which allows for the debonding failure mode to be represented within the finite element model. Buildup of strains and resultant stresses at the interface is represented by compressive and friction

models. In the model formulation considered in this study, the compressive and friction model considers a coefficient of friction of 1.0. This is in line with CSA S6-19 Surface condition 2, concrete placed against hardened concrete, with the surface clean and free of laitance and intentionally roughened to a full amplitude of about 5 mm and a spacing of about 15 mm, outlined in Table *2*.

It is useful to reiterate what a traction separation model facilitates in finite element analysis. The traction separation model is a methodology of modeling the interaction between two materials, in this case the UHPC and girder concrete materials under stress and allows for the representation of a debonding failure mode between the two materials (Sudziak, Jackiewicz-Rek and Kozyra 2021). This model first considers the interaction between materials using linear elastic behaviour up to a point of damage initiation which is then followed by the evolution of damage and corresponding change in behaviour at the interface. Following the onset of damage initiation, denoted by the peak traction force, damage evolution is then considered by the model. The use of this modeling technique was validated for the interaction of girder concrete and UHPC completed in similar applications by Semendary *et al*. (Semendary, Steinberg, et al. 2019).

The results from the direct tension test, slant shear test, and bi-shear test can be used to represent the stiffness response and failure criterion in each relevant direction of loading. The following Figure *39* to Figure *41* depict the test setup and schematic direction of loading for each of the test forming a useful reference point for discussion.

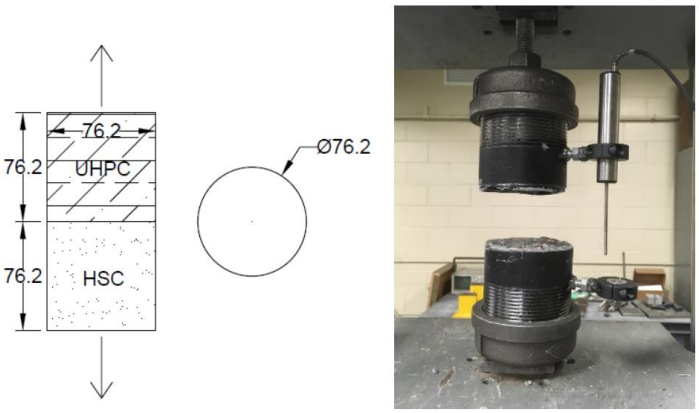

Figure 39: Direct Tension Test Setup *(Tan 2021)*

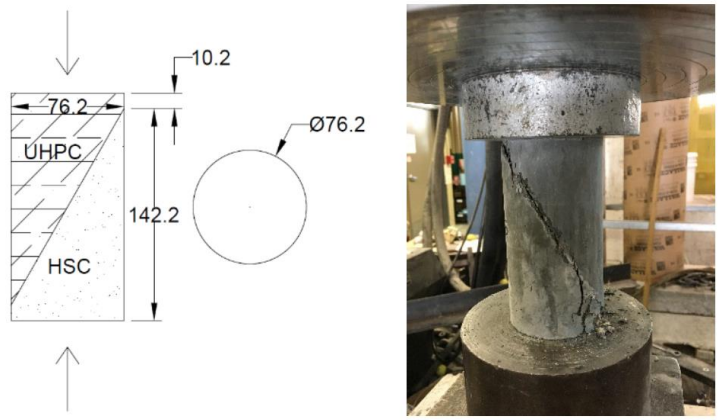

Figure 40: Slant Shear Test Setup *(Tan 2021)*

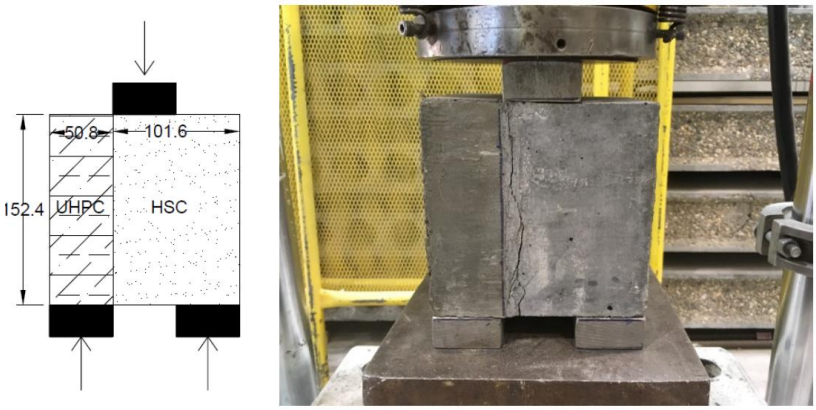

Figure 41: Bi-Shear Test Setup *(Tan 2021)*

3.7.1 Normal Loading to Shear Key Response

The direct tension test, completed in accordance with ASTM C1404/C1404M-98, is used to define the normal stress response across the shear key to girder interface. Figure *42* shows two representative test results of the direct tension test, plotting normal stress and displacement at corresponding increments of loading from the data set. Curve G7-3-7 and Curve G7-3-39 both represents the bond response at 91 days of age. As previously stated in Section 3.6.3 there was an unexplained drop in tensile test at the days 28 and 91 tests, as a result these test results are conservatively used in the development of appropriate model values, with real world higher peak debonding likely present.

From the test results the material stiffness response, denoted by the slope of the dashed red line, can be determined up to the point of damage initiation. For these tests its determined to occur at 0.038 mm of displacement. The corresponding damage initiation stress of 2.78 MPa is found to represent the stress level where debonding begins. This stress is chosen as it is the average max stress between the two representative test results, curve G7-3-7 and G7-3-39, considering the unexplained drop in tension within the direct tension test setup at 28 and 91 days, the model formulation airs on the side of being conservative.

From that point, the specimen rapidly de-bonds which is conservatively estimated to finish at approximately 0.042 mm of displacement. Even though tensile stress continues to build up to a displacement of 0.0485 mm, this lower point of 0.042 mm is chosen for a

few reasons. First the stress level represents the point where displacement starts to rapidly increase, second it is the midpoint between the main damage initiation displacement and the ultimate measured displacement, and third there is minimal additional stress capacity in direct tension beyond this point.

Overall this peak chosen debonding stress in tension is a lower bound value when compared to the direct tension and pull off test results contained in Table *10* and Table *11* respectively.

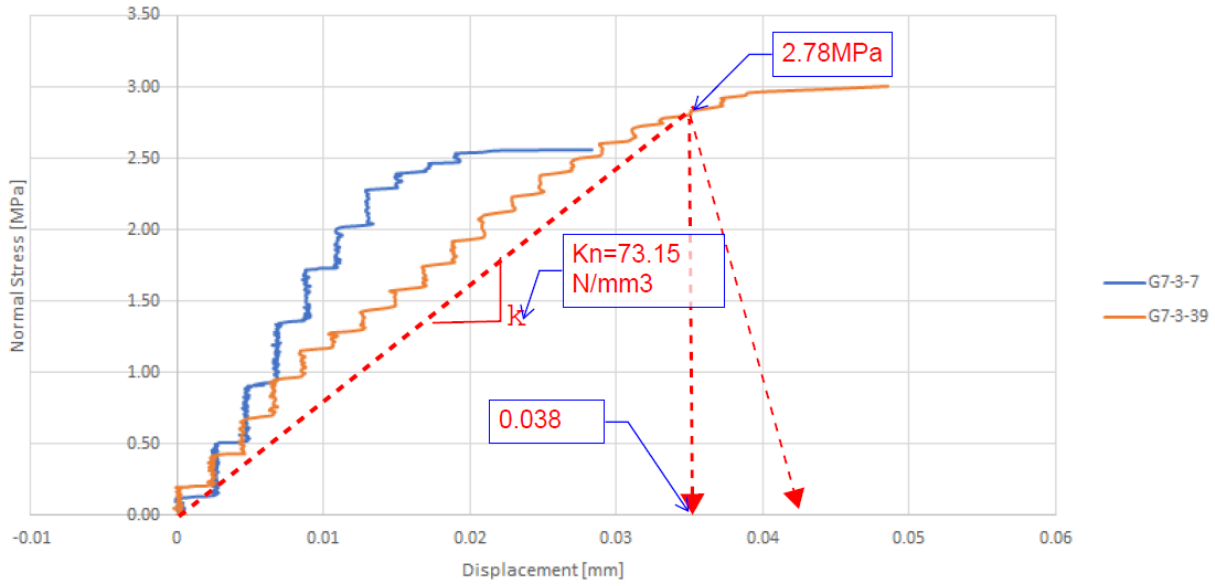

Figure 42: Direct Tension Test Displacement

3.7.2 Vertical Shear Loading Shear Key Response

The slant shear test, completed in accordance with ASTM C882, can be used to represent the response of the girder concrete to UHPC bond to shear force combined with compression. Figure *43* shows two representative test results completed at 91 days of age. From the test results there is a nonlinear portion of the curve up to a

displacement of about 1.2 mm. At 1.2 mm of displacement both curve SS 91-3 and SS 91-4 are relatively linear, so this is taken as the lower bound displacement for linear elastic material stiffness response to start occurring. The determined stiffness response, K_v, attempts to average the slope between the two curves to not overestimate the strain with increased increments of loading within the model.

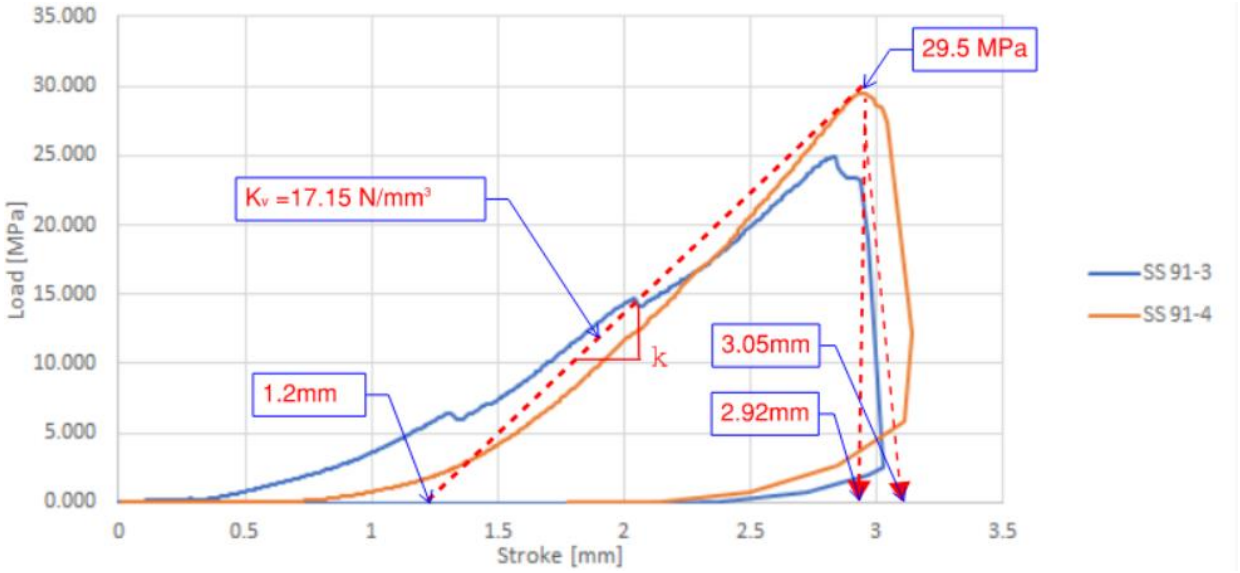

Figure 43: Slant Shear Load Displacement Graph

From the test results the material stiffness response, denoted by the slope of the dashed red line, can be determined up to the point of damage initiation, which occurs at 2.92 mm of displacement. The corresponding damage initiation stress of 29.5 MPa is found to represent the stress level where debonding begins. In relation to the average slant shear test results contained within Table 12, a higher average slant shear failure stress was found at 28 days at 31.4 Mpa compared to 25.9 Mpa at 91 days. In light of this information, the upper bound 29.5 Mpa experienced by curve 91-4 is viewed as more appropriate to represent the damage initiation stress, as the drop between 28 and

91 day averages is unexplained within the testing program. Curve SS 91-4 represents a 91 day test result closer to the strength evolution with time that would be expected to occur.

From that point, the sample rapidly debonded which is demonstrated by damage initiating at 2.92mm of displacement and finishing at 3.05 mm of displacement. The final displacement of 3.05 mm, at which the connection no longer transfers shear stress is chosen as the midpoint between the highest experienced displacement of curve SS91-3 and SS91-4, to add some conservatism to the estimates of debonding within the model in light of the unexplained drop in peak stress.

3.7.3 Horizontal Shear Loading Shear Key Response

The Bi-shear test results can be used to express the response of the girder concrete to UHPC bond to represent the effects of pure shear in the longitudinal direction of the shear key to box girder interface under cold weather where tension is forming in the key. Figure *44* shows two representative test results of the Bi Shear test, chosen conservatively due to stress building up the fastest within these two curves to reach the damage initiation stress level at lower bound displacements. These curves plot the bi shear stress and displacement at corresponding increments of loading. The intention is to provide a conservative indication of debonding and corresponding displacement realizing that variability in test results occurred within the material testing program.

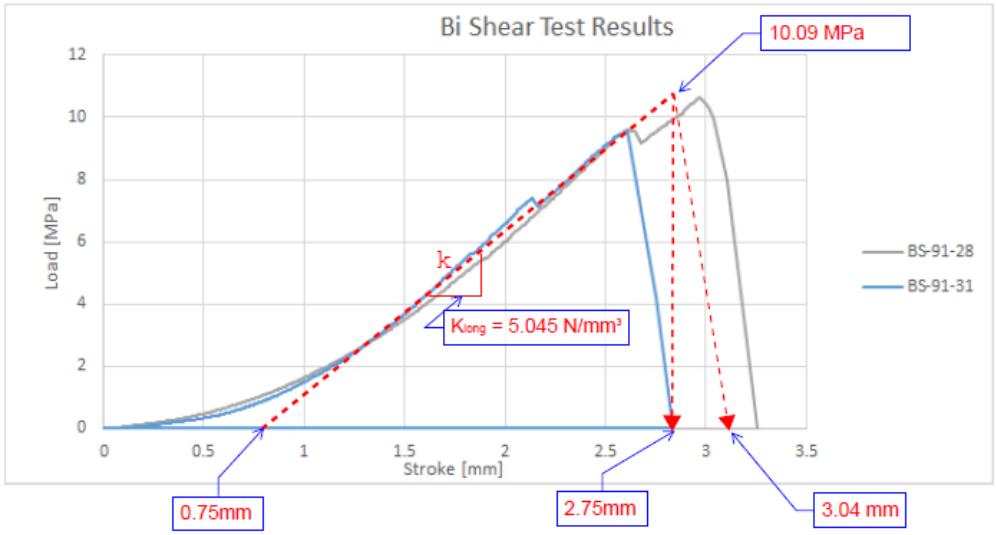

Figure 44: Bi Shear Load Displacement Graph

From the test results the material stiffness response, denoted by the slope of the dashed red line, can be determined up to the point of damage initiation, determined to occur at 2.75 mm of displacement. The corresponding damage initiation stress of 10.09 MPa is found to represent the stress level where debonding begins under horizontal shear.

The stress level is higher than the 91 day average bi shear stress of 6.63 Mpa, however within the underlying data set, provided in Figure *45*, there was a few curves that failed at about half to a quarter of the peak force, and are viewed as anomalies within this model formulation. With that said the peak failure load of four of the six test results at 91 days are all clustered around the peak force, so the chosen upset limit is viewed as reasonable.

From that point, the sample rapidly de-bonds which is demonstrated by damage initiating at 2.75 mm of displacement and finishing at 3.04 mm of displacement. The

complete debonding displacement of 3.04 mm is chosen as the average peak displacement between curves BS 91-28 and BS 91-31 when complete failure and debonding has occurred. This is a consistent choice between all modes of failure. This point attempts to be conservative to not overestimate shear key capacity within the finite element modeling.

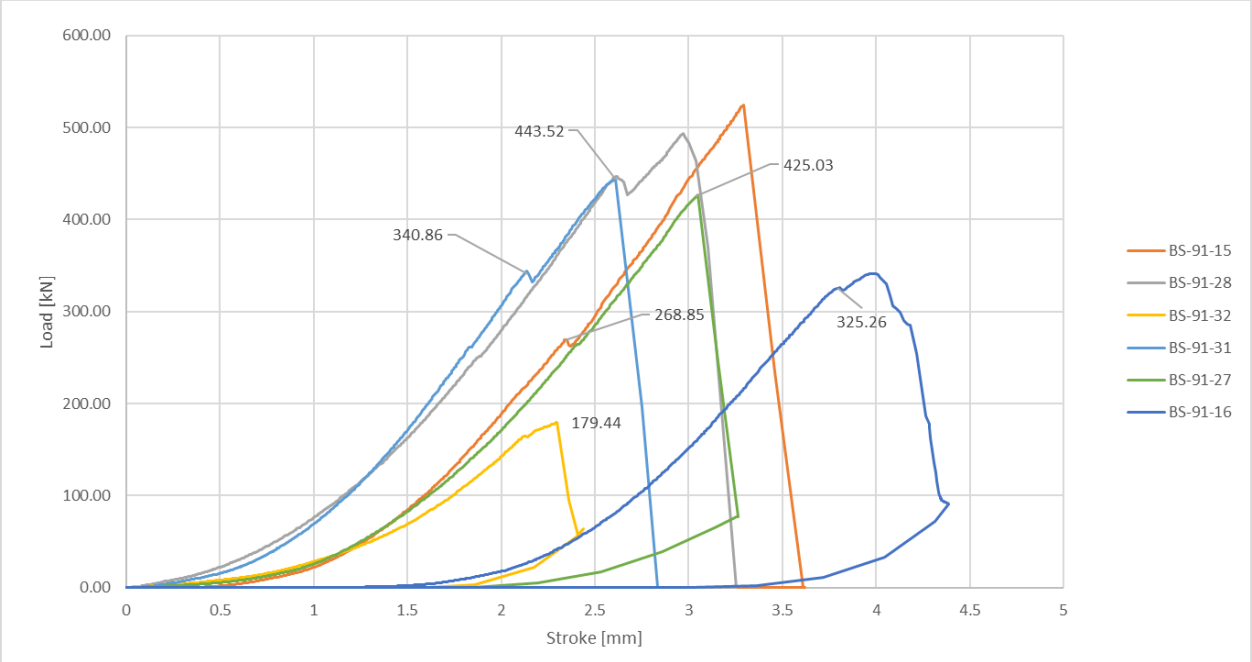

Figure 45: Bi Shear Force Displacement Graphs

3.7.4 Summary of Traction Separation Model Parameters

The results of the traction separation model parameters taken from materials testing are summarized in Table *14* through Table *17*. These parameters are used as shown in the finite element model to represent the shear key response to increase increments of loading and are read off the above graphs.

Table 14: Traction Separation Model - Cohesive Behaviour Parameters

Parameter	Value	Units	Test Source
Normal Direction Stiffness Response, K_{nn}	73.15	N/mm^3	From Direct Tension Test
Vertical Shear Direction Stiffness Response, K_{ss}	17.15	N/mm^3	From Slant Shear Test
Horizontal Shear Direction Stiffness Response, K_{tt}	5.05	N/mm^3	From Bi-Shear Test

Table 15: Traction Separation Model - Damage Initiation Criteria

Parameter	Value	Units	Test Source
Normal Direction Bond Damage Initiation Stress	2.78	MPa	From Direct Tension Test
Vertical Shear Direction Bond Damage Initiation Stress	29.50	MPa	From Slant Shear Test
Horizontal Shear Direction Bond Damage Initiation Stress	10.09	MPa	From Bi-Shear Test

Table 16: Traction Separation Model – Damage Evolution Criteria

Parameter	Effective Displacements		Units
	Initial Start of Damage, δ_{m0}	Final Completion of Damage, δ_{mf}	
Normal Direction - Displacement of shear key through damage evolution, δ_n	0.038	0.042	mm
Vertical Shear Direction - Displacement of shear key through damage evolution, δ_s	2.92	3.05	mm
Longitudinal Shear Direction - Displacement of shear key through damage evolution, δ_t	2.75	3.04	mm
Effective Displacements Through Damage Evolution*, δ_m	4.01	4.31	mm
*Effective Displacement $\delta_m = \sqrt{\langle \delta_n \rangle^2 + \delta_s^2 + \delta_t^2}.$			

Table 17: Traction Separation Model – Mix Mode Ratios

Parameter	Result	unit
Total Plastic Displacement (Difference δ_{mf}-δ_{m0})	0.295	mm
Sum of Total Delta Plastic Displacements	0.424	mm
Mix Mode Ratio 1 (Plastic Normal Displacement / Total Plastic)	0.0094	-
Mix Mode Ratio 2 (Plastic Shear Displacement / Total Plastic)	0.9906	-

3.8 Finite Element Model

The finite element model of adjacent girders has been created within Abaqus CAE. The model has been created using the element dimensions from the tender drawings of the Little Morris River Bridge discussed in Section 3.1 and consists of the concrete geometry of four adjacent girders, intermediate and end diaphragms, end of girder expansion joint block-out beam, internal girder reinforcement including all longitudinal and transverse steel, prestressing steel, shear keys between the girders, and dowels connecting the shear key to girder (including additional lapped bars within the shear key). In addition, elastomeric bearing pads and the translation rods MK GX2 are included within the model.

The model has proceeded utilizing four girders which represent half of the bridge up to the longitudinal centreline. This has been done to provide a robust analysis considering the group effects of the girders, and changes to temperature through the mass of bridge superstructure, while allowing for reasonable (< 1 day) processing times of the finite element model.

3.8.1 Three Model Part Meshing and Interaction

Three-dimensional linear brick elements (C3D8R) were used to model each part. Figure *47* to Figure *48* contains each of the meshed parts. Tie constraints are utilized to connect intermediate, end diaphragms, and end expansion joint block-out beam to the box girder concrete to ensure that no slip and resultant separation is permitted at these interfaces as the girders and diaphragms were cast monolithically and the expansion joint block out is tied to the girders with reinforcement.

Embedded constraints are used to connect all internal reinforcement, shear key dowels, and MK GX2 rods to the girder concrete. Modelling these elements as embedded constraints means that no slip is allowed to occur at their interfaces and that the translational degrees of freedom within the model of the shear key and concrete are constraining the values of the degrees of freedom of the embedded reinforcement/steel. Figure *46* below shows an isometric view of the meshed finite element model as well as the reference coordinate system.

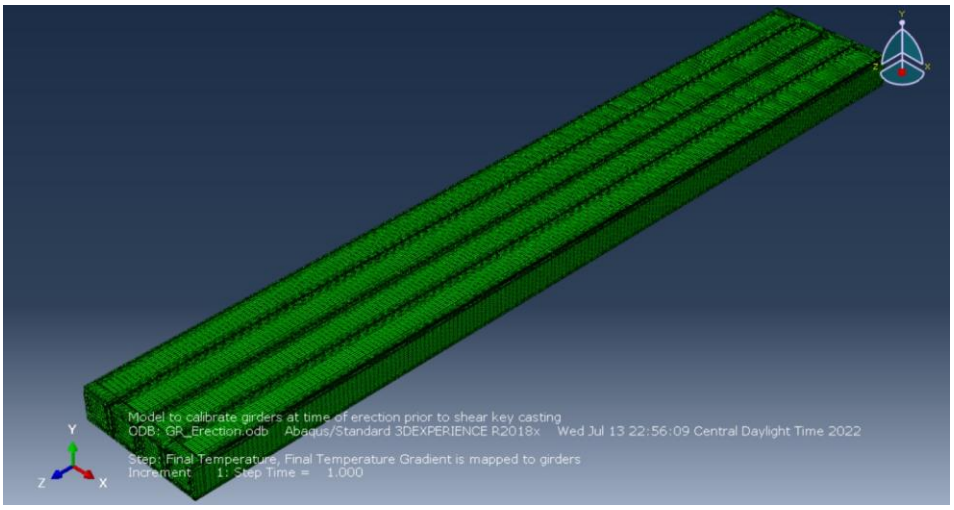

Figure 46: Abaqus CAE Isometric View of Model Meshing

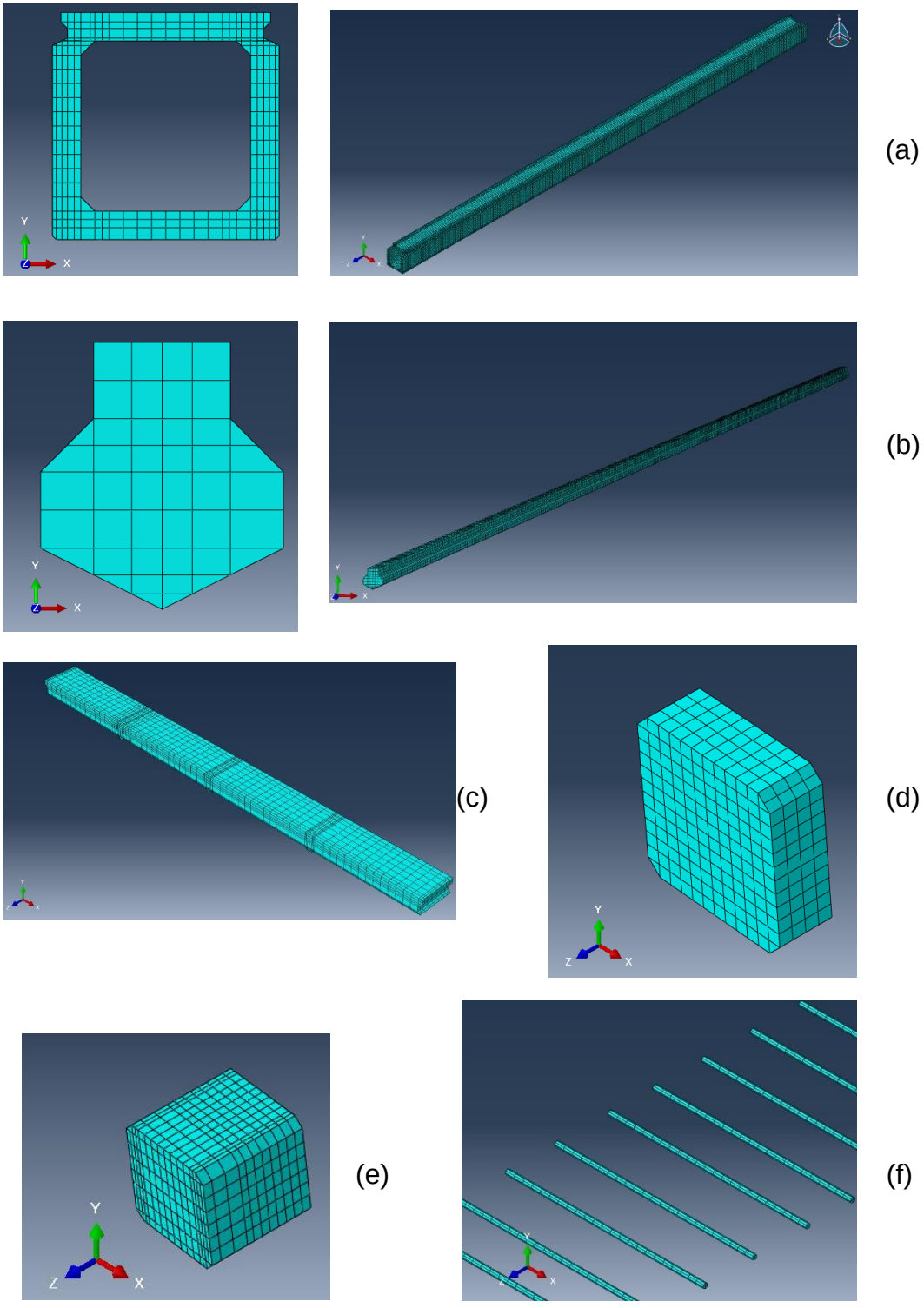

Figure 47: Major Girder Parts (a) Girder, (b) Shear key model parts, (c) Girder end blockout, (d) Intermediate diaphragm, (e) End Diaphragm, (f) Dowels

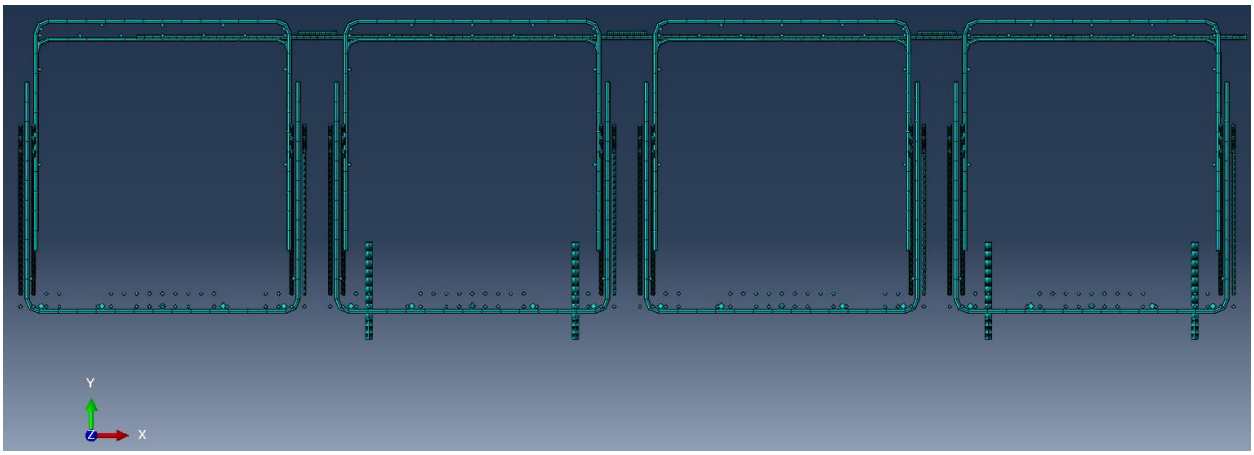

(a)

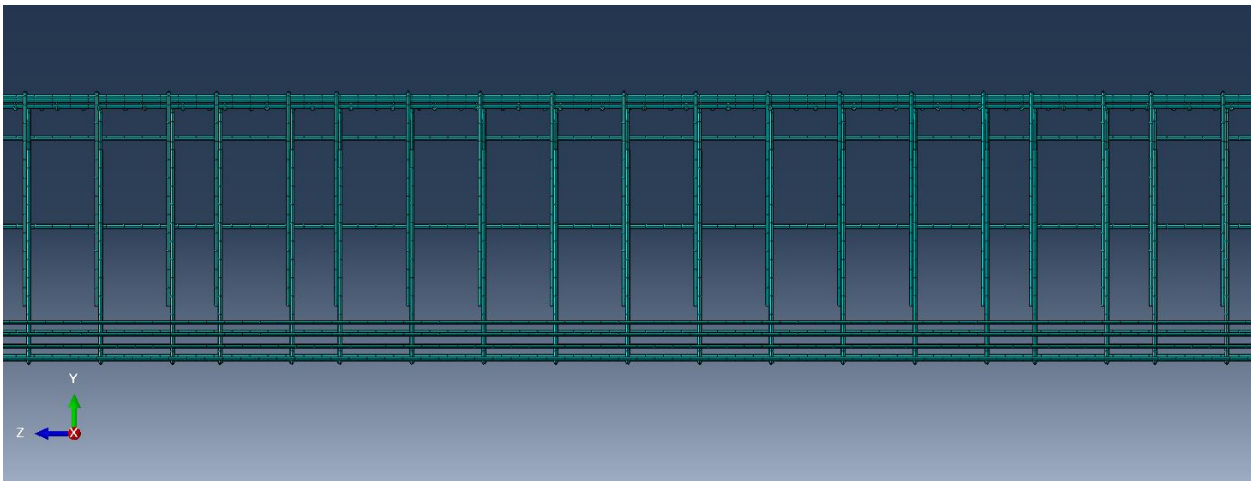

(b)

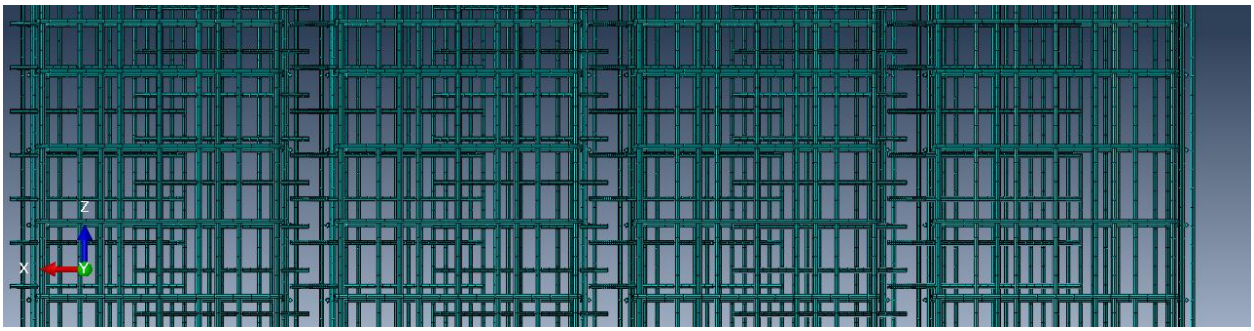

(c)

Figure 48: Assembled Reinforcing Steel (a) Section view, (b) Mid Span Elevation View, (c) Mid span Plan View

Each part within the model has been meshed individually with a seed resolution of at least 75 mm longitudinally in the global Z direction. This is done to obtain more refined results from the model through better representation of interaction between elements degrees of freedom.

Interaction between the UHPC shear key and girder concrete is represented by the traction separation model defined in Section 3.7. Within Abaqus CAE this model represents the interaction using a combination of surface based cohesive behaviour combined with compressive and friction behaviour. The surface based cohesive behaviour is defined by the traction separation model and the calculated input parameters are taken from the materials testing of specimens from the bridge construction.

3.8.2 Final Finite Element Model Material Properties

Material properties from each of the bridge elements are incorporated into the finite element model. Table 18 contains a complete listing of material properties used in the model which were determined as part of the materials testing program described in Section 3.6. The model material properties, shown in the table, have been refined as part of the model calibration process described in Section 4.1, when compared to the results of the materials testing program.

Table 18: Finite Element Model Material Properties

Element	Young's Modulus of Elasticity E (GPa)	Poisson's Ratio
Box Girder	35.0	0.15
Girder End Block out	35.0	0.15
UHPC Shear Key	70.0	0.20
Rebar & Dowels	200.0	0.30
Prestressing Strands	195.0	0.30
Elastomeric Bearings	50.0	0.30

In addition, Table *19* contains a listing of the coefficients of thermal expansion for each material utilized in the finite element model. Further discussion is contained in Section 4.1 as it relates to calibration of the material properties within finite element model. The coefficients for concrete and rebar are in accordance with the AASHTO LRFD Bridge design code, while the UHPC shear key coefficient of thermal expansion comes from the literature where it is recommended that a value of 11 μ/°C should be chosen if no other value can be determined (Graybeal and Russell 2013)

Table 19: Coefficient of Thermal Expansion

Parameter	Coefficient of Thermal Expansion CTE μ /°C
Rebar / Dowels / Strands	11.7
Girder Concrete	10.8
UHPC Shear Key	11.0

3.8.3 Boundary Conditions

As discussed in detail in Section 3.1, the boundary conditions of the Little Morris river bridge consist of a simply supported span with one end free to translate, while the other end is pinned against translation with reinforced elastomeric bearings at either end of the bridge. The pinned end features threaded steel rods between the girder and

concrete pier cap. The finite element model has been developed to represent the fixity arrangement of the in-service bridge.

Within the cold weather finite element model global boundary conditions are represented by elastomeric pads at the ends of the bridge with the underside of the pad fixed to the ground to represent the concrete pier. These pads allow for horizontal Z (longitudinal with bridge centreline) and X (Transverse to bridge centreline) direction movement of the elements constrained by the elasticity and Poisson's ratio material properties applied to the pad. At the fixed end of the span, the pin MK GX2 is included within the finite element model and is modeled as a steel rod with stiffness. The rod is embedded into the girder and has a fixed boundary condition to the ground.

Within the warm weather finite element model global boundary conditions are represented by simply supported pin and roller supports. At the fixed end of the span, the pin MK. GX2 is included within the finite element model and is modeled as a steel rod with stiffness. The rod is embedded into the girder and has a fixed boundary condition to the ground.

Since half of the bridge transverse width is modeled, the centreline of the shear key, located directly at the middle of the bridge, is pinned against transverse movement, and fixed against rotations along its longitudinal axis. This allows the model to rely on the effects of symmetry while reducing computational time. In addition, within both warm and cold weather models, the top flange of the ends of the bridge have been limited to 1 mm of movement in the longitudinal Z direction, determined as part of the model

calibration. Similarly, the free outside edge of the bridge has also been limited to 0.125 mm of movement.

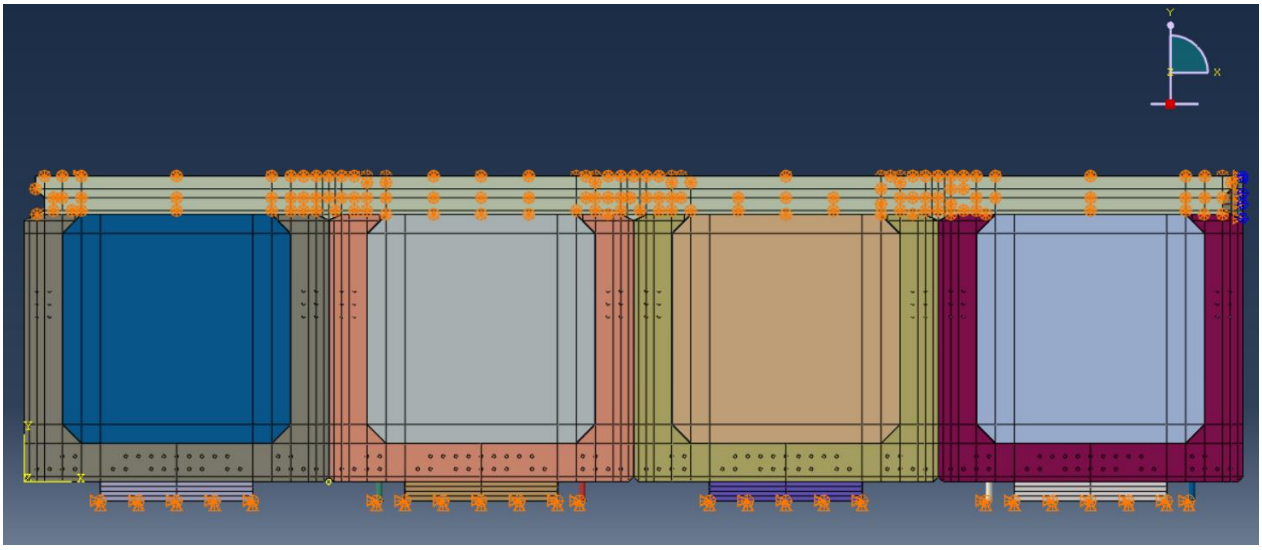

Figure 49: Abaqus CAE End Cross Section View of Girder Model Showing Boundary Conditions

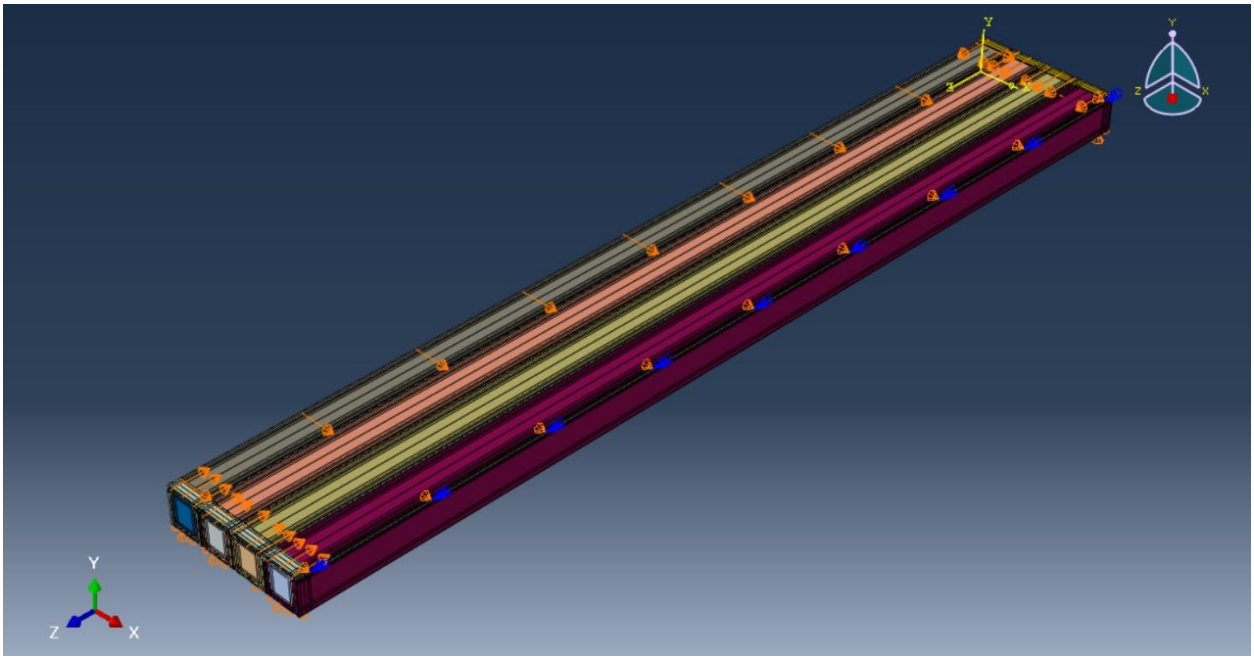

Figure 50: Abaqus CAE Isometric View of Model Showing Boundary Conditions

3.8.4 Load Application

Initial and final temperature gradients, for each of the considered cases, were mapped to the model using a predefined field option. The initial temperature was set in the initial frame at the same time as the self-weight being applied to the model. The final temperature was then mapped to the model and applied in the following time step.

4.0 Finite Element Analysis

This section summarizes the process of finite element model calibration, verification of results from the calibrated finite element model, and the resultant parametric study findings.

4.1 Model Calibration

The Little Morris River bridge contains both thermocouples and strain gauges within the bridge. The goal of the finite element model creation is to replicate the field results through a three-dimensional finite element model. The model formulation has been outlined in Section 3.8 and has been created within Abaqus CAE.

From the measured field data, snapshot temperature profiles have been chosen, outlined in Section 3.5 to represent both cold weather and warm weather temperature gradients applied to the bridge. The finite element model is first run using the fixity conditions and material properties from the drawings and available data. From there, refinements were added and material properties modified as outlined in the following sections.

4.1.1 Top Flange Movement Restraint

Early in model calibration it was determined that the magnitude of top flange strains in the transverse X (EE11) and longitudinal Z (EE33) directions of loading were low in magnitude at mid span and at the support for both the cold weather and warm weather cases. At the time, a trial and error of restraint conditions in these directions was

conducted to determine the point at which the magnitude of strain would be within the field data level of magnitude.

The trial-and-error evaluation found that initially without restraint top flange results magnitudes of strain were about one tenth to one quarter of the required strain in the transverse and longitudinal direction. The restraint brought values into the correct magnitude as was measured within the field. With the restraint an upset limit of influence of around 1mm was found. Additional restraint beyond these values had minimal effect on girder strains.

The final top flange restraint chosen by this analysis found that a top flange restriction to 1 mm of movement in the longitudinal Z direction (EE33) produced a level of strain expected in the field. Similarly, a maximum movement in the transverse X direction (EE11) found that a top flange movement restriction of 1.125 mm produced the level of magnitude of strain within the measured field data. This trial-and-error process utilized the average material properties for girder and shear keys established in sections 3.6.1 and 3.6.2 within the model.

4.1.2 Material Property Sensitivity Analysis

Following establishment of the fixity conditions, a sensitivity analysis of the UHPC and girder concrete elasticity as well as poisson's ratio was completed to establish the general trends the model outputs and refine the model to better match the field data. The analysis results are shown in Table *20*. This material sensitivity analysis was completed considering a tie constraint between the girder and shear key, in place of the traction separation model, under the cold weather case of January 16, 2020. This was

done to determine the influence and appropriate material properties prior to moving to the higher level of refinement offered by the traction separation model.

As a result of the traction separation model not being used in this analysis, all reported strain values are higher than final results using the traction separation model. This sensitivity analysis results are meant to demonstrate the trends that occurred in the analysis for each considered material property and form part of the calibration.

Table 20: Finite Element Model Material Property Sensitivity Analysis

Girder Property		UHPC Shear Key Property		Modeled – Mid Span SK1		Field – Mid Span SK1	
Poisson Ratio	Modulus of Elasticity (GPa)	Poisson Ratio Tested	Modulus of Elasticity Tested (GPa)	EE11 – Transverse Shear Key Strain (με)	EE33 Longitudinal Shear Key Strain (με)	EE11 – Transverse Shear Key Strain (με)	EE33 Longitudinal Shear Key Strain (με)
0.26	40	0.1	60	172	248	52	63
		0.18	60	156	249	52	63
		0.3	60	130	251	52	63
0.15	40	0.2	60	145	250	52	63
0.10	40	0.2	50	167	250	52	63
		0.2	60	138	250	52	63
		0.2	70	113	249	52	63
0.10	35	0.2	70	98	251	52	63

From this sensitivity analysis the final model material properties have been determined for use. The modulus of elasticity of the concrete girder has been taken as 35GPa. This modulus is a lower bound of the materials testing completed on samples from the structure, outlined in Section 3.6.1, however variability does exist between laboratory testing of a discrete sample and the in-situ structure. In addition, the Poisson's ratio has been taken as 0.15. The sensitivity testing noted improved results with a ratio of 0.1 for the concrete girder, improving strains towards field result by about 7 με in tension within

the cold weather sensitivity analysis, however, as outline in Section 3.6.1 more comprehensive justification exists within the literature for long term Poisson's ratios in concrete between 0.15 – 0.2 (CSA 2019).

The modulus of elasticity of the UHPC has been taken as 70 GPa within the finite element model with a Poisson's ratio of 0.2. Under cold weather application sensitivity analysis the higher modulus of elasticity produced the best results in the calibration and can be justified by the continued increase of modulus with time, demonstrated by the regression analysis in Section 3.6.2, which places the modulus somewhere between 61 364 – 68 068 MPa at six months of age and 66 602 – 76 703 MPa at 18 months of age. Sensitivity testing of the UHPC modulus of elasticity between 50 GPa and 70 GPa within the finite element model reduced the results in tension by 54 με bringing the analysis more in line with field results. The Poisson's ratio is widely cited in the literature as 0.2 for UHPC (Graybeal and Russell 2013).

Overall, the final material properties have been judged to be reasonable with respect to the materials testing program and values available within the literature. The final material properties used in finite element modeling are provided in Section 3.8.2 within Table *18* and Table *19*. From this sensitivity analysis a few trends can be noted worth pointing out including:

- As the Shear key modulus of elasticity increases, the tensile strain within the shear key decreases;

- As the difference in modulus of elasticity between the shear key and girder increases, the magnitude of tensile strain within the shear key also trends downward; and
- The Poisson's ratio of both the shear key and girder has an influence on the magnitude of shear key strain. While less pronounced than the influence of the magnitude of elasticity of each component, it still influences the level of strain.

4.1.3 Results of Calibrated Validation Model Analysis Cases

As this is a study of shear key behaviour under cold weather gradient effects, validation of the model under cold weather conditions is of key importance. Two cold weather cases, January 16, 2020, and February 14, 2021 are utilized to validate the behaviour under cold weather conditions. The model is then tested against a warm weather scenario on July 3, 2020 to provide a broader validation of model behaviour. The three cases are described in detail within Section 3.5 with an initial reference temperature from Nov 26, 2019 being applied as the initial temperature of the model in all cases. The January 16, 2020 case represents a differential cold weather application between the exterior edge of the bridge and its core, while the February 14, 2021 case represents coldest recorded temperature within the recorded data throughout the mass of the structure.

Table *21* through Table *23* provide the comparison of measured field strain data to the results obtained from the finite element model utilizing the developed traction separation model to represent shear key bond behaviour at the shear key interface to girders within the structure. First, examining the strains across the shear key at mid span, in Table *21*,

we can see that the model is replicating the behaviour and level of magnitude of transverse strain quite closely to the measured field data. The distribution follows what one might expect as the temperature changes. As it gets colder, between the January 16, 2020 and Feb 14, 2021 cases, the level of tension strain across the shear key increases. Once the warm weather gradient, of July 3, 2020 is checked the behaviour of the model turns to compression.

Table 21: Mid Span Shear Key Strains Validation Cases

Date	Result	EE11 Transverse Strains (με)			EE33 Longitudinal Strains (με)		
		SK 1	SK 2	SK 3	SK 1	SK 2	SK 3
January 16, 2020	Field	52	-	60	63	80	-
	FE Model	67	67	67	243	249	243
February 14, 2021	Field	75	-	70	103	84	-
	FE Model	79	80	80	299	302	300
July 3, 2020	Field	-115	-	-98	-121	-131	-
	FE Model	-146	-147	-146	-203	-207	-194
Note: FE model shear key measurements taken 58.75 mm below the top of shear key to correspond with approximate final placement of gauge within the shear key.							

Table 22: Support Shear Key Strains Validation Cases

Date	Result	EE11 Transverse Strains (με)			EE33 Longitudinal Strains (με)		
		SK 1	SK 2	SK 3	SK 1	SK 2	SK 3
January 16, 2020	Field	46	51	49	-	-	-
	FE Model	97	86	66	199	208	206
Feb 14, 2021	Field	70	69	75	-	-	-
	FE Model	115	92	70	240	249	245
July 3, 2020	Field	-91	-101	-88	-	-	-
	FE Model	-223	-227	-197	-164	-139	-139
Note: FE model shear key measurements taken 58.75 mm below the top of shear key to correspond with approximate final placement of gauge within the shear key.							

The longitudinal strain within the shear key is being modeled higher in magnitude in all cases, however the direction of strain (expansion / contraction) is correct to the field data. One potential cause of this difference is the lack of long-term shrinkage strains being considered within the finite element model. A review of the literature indicates that shrinkage strain in UHPC between 28 days and ultimate strain can be sizable, with ultimate long term shrinkage values ranging between 555 and 766 με being reported dependent on curing conditions (Flietstra 2011). Typical 28-day shrinkage has been reported around 550 – 600 με depending on the curing regime (Weldon, et al. 2019), demonstrating that there is potential for long term shrinkage between the reference strains, on Nov 26, 2019, and each of the validation cases.

Overall, the behaviour of the bridge is captured better at mid span compared to at the support. This could be related to the boundary conditions utilized within the model to achieve the calibration. However, the level of magnitude and direction of strain at the support is still being replicated by the finite element model.

The transverse and longitudinal girder strains are provided in Table *23* at mid span of the girder. The top flange transverse strains within the girder are replicating both magnitude and direction under the cold weather cases. The warm weather case is replicating the correct direction, however the magnitude of strain in compression is high. The longitudinal strains within the girders are correct in direction and magnitude for the bottom and top flanges under the January 16 case. However, the February 14, 2021 case the magnitudes are too high within the finite element model compared to field readings.

Digging a little deeper into the comparison of cold weather cases it can be noted that the longitudinal strain field readings substantially decreased between Jan 16, 2020, and February 14, 2021, but the weather profile got colder on Feb 14,2021. From previous discussion, additional tensile strain in the girder would be expected as the girder gets colder, not less. The finite element model output additional tensile strain as would be expected.

A likely cause of the lower tensile strains within the field data is the girder cracking over the year between results. Cracked girder stiffness would cause lower tensile strains measured in the field and is not captured within the finite element model as linear elastic analysis is used within this study. Examining the tensile capacity relationship in the CSA S6-19 bridge code, Clause 8.4.1.8.1 the tensile capacity of concrete is taken as 0.4 times the square root of the concrete compressive strength (CSA 2019).

This tensile capacity relationship would result in a tensile capacity of 3.35 MPa for the girders (conservatively taken as 70MPa compressive strength). In turn, the expected cracking strain would be in the region of 96 με, indicating a high likelihood of cracking occurring within the girders. The girder would experience a reduced effective inertia under increased increments of loading the structure experiences which is not taken into account within this study and may account for some of the difference between modeled and field strain results. This would also influence the longitudinal strains within the shear key, due to the supporting beams reduced stiffness.

Bottom flange transverse tensile strains are not reported as the prestressing force has not been applied to the finite element model here. The longitudinal prestressing would have a substantial impact on the transverse strains through the Poisson effect, however accurate modeling of this effect is a limitation of the finite element model.

In addition, it is documented in the literature that bearing stiffness changes with temperature variation, with elastomer stiffness increasing with reduced temperature. This could be a key source of the difference between the predicted cold weather and warm weather strains (AASHTO 2020). As a result the support boundary conditions were modified between the cold and warm weather cases as outline in Section 3.8.3.

Table 23: Mid Span Girder Strains Validation Cases

Date	Result	EE11 Transverse Top Flange Strains (με)				EE33 Longitudinal Top Flange Strains (με)				EE33 Longitudinal Bottom Flange Strains (με)			
		G1	G2	G3	G4	G1	G2	G3	G4	G1	G2	G3	G4
January 16, 2020	Field	207	239	258	221	83	284	265	258	223	213	200	180
	FE Model	231	231	232	230	240	244	240	243	230	213	211	212
Feb 14, 2021	Field	291	326	289	267	151	120	131	99	61	64	61	40
	FE Model	261	254	254	252	289	284	282	285	240	240	239	240
July 3, 2020	Field	-138	-146	-157	-113	-134	-254	-243	-266	-204	-211	-220	-183
	FE Model	-370	-392	-372	-375	-192	-189	-178	-178	-296	-254	-249	-247

As this is a study of the bond behaviour of the shear keys under cold weather conditions in the transverse direction, the overall model behaviour is seen as acceptable. The model overpredicts the tension in the shear key and under predicts the tension within the girder flange. This will provide a conservative indication of debonding temperature and stress under parametric testing. Of key importance is the model's ability to recreate

the large difference in tensile strain across the shear key to girder bond experienced by the structure. This allows for the modeling of the primary damage mechanism, debonding under increased increments of cold weather.

In addition, a key feature of the field data is the fact that following the likely cracking that occurred between the January 16, 2020 and February 14th, 2021 case, the strain distribution between shear key and girder are similar. This indicates that shear stresses are not really building in the longitudinal direction of the shear key and are not contributing to stress that would lead to debonding. As a result, longitudinal strains are not a large influence on the outcomes of this study and do not play a key role in debonding of the shear key under increasing increments of extreme cold. This field behaviour is replicated by the model. The following Figure *51* through Figure *60* provide snapshots of the strain distribution within the model for the extreme cold weather cases that provide some key context when interpreting the results provided in the tables.

Figure *51* and Figure *52* show the longitudinal and transverse strain distribution within the bridge girders for the February 14, 2021 temperature profile application. This was the coldest on record temperature event where the bridge was also a similar temperature throughout its depth and width. This is reflected within the strain profile results which show a linear decrease in longitudinal tension between the top and bottom flanges of the girder that is consistent across the width of the bridge indicating some rotation of the cross section is occurring, from the thermal moment being induced. Top flange transverse tension is also consistent across the width of the structure, with tension concentrating in the centre of the girder flange and reducing at shear key locations.

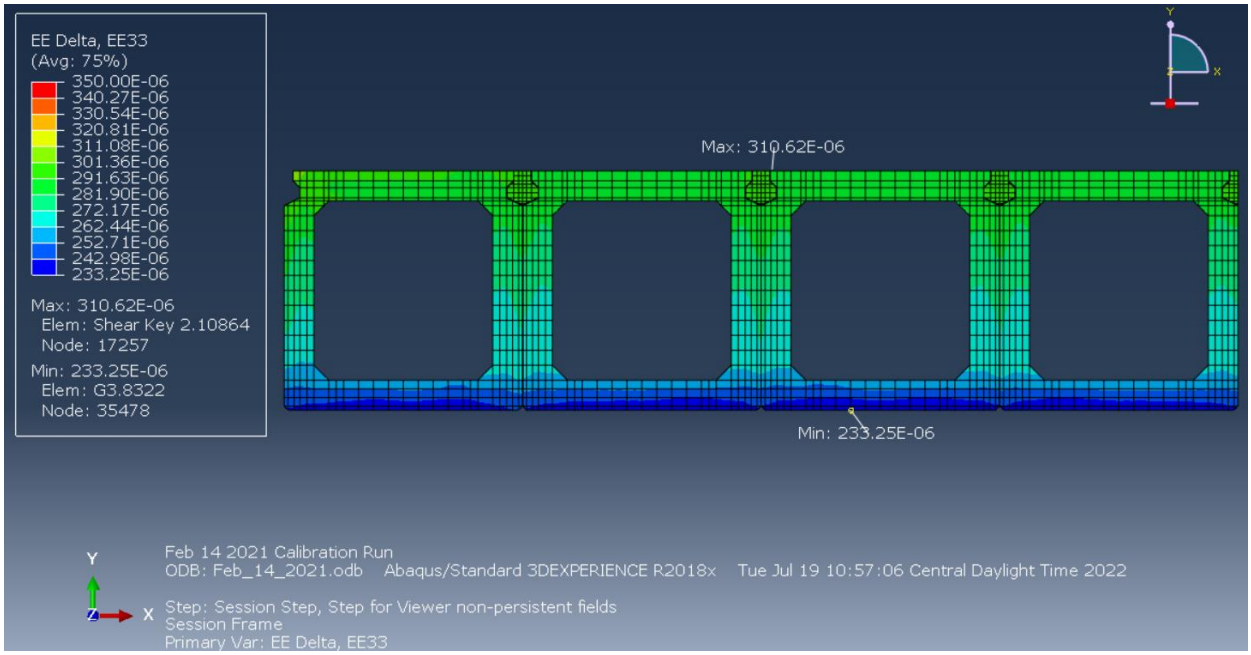

Figure 51: Mid Span Longitudinal Strain (EE33) – Feb 14, 2021

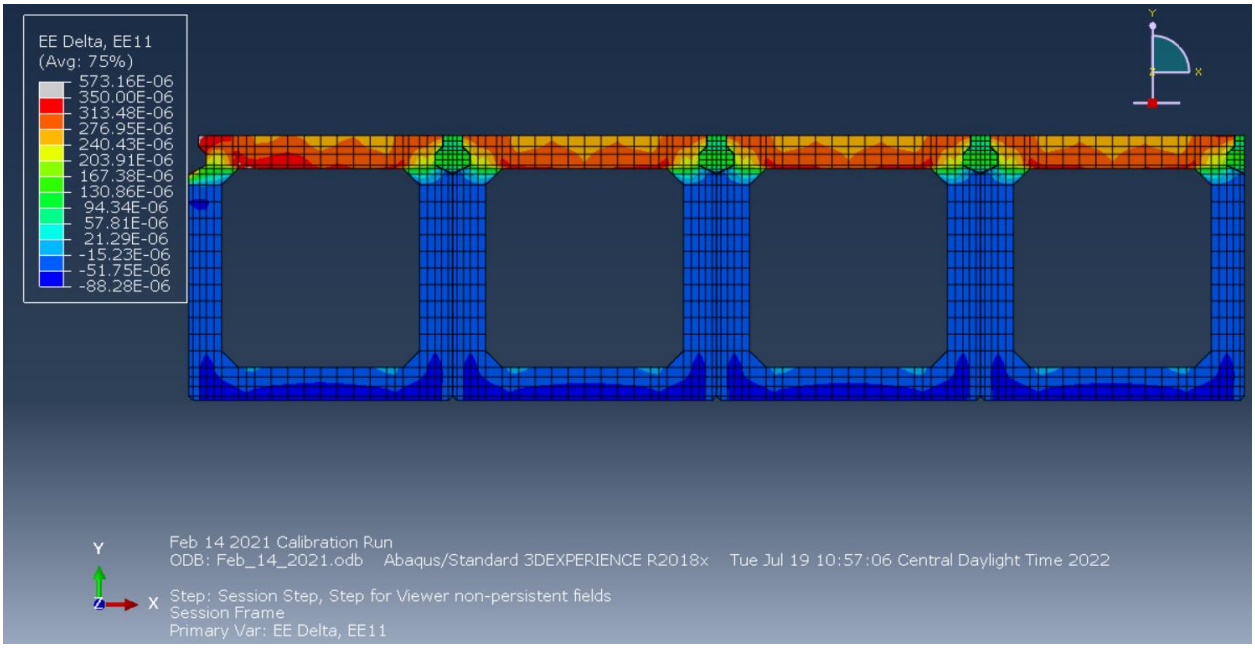

Figure 52: Mid Span Transverse Strain (EE11) – Feb 14, 2021

Figure *53* and Figure *54* provide the transverse (E11) and longitudinal (E33) strain distribution throughout shear key 1, the west most key, and shear key 2 adjacent. From these results it is demonstrated that the highest tensile transverse strain in the key is experienced at the level of the steel dowels. The strain reduces above and below these locations with the sloped face of the shear key experiencing the lowest transverse strain in the key. The strain distribution was found to be similar between shear key 1 and shear key 2.

Figure *55* shows the transverse distribution across the shear key into the dowels. The modeling demonstrated that the highest strain is experienced at the interface between the dowel and UHPC. This finding is in line with the past work of (Semendary, Steinberg, et al. 2019)

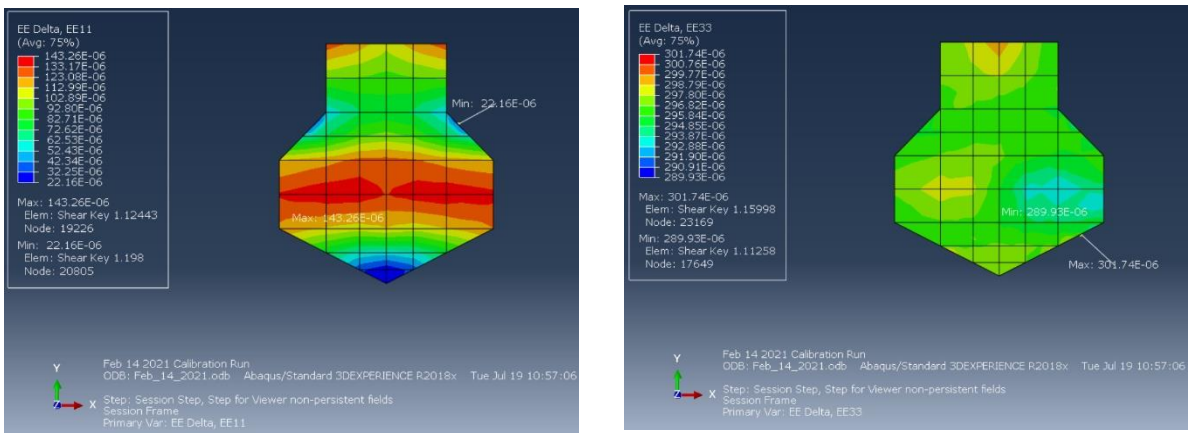

(a) (b)

Figure 53: SK1 Mid Span Strains (a) EE11, (b) EE33 – Feb 14, 2021

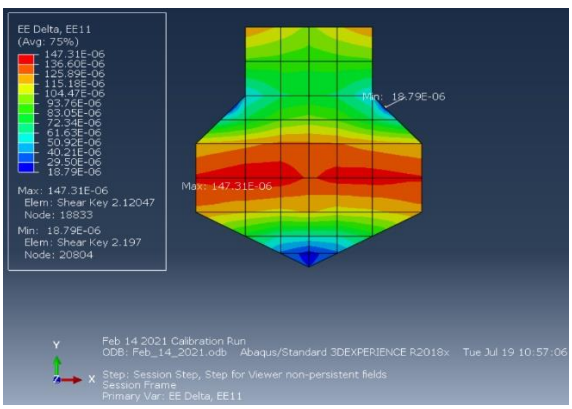

(a)

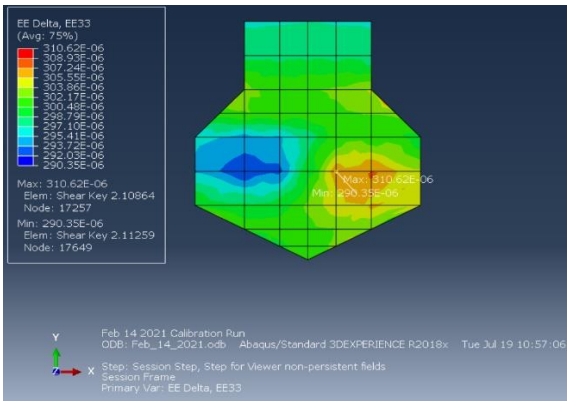

(b)

Figure 54: SK2 Mid Span Strains (a) EE11, (b) EE33 – Feb 14, 2021

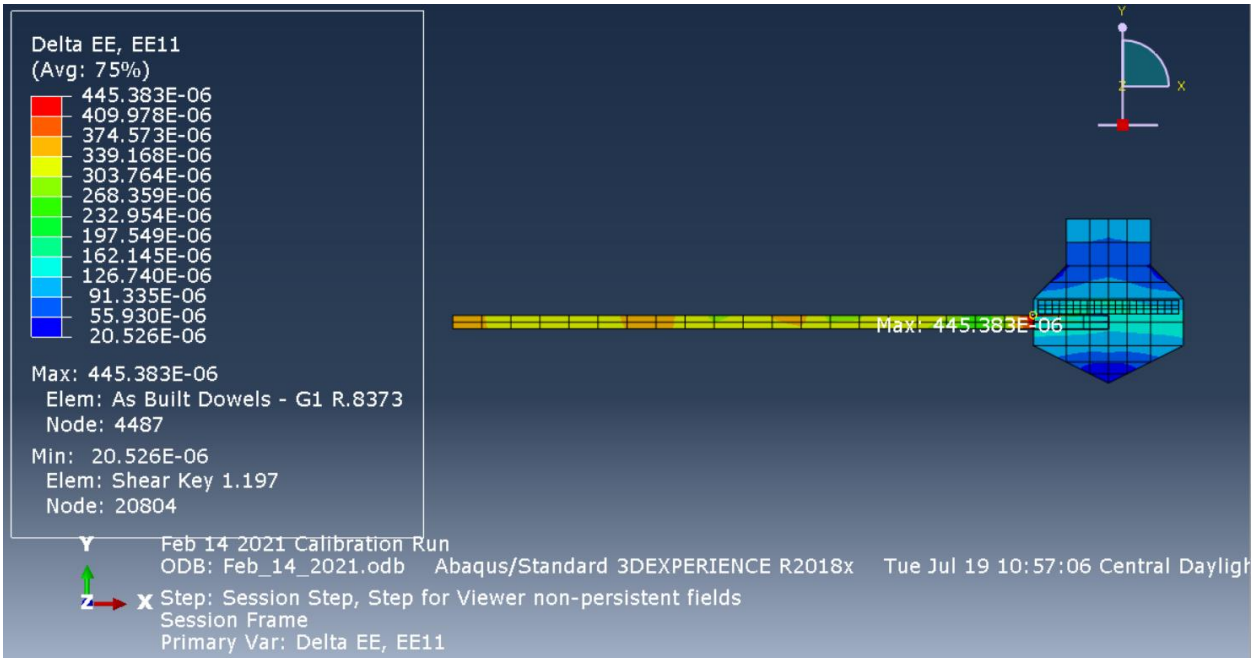

Figure 55: SK1 Mid Span Strains at SK to Dowel Interface – Feb 14, 2021

Figure *56* and Figure *57* show the longitudinal and transverse strain distribution within the bridge girders for the January 16, 2020 temperature profile application. This temperature profile featured a colder west face of the bridge (beam 1) and temperature warming up within the centre mass of the box girders. This is reflected within the strain

profile results which show a higher tension strain within the west exterior face and decreases towards the centre of the structure. In addition, there is a decrease in tension between the top and bottom flanges indicating some rotation of the cross section is occurring, from the thermal moment being induced. Top flange transverse tension reduces across the width of the structure with more tension experienced within the west most girder and deceasing across the bridge width. Similar to the February 14, 2021 case tension is concentrating in the centre of the girder flange and reducing at shear key locations.

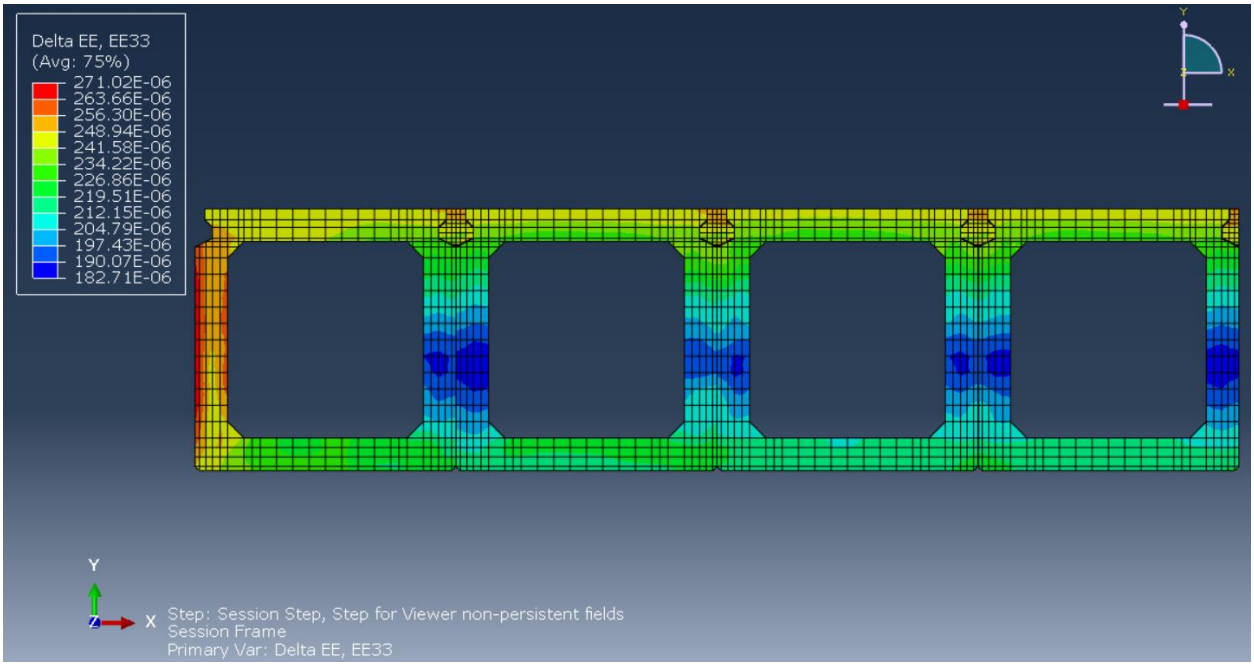

Figure 56: Mid Span Longitudinal Strain (EE33) – Jan 16, 2020

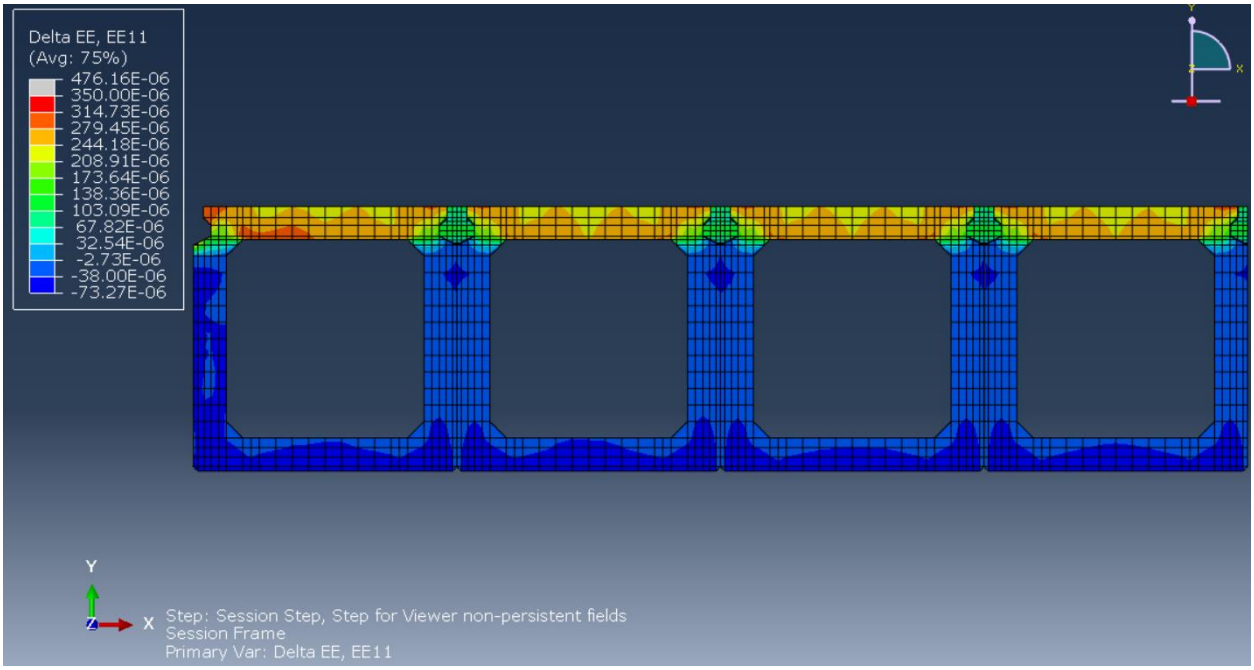

Figure 57: Mid Span Transverse Strain (EE11) – Jan 16, 2020

Figure *58* and Figure *59* provide the transverse (E11) and longitudinal (E33) strain distribution throughout shear key 1, the west most key, and shear key 2 adjacent. From these results, similar to the Feb 14, 2021 case, it is demonstrated that the highest tensile transverse strain in the key is experienced at the level of the steel dowels. The strain reduces above and below these locations in the sloped face of the shear key with the lowest transverse strain in the key found within the sloped faces. The strain also reduces towards the centre of the shear key. The strain distribution was found to be similar between shear key 1 and shear key 2.

Figure *60* shows the transverse distribution across the shear key into the dowel. The modeling demonstrated that the highest strain is experienced within the girder due to the pulling action created by the west exterior face being colder than the rest of the bridge. A similar magnitude of strain was experienced at the girder to UHPC interface.

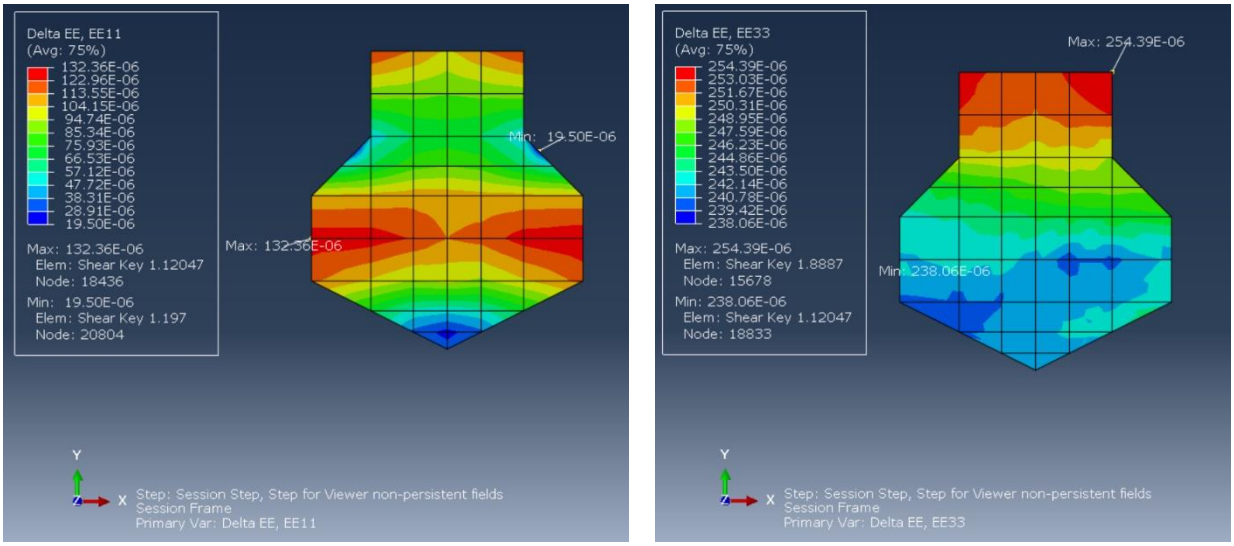

(a) (b)

Figure 58: SK1 Mid Span Strains (a) EE11, (b) EE33 – Jan 16, 2020

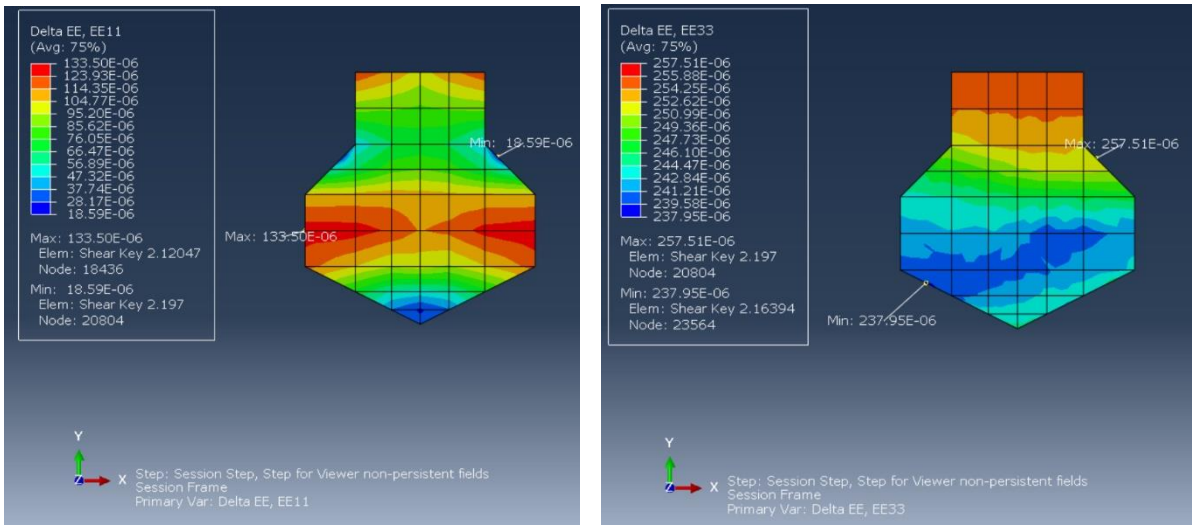

(a) (b)

Figure 59: SK2 Mid Span Strains (a) EE11, (b) EE33 – Jan 16, 2021

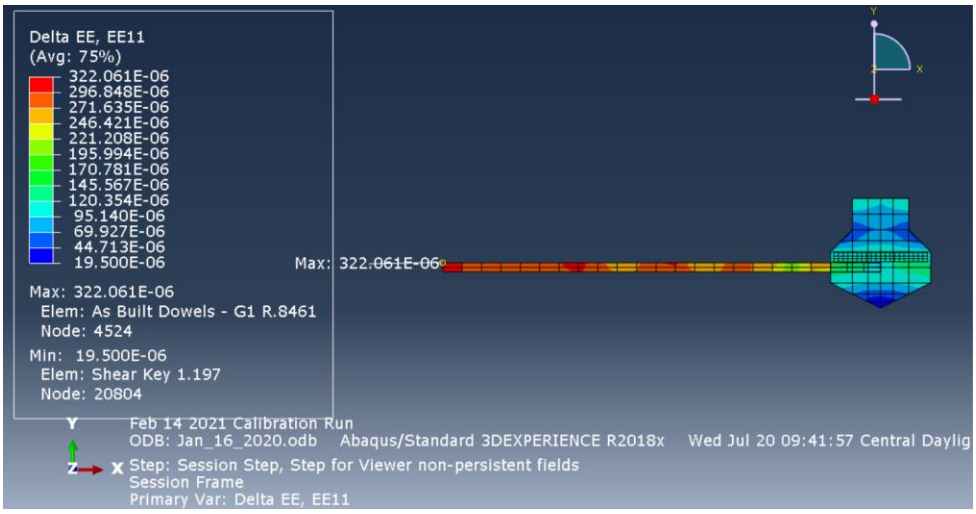

Figure 60: SK1 Mid Span Strains at SK to Dowel Interface – Jan 16, 2020

Finally examining the mid span and end of bridge dowel strains provides some commentary as it relates to model behavior. Table *24* provides the field measured and finite element modeled axial dowel strains at mid span and over the support for the two cold weather validation cases where tension forms in the dowels. Figure *61* provides the schematic location where results are provided. The strains in the other shear keys are consistent with these representative dowel strain values and can be seen in Section 3.5.2.

Table 24: Mid Span Dowel Strains Under Cold Weather Validation Cases

Date	Result	Dowel Axial Strains EE11 (με)	
		Shear Key 1 Mid Span Dowels	Shear Key 1 End of Bridge
January 16, 2020	Field	19 Left Dowel 20 Right Dowel	8 Left Dowel -2 Right Dowel
	FE Model	26	572
Feb 14, 2020	Field	32 Left Dowel 38 Right Dowel	28 Left Dowel 8 Right Dowel
	FE Model	40	794
Note: Left and Right dowels had the same value within finite element model.			

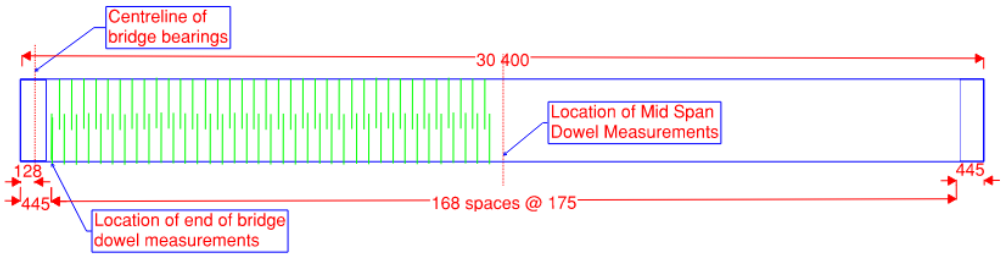

Figure 61: Girder Plan View Schematic Location of Dowel Measurements and Results

Figure *62* and Figure 63 provide a snapshot of the finite element dowel strains for the two corresponding cold weather cases within shear key 1. The dowel strains within the shear key at mid span are reporting similar values to field measurements with 26 με and 40 με being reported for the January 16, 2020, and February 14, 2021 cases respectively. From the figures these low values are reported at the centre of the shear key and the finite element model rapidly increases the magnitude of strain within the dowel as it exits the shear key.

In reality, the zone of development of the dowel bar would be larger than what is indicated within the finite element model as the local interface bond condition to the bar is not being modeled here. This may partially explain why the field sensors are picking up lower strains at measured dowel locations, and the finite element model is reporting much higher strains at that same interface. Additionally, the sensors may not have been placed in the critical location on the dowel, resulting in them not picking up the peak strains.

In addition, the model indicates high tensile strain in the dowel directly over the bridge support. This is consistent with past modeling by Semendary et al. (Semendary, Steinberg, et al. 2019) and appears to be a limitation of the finite element model, as the reported field data strains in dowels over the supports are consistent with the mid span

strains. One potential reason for the higher dowel strains over the supports relates to the boundary conditions used within model calibration, namely the use of top flange movement restraint. This restraint may be causing a buildup of stress at the bridge ends subsequently being transferred into the dowels. Another potential reason is related to the stiffness at the end of the girder increasing due to the end diaphragm. This increased stiffness may be articulating more stress to the bridge end where the end dowels are located as a result.

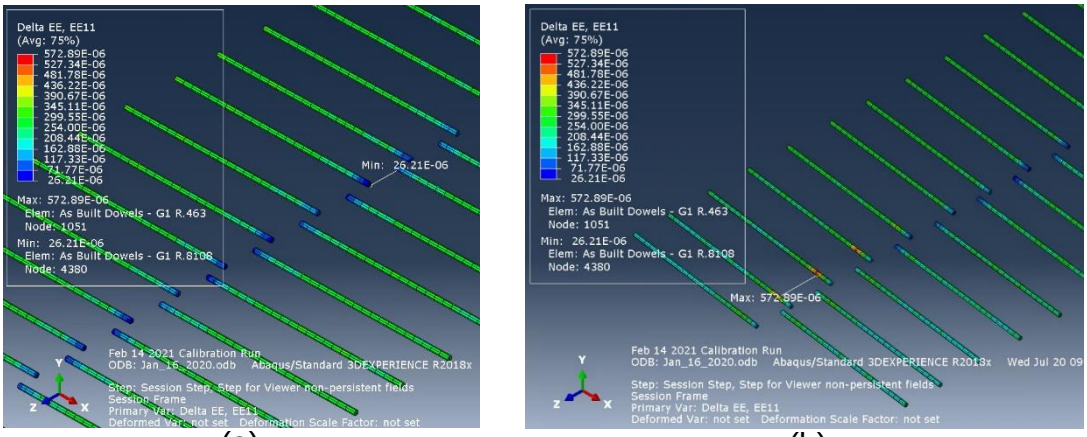

(a) (b)

Figure 62: SK1 Dowel Strains EE11 (a) Mid Span (b) Support – Jan 16, 2020

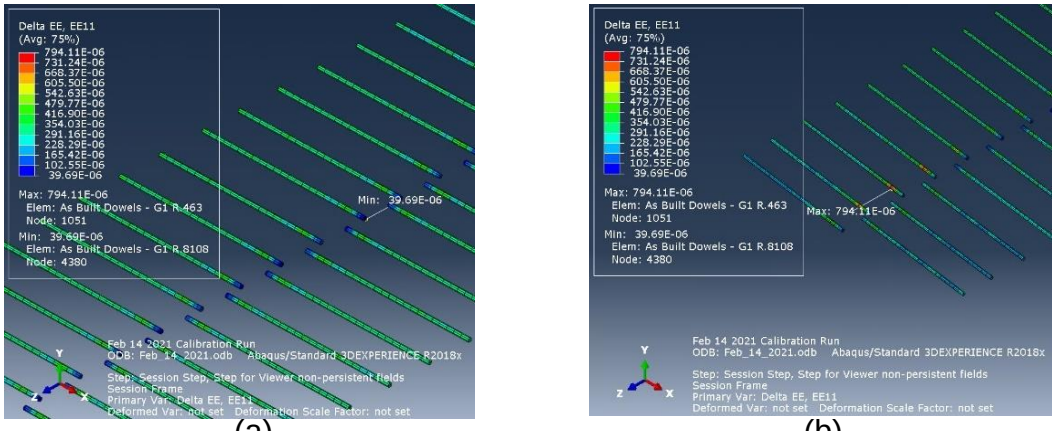

(a) (b)

Figure 63: SK1 Dowel Strains EE11 (a) Mid Span (b) Support – Feb 14, 2021

4.2 Parametric Testing

Three cold weather temperature gradients have been chosen for investigation of shear key behaviour under increasing increments of extreme cold conditions. These temperature gradients, shown in Table *25*, represent a consistent distribution of cold temperature throughout the thermal mass of the structure. Each of the tested gradients decrease the coldest on record temperature distribution from February 14th, 2021 by a progressive 5 degrees Celsius. For each case, the shear key strain, girder strain, mid span dowel strain, and damage index (DI) have been determined.

Table 25: Parametric Cold Weather Testing Cases

Depth (mm)	Girder-1				Girder-4			
	Field Temp. Feb.14th (^{0}C)	Gradient (^{0}C)			Field Temp. Feb.14th (^{0}C)	Gradient (^{0}C)		
		1	2	3		1	2	3
1200 (Top)	-27.55	-32.55	-37.55	-42.55	-25.08	-30.08	-35.08	-40.08
1100	-27.15	-32.15	-37.15	-42.15	-25.63	-30.63	-35.63	-40.63
796	-25.67	-30.67	-35.67	-40.67	-24.985	-29.985	-34.985	-39.985
498	-25.35	-30.35	-35.35	-40.35	-24.34	-29.34	-34.34	-39.34
200	-24.54	-29.54	-34.54	-39.54	-24.51	-29.51	-34.51	-39.51
0	-22.85	-27.85	-32.85	-37.85	-22.93	-27.93	-32.93	-37.93

Table *26* and Table *27* provide the results of shear key transverse and longitudinal strain under each of the tested cases. From the EE11 transverse results, it can be shown that the tensile strain across the key at mid span increases up until parametric testing case 2, at which point damage within the shear key bond starts to initiate and the tensile capacity of the shear key to beam interface starts to reduce. The shear key strains modeled peak at about 17 με higher than the field measured strain. There is the potential for the UHPC itself to crack at this strain level, however this is considered

unlikely to meaningfully impact the modeled transverse strain results as they relate to the interface bond capacity and resultant loss of load transfer.

This is further demonstrated by the results at the support of the span, where tensile strain across the shear key is higher within the finite element model. Damage to the bond begins immediately at the girder end with the transverse tensile strain reducing in shear key 2 and shear key 3 between the Feb 14, 2021 and Parametric testing case 1. Shear key 1 did not exhibit the same debonding at the support. As discussed in Section 4.1.3 the calibration section the results at the support are less reliable due to the top flange movement restraint in the transverse and longitudinal directions utilized during calibration. Stress at this location, and ultimate initiation of damage criteria may not initiate as a result of the potential distortions.

Table 26: Mid Span Shear Key Strains Parametric Cases

Date	Result	EE11 Transverse Strains (uε)			EE33 Longitudinal Strains (uε)		
		SK 1	SK 2	SK 3	SK 1	SK 2	SK 3
Feb 14, 2021	Field	75	-	70	103	84	-
	FE Model	79	80	80	299	302	300
Parametric Case 1	FE Model	86	86	85	355	358	356
Parametric Case 2	FE Model	92	92	91	411	414	412
Parametric Case 3	FE Model	79	80	79	466	470	468
Note: FE model shear key measurements taken 58.75 mm below the top of shear key to correspond with approximate final placement of gauge within the shear key.							

Table 27: Support Shear Key Strains Parametric Cases

Date	Result	EE11 Transverse Strains (uε)			EE33 Longitudinal Strains (uε)		
		SK 1	SK 2	SK 3	SK 1	SK 2	SK 3
Feb 14, 2021	Field	70	69	75	-	-	-
	FE Model	115	92	70	240	249	245
Parametric Case 1	FE Model	129	88	62	284	298	290
Parametric Case 2	FE Model	136	80	53	332	347	345
Parametric Case 3	FE Model	137	72	44	377	396	392
Note: FE model shear key measurements taken 58.75 mm below the top of shear key to correspond with approximate final placement of gauge within the shear key.							

Similarly, Table *28* shows the mid span girder strains. Since the model is a fully elastic uncracked finite element model, the girder top and bottom longitudinal EE33 strains continue to increase with each of the parametric cases, not reflecting the likely cracking that occurred in the girder between the Jan 16, 2020 and Feb 14, 2021 temperature gradients discussed in Section 4.1.3. The transverse strain in the girder top flange, EE11, continues to increase up to parametric testing case 2, at which point a maximum is reached and the transverse flange strains are maintained.

From these results we can see that the difference in tensile strain across the shear key to girder bond is building up to parametric testing case 2. This indicates that the tensile stress, and likelihood of debonding is increasing. The longitudinal strains are not meaningfully different between the shear key and girders, indicating that longitudinal shearing stresses are not building in a meaningful way to lead to debonding.

Table 28: Mid Span Girder Strains Parametric Cases

Date	Result	EE11 Transverse Top Flange Strains (uε)				EE33 Longitudinal Top Flange Strains (uε)				EE33 Longitudinal Bottom Flange Strains (uε)			
		G1	G2	G3	G4	G1	G2	G3	G4	G1	G2	G3	G4
Feb 14, 2021	Field	291	326	289	267	151	120	131	99	61	64	61	40
	FE Model	261	254	254	252	289	284	282	285	240	240	239	240
Parametric Case 1	FE Model	291	282	282	280	343	338	336	338	290	290	289	289
Parametric Case 2	FE Model	311	298	299	295	396	390	388	391	339	339	339	339
Parametric Case 3	FE Model	315	291	293	290	448	443	440	443	389	388	388	389
NOTE: EE33 Longitudinal Top and Bottom Flange Strains reported are higher then measured field results. See further discussion on the variation in Section 4.1.3. where it is hypothesised that the girder cracked between Jan 16, 2020 and Feb 14, 2021 causing a cracked girder stiffness not realized by the Finite element model.													

To interpret these results it is useful to examine the Damage Index to understand the behaviour of the connection. The damage index is a measurement of whether the damage initiation criteria has been met and is the calculated output from the quadratic interaction function, described in Equation 10. If a value of unity has been met at an evaluated point, then the damage evolution criteria of the traction separation model initiates and the SK to Beam connection starts to de-bond within the model and residual bond capacity defined within the traction separation model starts to govern.

Figure *64* through Figure *67* contain the quadratic damage initiation function contour map for each of the parametric testing cases and Feb 14, 2021 case within the girder 1 shear key connection. From Figure *64* there is no damage occurring within the connection under the Feb 14, 2021 temperature gradient at mid span. Some potential damage has begun at the support, but debonding has not yet begun, as shown by the damage index.

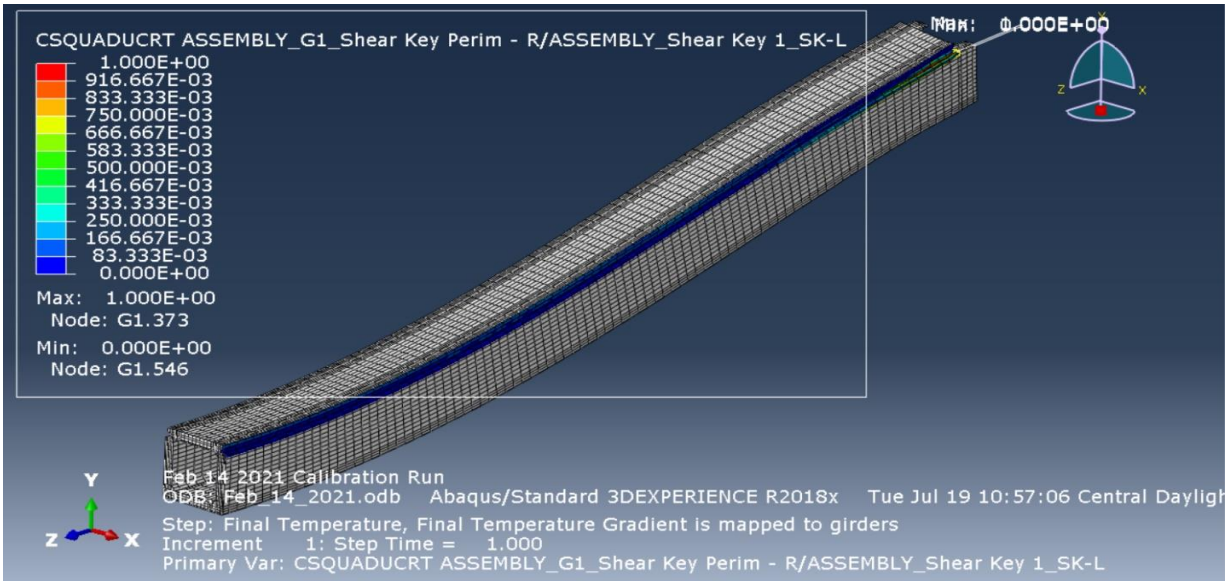

(a)

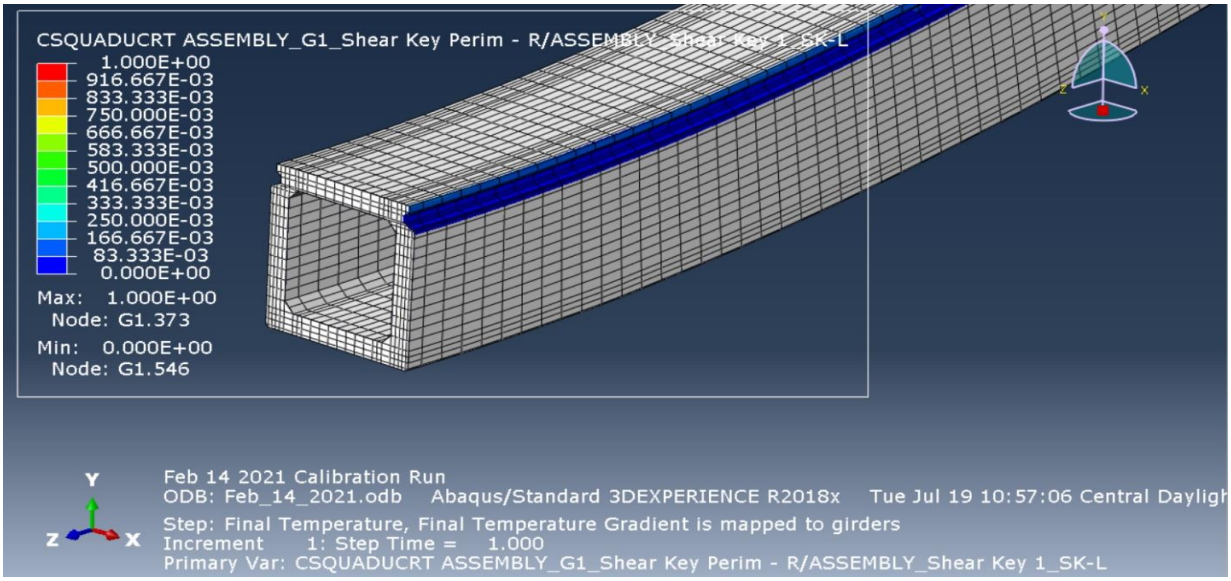

(b)

Figure 64: Feb 14, 2021 Temperature Gradient – Girder 1 Damage Index (a) Half Beam, (b) Mid Span

Under parametric testing case number 1, shown in Figure *65*, some damage within the shear key has begun within the top portions of the shear key at both mid span and at the support. A damage index ratio of unity has not yet been met, so debonding has not yet begun. As the temperature further decreases in parametric testing case 2, shown in

Figure *66*, a damage index ratio of unity is reached along the shear key in its upper half, indicating that debonding could be occurring within the top of the beam to shear key connection. The lower half of the shear key to beam bond is still intact with the separation criteria not yet being reached. Finally, under parametric case number 3, shown in Figure *67*, the damage initiation criterion has been met over most of the shear key height, with debonding likely occurring over much of the shear key to girder interface.

Examining the results, the evolution of shear key damage initiation and ultimate debonding is more pronounced at mid span compared to at the support. There is a clear progression of more severe increments of damage under decreasing temperature when compared to at the support, where the damage index remains constant. From the strain data we can see that the predominant mechanism of debonding of the shear key is direct tension forming across the interface, leading to the exceedance of the tensile capacity of the bond.

It was previously noted that the dowel strains directly at the support are slightly higher as well. It is possible that the boundary conditions utilized to calibrate this finite element model are creating a stress concentration at the ends of the beam not experienced by the in-service structure. Model calibration involved pinning the girder longitudinal movements at 1mm of movement. These pins were attached to the top flange of the girder ends as shown in Figure *49* and could be influencing stress distribution.

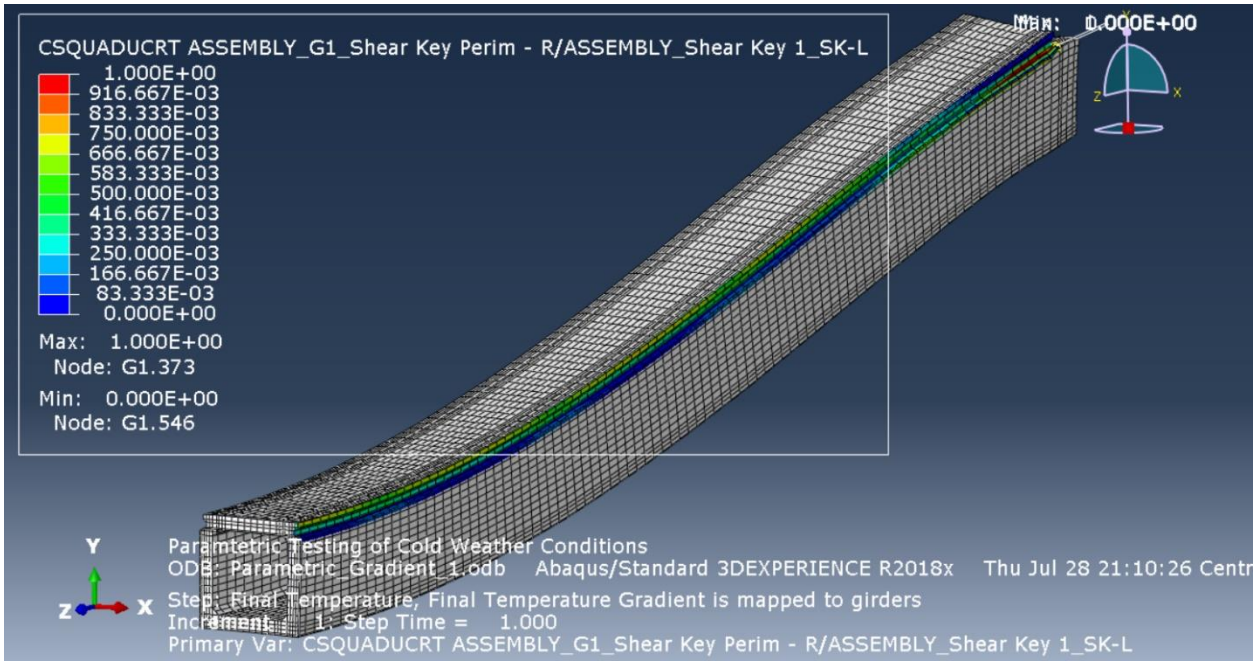

(a)

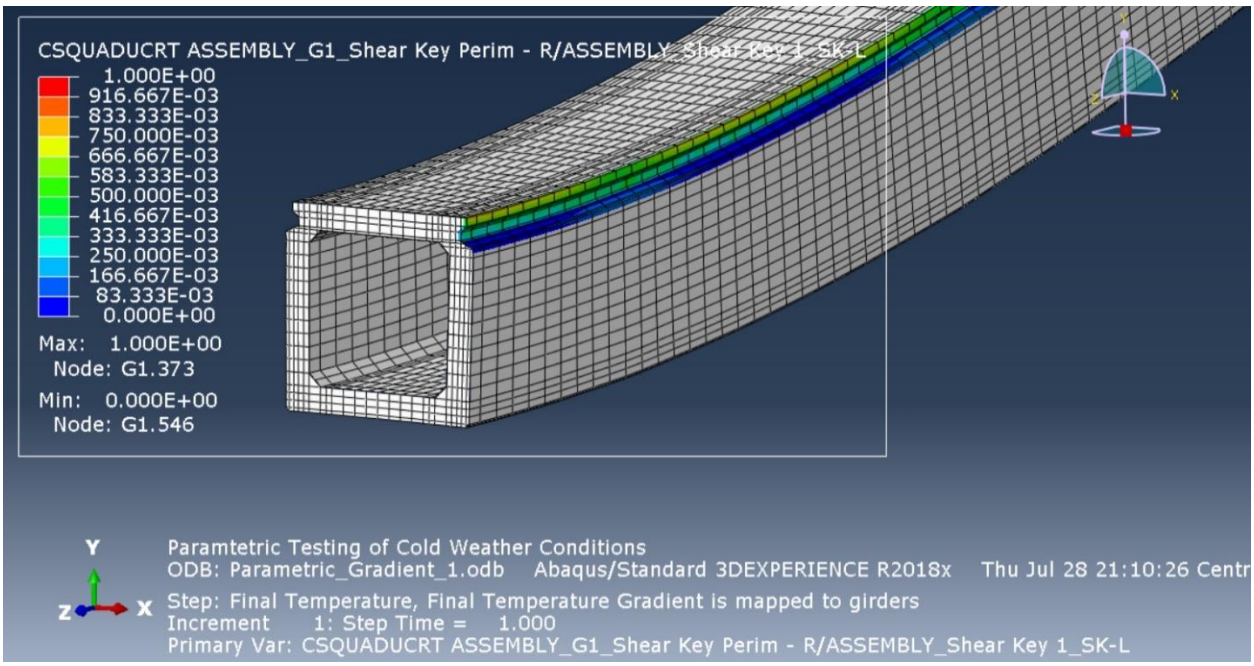

(b)

Figure 65: Parametric Gradient 1 – Girder 1 Damage Index (a) Half Beam, (b) Mid Span

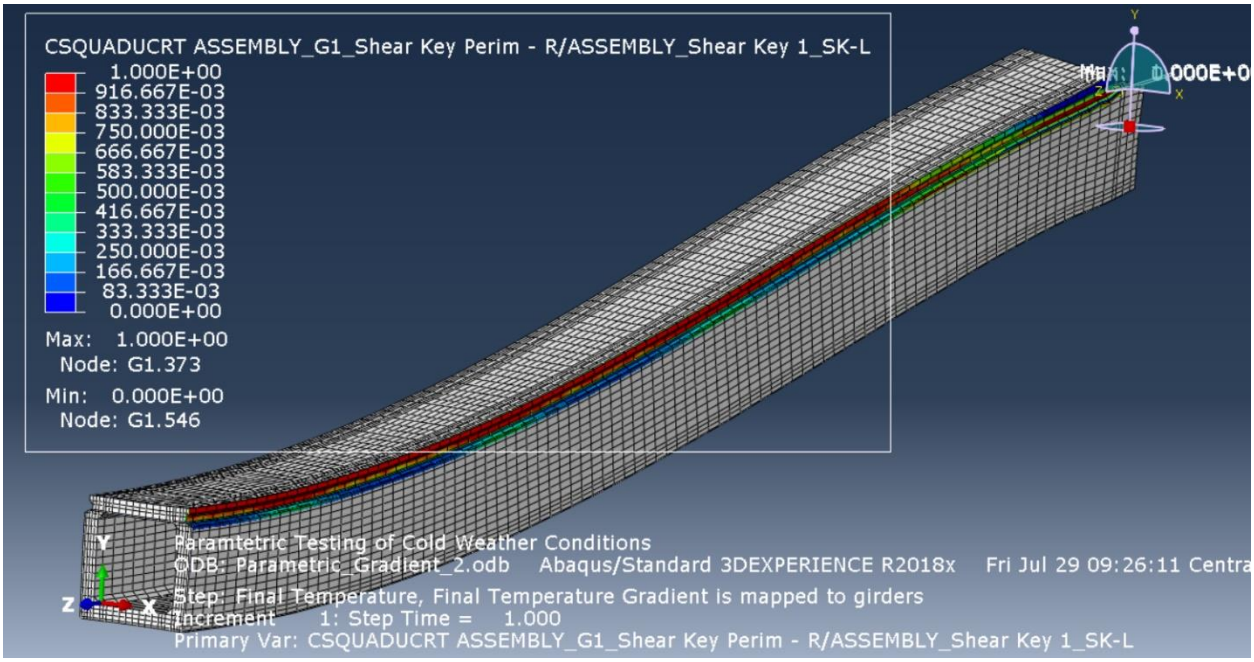

(a)

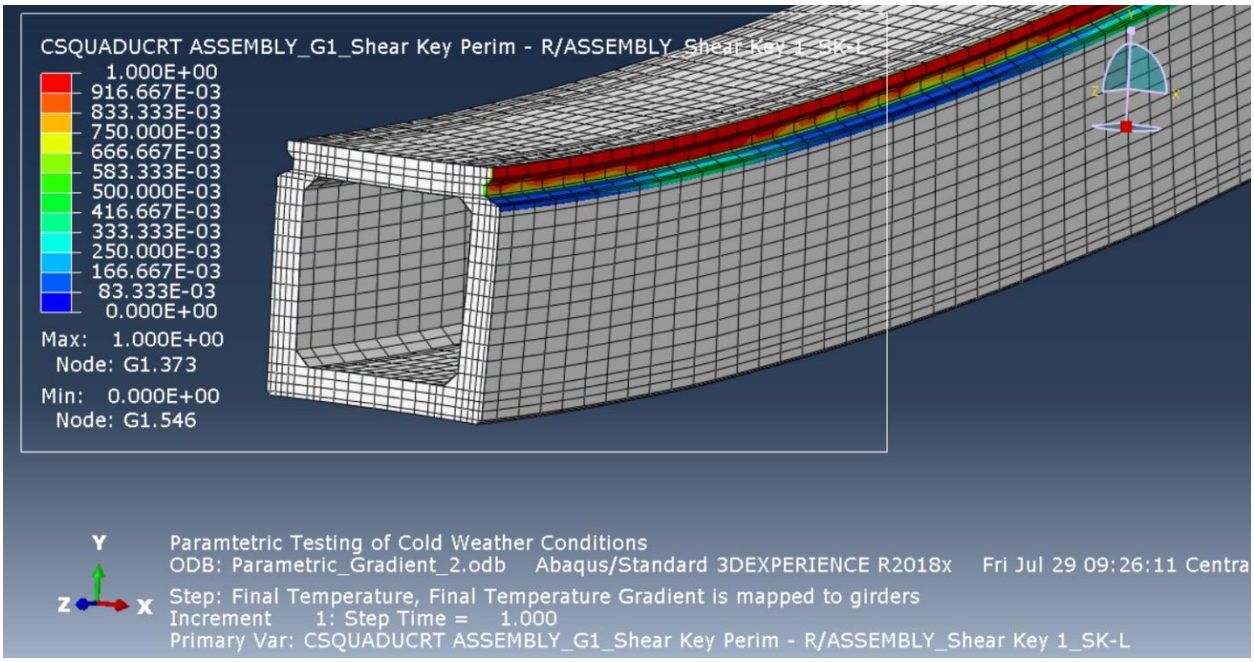

(b)

Figure 66: Parametric Gradient 2 – Girder 1 Damage Index (a) Half Beam, (b) Mid Span

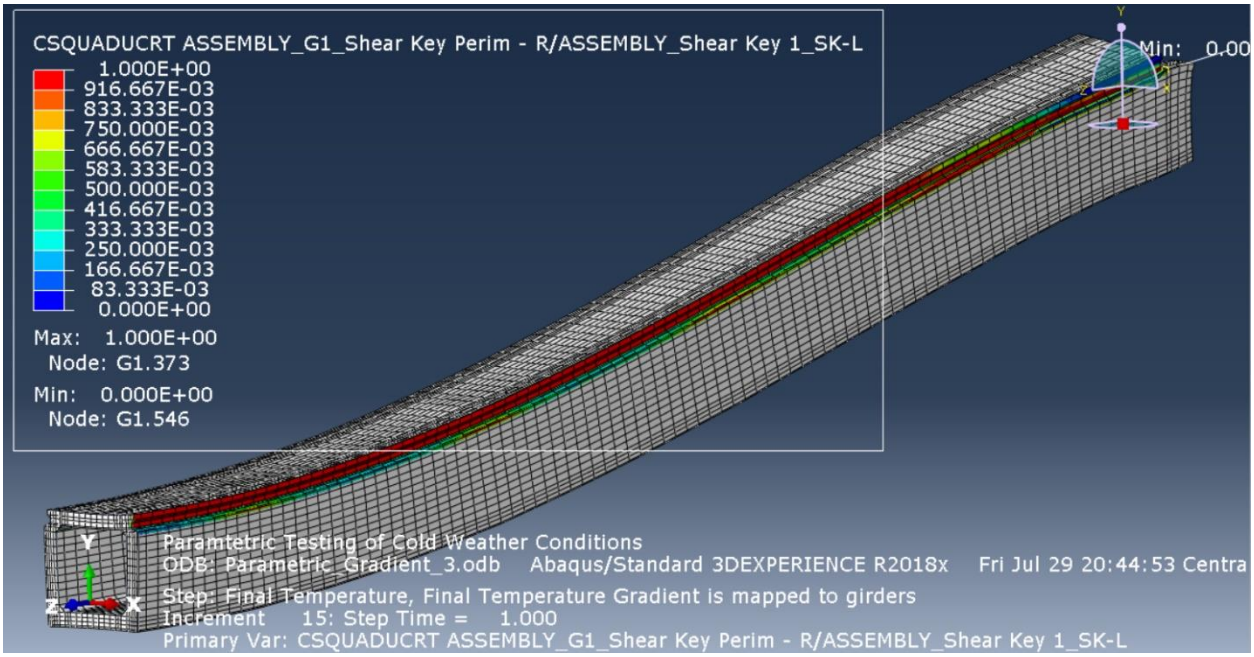

(a)

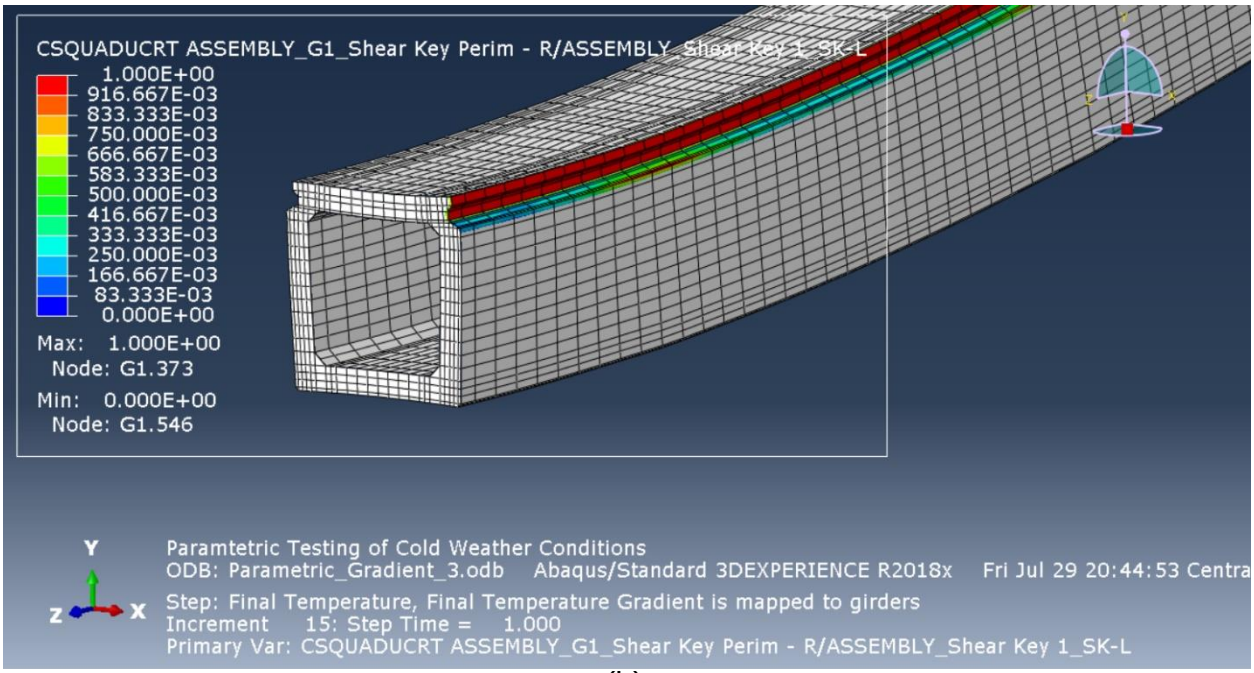

(b)

Figure 67: Parametric Gradient 3 – Girder 1 Damage Index (a) Half Beam, (b) Mid Span

As the damage to the shear key to beam bond progresses over each of the parametric testing cases, it is demonstrated by the finite element model that the dowels begin to transfer increasing tensile strain and resultant stress within the connection between the girders. Figure *68* through Figure *70* show the mid span dowel strains and strain at the shear key to dowel interface for each of the parametric testing cases. As the temperature gradient increases the strain within the dowel progressively increases as the connection begins debonding. Prior to debonding initiating the dowel strain at the interface is 670 με in parametric testing case 1. In parametric testing case 2, where just the top of the shear key has de-bonded, dowel strain increases to 917 με. Finally in parametric testing case 3, where the shear key has de-bonded over the full height of the dowels, the tensile strain within the dowel increases to 1227 με.

These dowel strains at the connection demonstrate that the dowels play a key role in continuing to transfer stress across the connection as the shear key de-bonds. Additionally, even under the most extreme parametric testing case, the dowel strain is still below its yield strain. When the dowel strains at the centreline of the shear key are examined, a substantial decrease in the tension is seen. With transference occurring between the dowel and UHPC shear key.

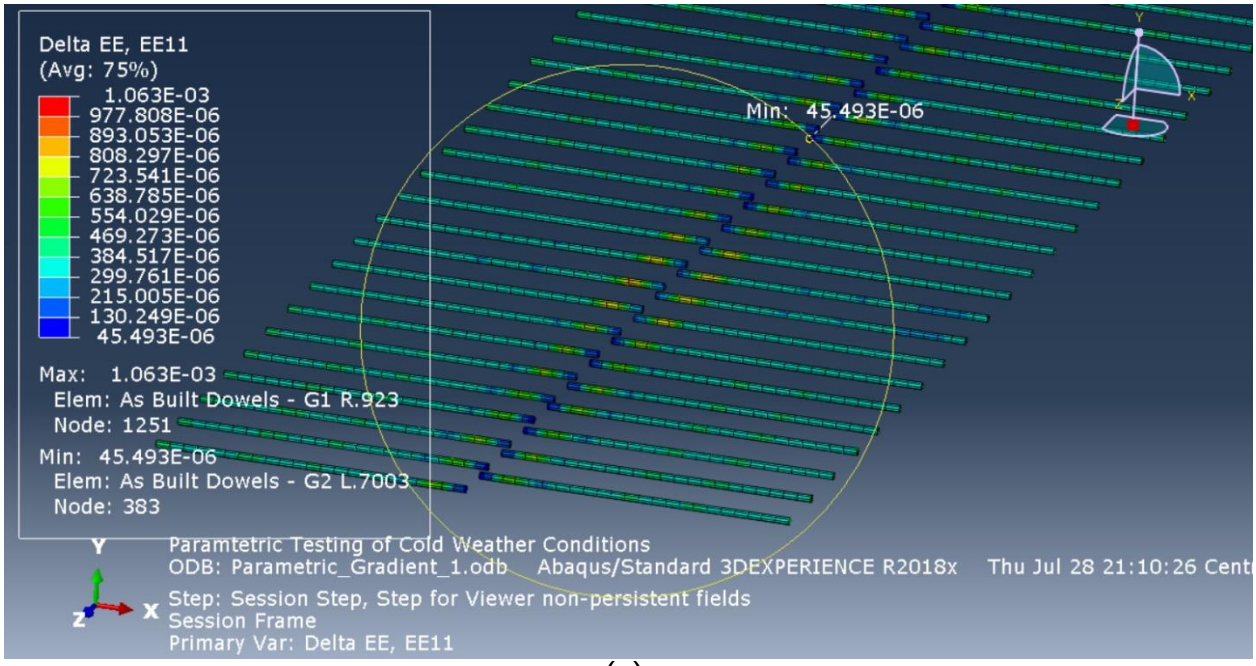

(a)

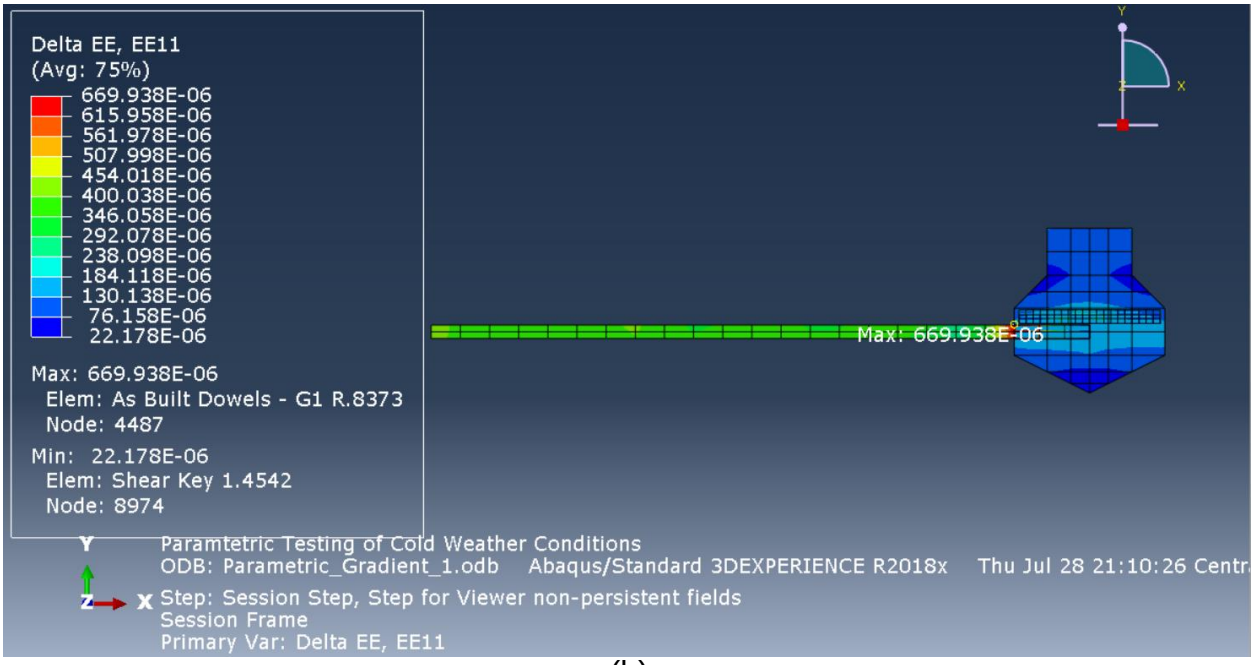

(b)

Figure 68: Parametric Gradient 1 – SK 1 Dowel Strain (a) Mid Span, (b) SK to Dowel Interface

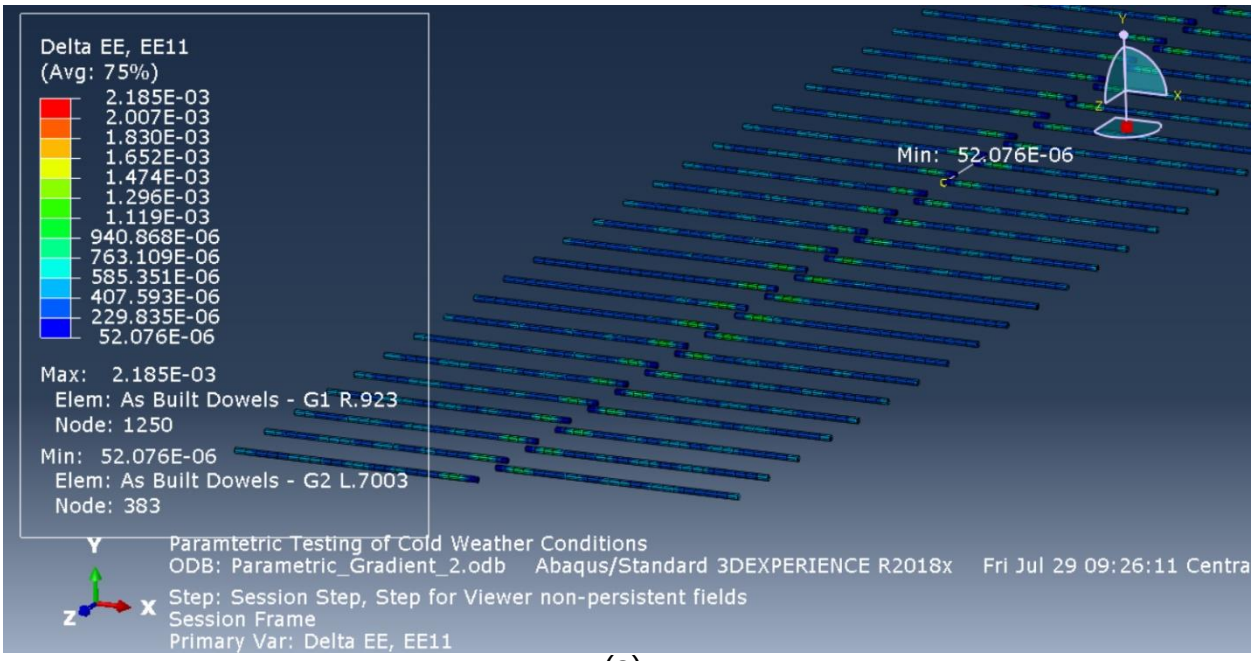

(a)

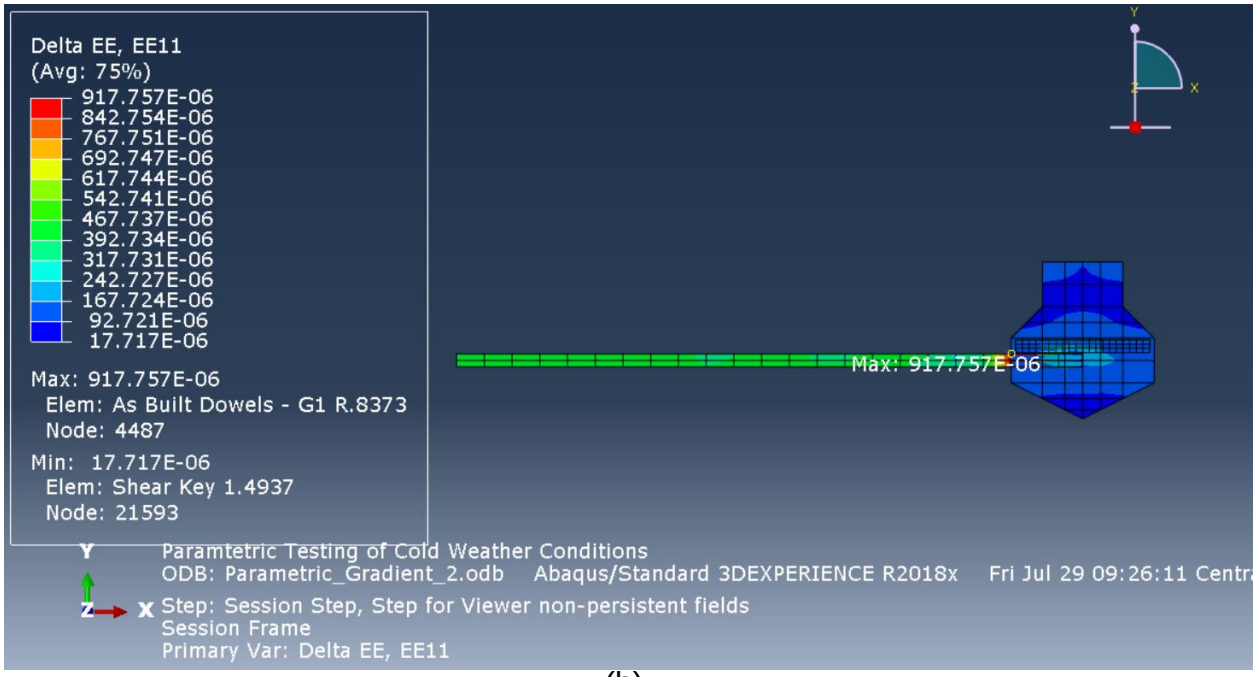

(b)

Figure 69: Parametric Gradient 2 – SK 1 Dowel Strain (a) Mid Span, (b) SK to Dowel Interface

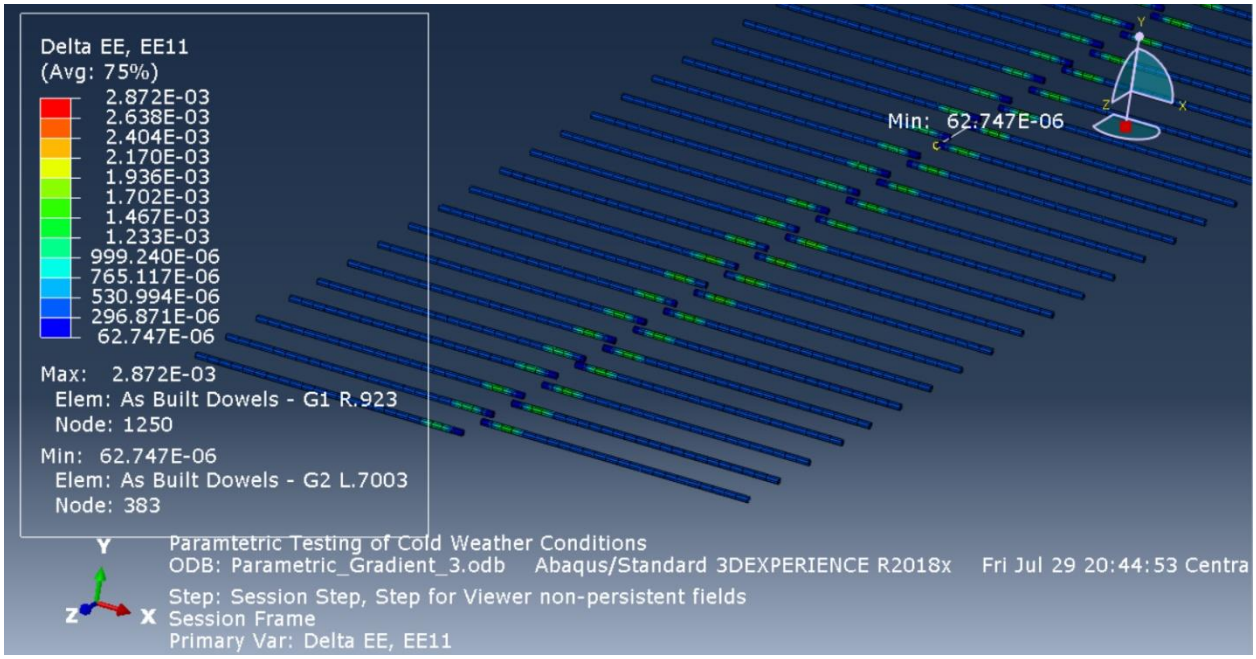

(a)

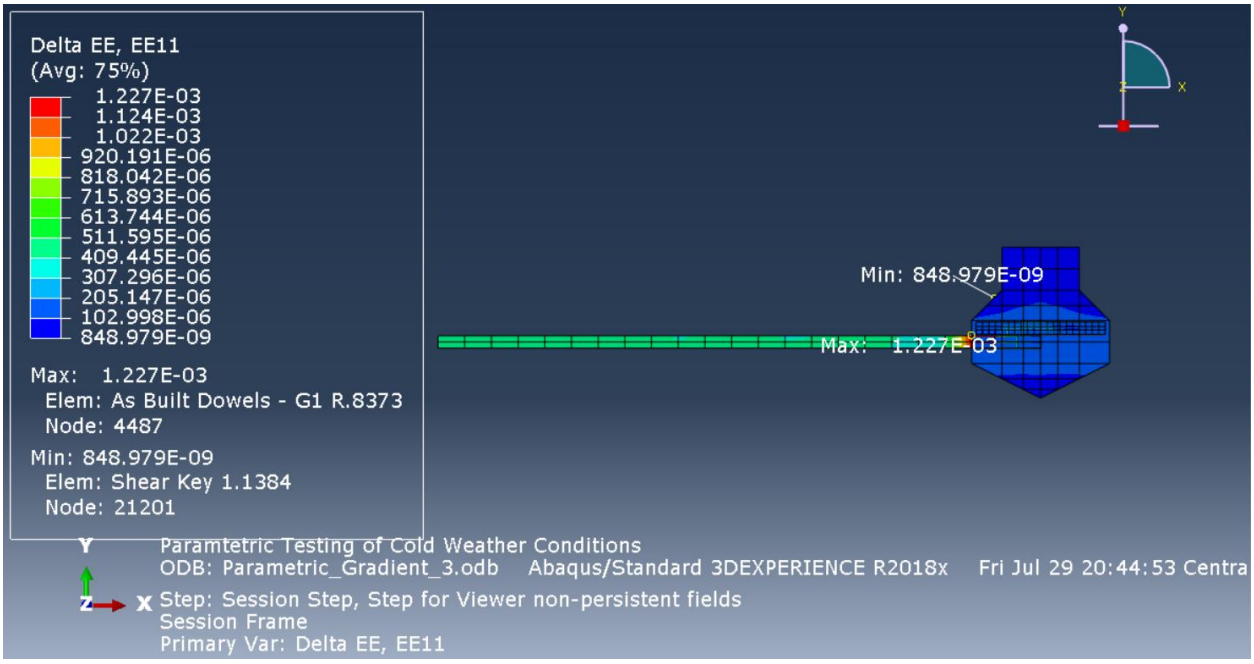

(b)

Figure 70: Parametric Gradient 3 – SK 1 Dowel Strain (a) Mid Span, (b) SK to Dowel Interface

5.0 Conclusions and Recommendations

The research program has been undertaken to investigate the cold weather behaviour of a UHPC shear key connection between adjacent precast prestressed box girders reinforced with dowels. The following chapter presents the conclusions of the research program and recommends some future areas of research.

5.1 Conclusions

Numerous conclusions related to shear key behaviour under thermal gradient loading can be made following completion of this research program. These conclusions may be split into categories and include:

5.1.1 Bridge Behaviour Under Gradient Thermal Loading

- Field measurements of girder strain of the Little Morris River Bridge revealed as ambient temperature decreases below zero degrees celsius tensile strain forms in the longitudinal and transverse bridge span direction in both the top and bottom flanges of the girder and across the shear key. Inversely, as the temperature increases above zero compressive strain forms in the transverse and longitudinal bridge span direction in both the top flange, bottom flange, and shear key.
- The dowels respond to temperature gradient by forming tension in their local axial direction under cold weather and compression along their local axial direction under warm weather. The magnitude of strain in the dowel is far lower than that of the shear key and girder top flange concrete.

5.1.2 Finite Element Modeling

- This study further validated that shear key bond behaviour may be modeled using a traction separation model within the finite element analysis allowing for the representation of a debonding failure mode between two materials in this case the UHPC and high strength girder concrete.
- The model was successfully defined using the results of direct tension test to define the normal stress response of the shear key, slant shear test to represent vertical shear force transfer response between girder units, and the Bi-shear test to represent the combined effect of tension and shear in the longitudinal direction of the shear key to box girder interface.
- Finite element model calibration revealed that different boundary conditions are required to facilitate modeling of the structure under cold and warm weather conditions. Cold weather conditions required greater fixity at the ends of the structure, while warm weather was best modeled utilizing a simply supported arrangement.
- Model calibration further revealed some general trends may exist with regards to material properties. First, as the Shear key modulus of elasticity increases, the tensile strain within the shear key decreases. Second, as the difference in modulus of elasticity between the shear key and girder increases, the magnitude of tensile strain within the shear key also trends downward.

- Ultimately model calibration was able to recreate the primary mechanism of failure in extreme cold, tensile stress across the shear key, with a high degree of conformance to the field measured data.

5.1.3 Shear Key Performance Under Severe Cold Temperature

- Under the coldest on record thermal gradient case, Feb 14, 2021, finite element modeling indicated that damage to the shear key to girder interface had not yet initiated. At the support, some damage initiation had begun within the modeling, however, the initiation criterion for debonding had not yet been reached.
- Under testing utilizing incrementally colder temperature gradients which decrease the coldest on record temperature distribution from February 14th, 2021 by a progressive 5 degrees celsius, it was found that damage within the shear key to girder bond at mid span initiates between 5 and 10 degrees colder than the Feb 14th, 2021 gradient.
- Damage and subsequent debonding initiates at the top of the shear key and progressively de-bonds further down the shear key under colder increments of temperature.
- The finite element modeling indicates that the evolution of shear key damage initiation and ultimate debonding is more pronounced at mid span compared to at the support. There is a clear progression of more severe increments of damage under decreasing temperature when compared to at the support, where the damage index remains relatively constant.

- As the damage to the shear key to beam bond progresses it is demonstrated by the finite element model that the dowels begin to transfer increasing tensile strain and resultant stress within the connection between the girders.
- The finite element model indicates that the dowels within the structure would stay under their yield strain reaching a tensile strain of 1227 με following debonding of the shear key within the finite element model.
- The study further found that the primary mechanism of shear key damage under increased colder weather is direct tension that forms across the shear key, demonstrating the importance of direct tension capacity of the key to perform under extreme cold.

5.2 Recommendations for Future work

Based on the results of the conducted finite element modelling some areas of future consideration have been formulated and include:

- The effects of short- and long-term shrinkage of UHPC as a shear key material should be considered.
- The nonlinear effect of concrete cracking under increased increments of loading should be investigated to examine the effect on shear key and dowel strains within the finite element modelling.
- No indication is provided from this study of the long-term effect of repeated cold weather cycles on the fatigue performance of the shear key to girder bond.

References

AASHTO Committee on Bridges and Structures. 2020. *LRFD Bridge Design Specifications 9th Edition.* Washington: American Association of State Highway and Transportation Officials.

ACI Committee 201. 2016. *ACI 201R-16: Guide to Durable Concrete.* American Concrete Institute (ACI.

Collins, Michael P., and Denis Mitchell. 1997. *Prestressed Concrete Structures.* Response Publications.

CPCI. 2017. *CPCI Design Manual 5th Edition.* Ottawa, ON: Canadian Precast/Prestressed Concrete Institute (CPCI).

CSA. 2019. *CAN/S6-19: Canadian Highway Bridge Design Code.* Toronto, ON: Canadian Standard Association (CSA).

Flietstra, Jason. 2011. *Creep and Shrinkage behaviour of ultra high-performance concrete under compressive loading with varying curing regimes.* Michigan Tech.

Graybeal, Benjamin, and Henry Russell. 2013. *Ultra-High Performance Concrete: A State-of-the-Art Report for the Bridge Community.* US Department of Transportation Federal Highway Administration.

Gulyas, Robert J, Gregory J Wirthlin, and Jeffery T Champa. 1995. "Evaluation of Keyway Grout Test Methods for Precast Concrete Bridges." *PCI Journal* 44-57.

Halbe, Kedar, Patrick Joyce, Carin L Roberts-Wollmann, and Thomas E Cousins. 2017. *Development of Improved Connection Details for Adjacent Prestressed Member Bridges.* Charlottesville: Virginia Department of Transportation.

Hussein, Husam, Kenneth Walsh, Shad Sargand, Fouad Al Rikabi, and Eric Steinberg. 2017. " Modeling the Shear Connection in Adjacent Box-Beam Bridges with Ultrahigh-Performance Concrete Joints. I: Model Calibration and Validation." *J. Bridge Eng.*

Hussein, Husam, Shad Sargand, and Issam Khoury. 2019. "Field investigation of ultra-high performance concrete shear key in an adjacent box-girder bridge."

Lopez de Murphy, Maria, Jubum Kim, Zi Sang Chao, and Thomas Larson D. 2010. *Determining More Effective Approaches for Grouting Shear Keys of Adjacent Box Beams.* Penn State: Commonwealth of Pennsylvania Department of Transportation; PennState University.

Mazzoti, Claudio, and Marco Savoia. 2012. "An Experimental Campaign on the Long-Term Properties of Self Compacting Concrete." *Advances in Structural Engineering.*

Newtson, Craig M, Brad D Weldon, Elsy Flores, Jordan Varbel, and William K Toledo. 2019. *UHPC Shear Keys in Concrete Bridge Superstructures.* Las Cruces: Transportation Consortuim of South Central States.

Ozyildrim, Celik H, and Gail M Moruza. 2016. "High-Performance Grouting Materials in Shear Keys Between Box Beams." *Transportation Research Record 2577* 35-42.

Persson, Bertil. 1999. "Poisson's ratio of high-performance concrete." *Cement and Concrete Research* 1647-1653.

Sargand, Walsh, Kenneth Shad, Husam Hussein, and Fouad Al Rikabi. 2017. "Modeling the Shear Connection in Adjacent Box-Beam Bridges with Ultrahigh-Performance Concrete Joints. II: Load Transfer Mechanism." *J. Bridge Eng.*

Semendary, A, L.X. Tan, and D Svecova. 2019. *Implementation of Precast Prestressed Concrete Box Beam Bridge Girders with UHPC Shear Keys in Manitoba.* Department of Civil Engineering; University of Manitoba.

Semendary, Ali, Eric Steinberg, Kennith Walsh, and Elne Barnard. 2019. "Effects of Temperature Distributions on Thermally Induced Behavior of UHPC Shear Key Connections of an Adjacent Precast Prestressed Concrete Box Beam Bridge." *J. Bridge Eng.*

Semendary, Ali, Kennith Walsh, and Eric Steinberg. 2017. "Early-Age Behavior of an Adjacent Prestressed Concrete Box-Beam Bridge Containing UHPC Shear Keys with Transverse Dowels." *J. Bridge Eng.*

Semendary, Ali, Li Tan Xin, and Dagmar Svecova. 2021. "Box Beam Bridge with UHPC Shear Keys in Manitoba (Long Term and Durability Tests)." Presentation to Province of Manitoba, Winnipeg.

Steinberg, Eric P, Ali Semendary, and Kennith Walsh. 2016. "Implementing Ultra High Performance Concrete (UHPC) with Dowel Bars in Longitudinal Joints (Shear

Key) in an Adjacent Box Beam Bridge." *First International Interactive Symposium on UHPC.*

Steinberg, Eric, John Ubbing, Oliver Giraldo-Londono, and Ali Semendary. 2014. "Parametric Analysis of Adjacent Prestressed Concrete Box Beams With UHPC-Dowel Shear Keys."

Structures, Subcommitte on Concrete. 2019. *Canadian Highway Bridge Design Code S6:19.* Toronto: Canadian Standards Association.

Sudziak, Slawomir, Wioletta Jackiewicz-Rek, and Zofia Kozyra. 2021. "On the Calibration of a Numerical Model for Concrete-to-Concrete Interface." *Materials.*

Tan, Li Xin. 2021. *Early Ange and Durability Study of the Bond Strength on the Interface between UHPC-HSC.* Winnipeg: University of Manitoba.

Tan, Li Xin, Ali A. Semendary, and Dagmar Svecova. 2021. "Estimation of bond strengths and design parameters for precast concrete-UHPC shear key interface in box beam bridge." *Engineering Structures.*

Weldon, Brad, Elsy Flores, Jordan Varbel, and William Toledo. 2019. *UHPC Shear Keys in Concrete Bridge Superstructures.* Transportation Consortium of South Central States.

WSP . 2018. "Plans of Proposed Bridge over Little Morris River on P.R. No. 422." *Province of Manitoba Construction Tenders Site No. 33987-10.* Winnipeg: Province of Manitoba, Decemeber 7.

Yuan, Jiqiu, and Benjamin Graybeal. 2016. "Full-Scale Testing of Shear Key Details for Precast Concrete Box-Beam Bridges." *J. Bridge Eng.*